

UC Irvine

UC Irvine Electronic Theses and Dissertations

Title

The Solution Synthesis of Group IV-Based Nanomaterials

Permalink

<https://escholarship.org/uc/item/459547tt>

Author

Cornell, Trevor Patrick

Publication Date

2015

Peer reviewed|Thesis/dissertation

UNIVERSITY OF CALIFORNIA,
IRVINE

The Solution Synthesis of Group IV-Based Nanomaterials

DISSERTATION

submitted in partial satisfaction of the requirements
for the degree of

DOCTOR OF PHILOSOPHY

in Chemistry

by

Trevor Patrick Cornell

Dissertation Committee:
Professor Allon I. Hochbaum, Chair
Professor Matthew Law
Professor Reginald Penner

2015

Chapter 4 © 2012 American Chemical Society
Portions of Chapter 5 © 2010 American Chemical Society
All other sections © 2015 Trevor Patrick Cornell

DEDICATION

To my family and friends,

Thank you for your unending support
and for being the reason why taking the hard road is worth it.

“A riddle everyone knows the answer to is worthless.”
-Batman

TABLE OF CONTENTS

LIST OF FIGURES	vi
LIST OF SCHEMES	ix
LIST OF TABLES	x
ACKNOWLEDGMENTS	xi
CURRICULUM VITAE	xii
ABSTRACT OF THE DISSERTATION	xiv
CHAPTER 1: An Introduction to Nanomaterials and Their Applications for Thermoelectrics	1
Introduction	1
World Energy Consumption	3
The Principles of Thermoelectric Materials	4
Current Materials	9
Modern Strategies for Improving Thermoelectric Performance	11
Thesis Objectives	17
References	20
CHAPTER 2: The Synthesis of Silicon–Germanium Alloy Nanocrystals	23
Introduction	23
The Properties of Silicon and Germanium	24
Synthetic Approaches for Silicon Nanomaterials	26
Synthetic Approaches for Germanium Nanomaterials	31
Synthetic Approaches for Silicon–Germanium Alloy Nanomaterials	32
Functionalization of Silicon and Germanium Surfaces	33
Results and Discussion	37
Conclusions and Future Work	57
Experimental Procedures	58
References	60
CHAPTER 3: The Synthesis of Metal–Germanide and Metal–Silicide Nanomaterials	67
Introduction	67
Synthetic Approaches for Metal–Silicide Nanomaterials	68
Synthetic Approaches for Metal–Germanide Nanomaterials	69
Experimental Design for Metal–Germanide Nanomaterials	69
Experimental Design for Nickel–Silicide Nanowire Arrays	70
Results and Discussion	71
Conclusions and Future Work	89
Experimental Procedures	90
References	93

CHAPTER 4: The Synthesis of Alkenylgold(I) Complexes via Sequential Hydrozirconation and Zirconium to Gold Transmetalation	100
Introduction	100
Results and Discussion	101
References	107
Experimental Procedures	109
CHAPTER 5: Development of a New Experimental Method for Real-Time Imaging of Platinum–Sulfur Covalent Bond Formation	140
Introduction	140
Experimental Design	141
Results and Discussion	145
References	149
Experimental Procedure	151

LIST OF FIGURES

		Page
Figure 1.1	Outline of nanocrystal synthesis phases	2
Figure 1.2	Influence of size on nanocrystal luminescence.....	3
Figure 1.3	Schematic of a thermoelectric device	5
Figure 1.4	The relationship of variables that determine the Figure of Merit.....	8
Figure 1.5	Crystal structure of Half-Heusler materials	11
Figure 1.6	Example of energy filtering barriers in Pb/PbTe.....	13
Figure 1.7	Crystal structure of skutterudites and clathrates.....	15
Figure 1.8	Outline of the fabrication of solution-processed Group IV-based devices	19
Figure 2.1	Diamond cubic crystal structure	25
Figure 2.2	Outline of a non-thermal plasma synthesis setup	28
Figure 2.3	Outline of a laser pyrolysis synthesis setup.....	28
Figure 2.4	TEM and XRD of SiGe particles synthesized in oleylamine with <i>n</i> -butyllithium as a reducing agent.....	38
Figure 2.5	TEM of SiGe particles synthesized in squalane with <i>n</i> -butyllithium as a reducing agent.....	40
Figure 2.6	Raman spectra of Si and Ge only reactions in squalane	40
Figure 2.7	IR spectrum of nanocrystals synthesized in squalane	41
Figure 2.8	Si nanocrystals produced from various concentrations of TOAB.....	44
Figure 2.9	Hexane solutions of SiGe alloy nanocrystal products	45
Figure 2.10	TEMs, size histograms, and SAED patterns of SiGe nanocrystals	46
Figure 2.11	Elemental analysis and Raman spectra of SiGe nanocrystals	48

Figure 2.12	TEMs of Si nanocrystals produced from different reductants.....	50
Figure 2.13	TEMs of Si nanocrystals produced from SiI ₄ and weak reductants	50
Figure 2.14	IR spectra of hexyl-capped SiGe nanocrystals.....	53
Figure 2.15	UV-Vis absorption and emission spectra of SiGe nanocrystals	56
Figure 3.1	TEM and size histogram of Ge nanocrystals produced from GeBr ₂	71
Figure 3.2	XRD of Ge nanocrystals produced from GeBr ₂	72
Figure 3.3	IR spectrum of Ge nanocrystals produced from GeBr ₂	72
Figure 3.4	Nickel(0) precursors used for the production of nickel germanide.....	73
Figure 3.5	TEM and size histogram of nickel germanide nanocrystals produced using Ni(COD) ₂	74
Figure 3.6	XRD of nickel germanide nanocrystals produced from Ni(COD) ₂	75
Figure 3.7	Nickel germanide phase diagram.....	76
Figure 3.8	IR spectrum of nickel germanide nanocrystals	77
Figure 3.9	TEM and size histogram of iron germanide nanocrystals	78
Figure 3.10	XRD of iron germanide nanocrystals	79
Figure 3.11	Iron germanide phase diagram.....	80
Figure 3.12	IR spectrum of iron germanide nanocrystals	81
Figure 3.13	TEM and size histogram of palladium germanide nanocrystals	82
Figure 3.14	XRD of palladium germanide nanocrystals at various processing temperatures.....	83
Figure 3.15	IR spectrum of palladium germanide nanocrystals	84
Figure 3.16	Overview of electroless etching synthesis of silicon nanowire arrays.....	85
Figure 3.17	SEM images of nickel silicide nanowire synthetic process	87

Figure 3.18	TEM image of nickel silicide nanowires	88
Figure 3.19	XRD of nickel silicide evolution from silicon nanowires.....	88
Figure 4.1	Precursors used for the synthesis of alkenylgold(I) complexes	101
Figure 5.1	Graphic representation of TIRF microscopy setup	142
Figure 5.2	BODIPY fluorophores and thiourea-functionalized silane studied.....	143
Figure 5.3	Revised injection setup and reaction cell.....	144
Figure 5.4	Outline of photopatterning process for sample creation.....	146
Figure 5.5	Representative data collected from single molecule imaging	147
Figure 5.6	Representative MATLAB time traces displaying quantized “on-off” single molecule activity.....	148

LIST OF SCHEMES

Scheme 2.1	Thermal decomposition of hydrogen silsesquioxane for the production of silicon nanocrystals	27
Scheme 2.2	Colloidal approaches to Si and Ge nanomaterials synthesis	30
Scheme 2.3	Germanium specific colloidal syntheses	31
Scheme 2.4	Surface modification approaches for silicon and germanium nanocrystals	34
Scheme 2.5	Surfactant-mediated room temperature synthesis of Group IV nanocrystals	43
Scheme 2.6	Proposed mechanisms for Pt-catalyzed and UV-mediated hydrosilylation/hydrogermylation	52
Scheme 4.1	Synthetic scheme for the production of alkenylgold(I) complexes	101
Scheme 4.2	Proposed isomerization of 2e via a gold carbenoid intermediate	104

LIST OF TABLES

Table 2.1	Indexing of selected area electron diffraction patterns for Si and Ge.....	45
Table 4.1	Reaction substrate scope for alkenylgold(I) complex synthesis	103

ACKNOWLEDGMENTS

I would like to thank my advisor, Professor Allon Hochbaum, for giving me the freedom to pursue my own ideas during my work in his lab. His encouragement to think outside the box helped me to grow as a scientist and learn to approach problems from different angles, which was invaluable throughout my time in his lab.

I would also like to thank Professor Suzanne Blum. During my time in her lab, she not only gave me a thorough grounding in good lab technique, but also gave me an appreciation for being thorough and always giving the smallest of details the attention they deserve. Ultimately, this has not only made me a better scientist, but a better thinker as a whole.

There are a number of people I have had the pleasure of working with and learning from throughout my time as a graduate student. Dr. Yili Shi and Dr. Katrina Roth were both excellent mentors and friends, who kept me from feeling completely overwhelmed as a new student. Doug Otte, Dr. Joshua Hirner, Dr. Shawn Miller, and John Naviaux have been some of the best friends I could have asked for, and I will be forever grateful for their camaraderie throughout my time at UCI.

Finally, I would like to thank Dr. Miranda Paley. You push me to be a better person, in all aspects of my life, and I know that I would not be who I am today without you. Your love and support mean more to me than I could ever hope to express in words.

Trevor P. Cornell
CURRICULUM VITAE

EDUCATION

University of California, Irvine, Irvine, CA 2009-2015
Ph.D. Inorganic Chemistry

The College of New Jersey, Ewing, NJ 2005-2009
B.S. Chemistry, Forensic Chemistry specialization, Criminal Justice minor

RESEARCH EXPERIENCE

University of California, Irvine, Irvine, CA
Advisor: Allon Hochbaum 2012–2015
Research: Synthesis of Silicon- and Germanium-based Nanomaterials for Thermoelectric Applications

Advisor: Suzanne Blum 2010–2012
Research: Synthesis of Alkenylgold(I) Complexes via Zirconium to Gold Transmetalation

PUBLICATIONS

5. Dupper, T.; Cornell, T. P.; Hochbaum, A. I. *In Preparation, December, 2015.*
4. Cornell, T. P.; Hochbaum, A.I. Solution Phase Synthesis of Silicon–Germanium Alloy Nanocrystals. *Submitted, September, 2015.*
3. Cornell, T. P.; Shi, Y.; Blum, S.A. Synthesis of Alkenylgold(I) Compounds via Sequential Hydrozirconation and Zirconium to Gold Transmetalation. *Organometallics* **2012** *31*, 5990–5993.
2. Esfandiari, N.M.; Wang, Y.; Bass, J.Y.; Cornell, T.P.; Otte, D.A.L.; Cheng, M.H.; Hemminger, J.C.; McIntire, T.M.; Mandelsham, V.A.; Blum, S.A. Single Molecule Imaging of Platinum Ligand Exchange Reaction Reveals Reactivity Distribution. *J. Am. Chem. Soc.* **2010** *132*, 15167–15169.
1. Donnelly, S.; Marrero, J.E.; Cornell, T.; Fowler, K.; Allison, J. Analysis of Pigmented Inkjet Printer Inks and Printed Documents by Laser Desorption/Mass Spectrometry. *J. Forensic Sci.* **2010** *55*, 129–135.

TEACHING EXPERIENCE

Graduate Teaching Assistant, Department of Chemistry, University of California, Irvine
Materials Chemistry (for graduate students), Winter 2014
General Chemistry Discussions, 2011–2012 academic year, Summer 2015, Fall 2015
General Chemistry Lab, Summer 2015
Honors General Chemistry Discussions, Fall 2010
Organic Chemistry Lab, 2009–2010 academic year, Winter 2011

PRESENTATIONS

American Chemical Society National Meeting- Denver, CO, 2015. Oral Presentation

OTHER RELEVANT EXPERIENCE

Laboratory Technician, Lexicon Pharmaceuticals, Princeton, NJ

2008

ABSTRACT OF THE DISSERTATION

The Solution-Phase Synthesis of Group IV-Based Nanomaterials: Silicon–Germanium Alloy, Metal Silicide, and Metal Germanide Nanocrystals

By

Trevor Patrick Cornell

Doctor of Philosophy in Chemistry

University of California, Irvine, 2015

Professor Allon I. Hochbaum, Chair

Nanomaterials derived from silicon and germanium have demonstrated several desirable properties for a variety of materials applications, such as optoelectronics, spintronics, catalysis, and thermoelectrics. Currently, the synthetic library for the production of technologically relevant Group IV nanomaterials comprised of silicon–germanium alloys, metal-silicides, and metal germanides are extremely limited, particularly with regard to solution-phase approaches. The work presented in this dissertation demonstrates the expansion of existing protocols to produce a variety of new Group IV-based nanomaterials using solution-phase syntheses. For the first time, silicon–germanium alloy nanocrystals are produced from a solution-phase approach. In addition, a new, generalizable scheme for the production of a variety of metal germanide nanocrystals is demonstrated through the use of metal(0) precursors. This methodology is then adapted to existing electroless etching methodologies used to produce silicon nanowire arrays, leading to the production of heterostructured silicon/metal silicide nanowires.

Chapter 1: An Introduction to Nanomaterials and Their Applications for Thermoelectrics

1.1 Introduction

History is littered with examples of nanomaterials being applied (however unwittingly) to a variety of applications as far back as the 4th century. Appearing in gorgeous pieces of artwork such as the Lycurgus Cup, the stained glass windows and ceramics produced throughout the Middle Ages, or in more practical applications, such as the Damascus steel blades which are still famous today for their beautiful patterning and incredible strength, the unique size-dependent properties of nanomaterials have spawned an incredibly diverse field of research which continues to expand without any signs of slowing.

From a scientific standpoint, the first principles concerning the production of nanomaterials were advanced by Victor La Mer and Robert Dinegar in 1950, with their experiments on the production of sulfur colloids from the decomposition of sodium thiosulfate.¹ From these experiments, they outlined the process in which colloidal nanoparticle growth occurs, which is outlined in Figure 1.1. They identified three distinct stages of the reaction. During Stage I there is a gradual buildup in concentration of the monomer. Eventually, a critical concentration is reached (Stage II), and nucleation of particles begins. This nucleation reduces the concentration of monomer, and the reaction moves to Stage III, where new nucleation events are eschewed in favor of growth of existing particles. In order to avoid particle aggregation and control the size and shape of the products, surface-stabilizing ligands are often employed.²

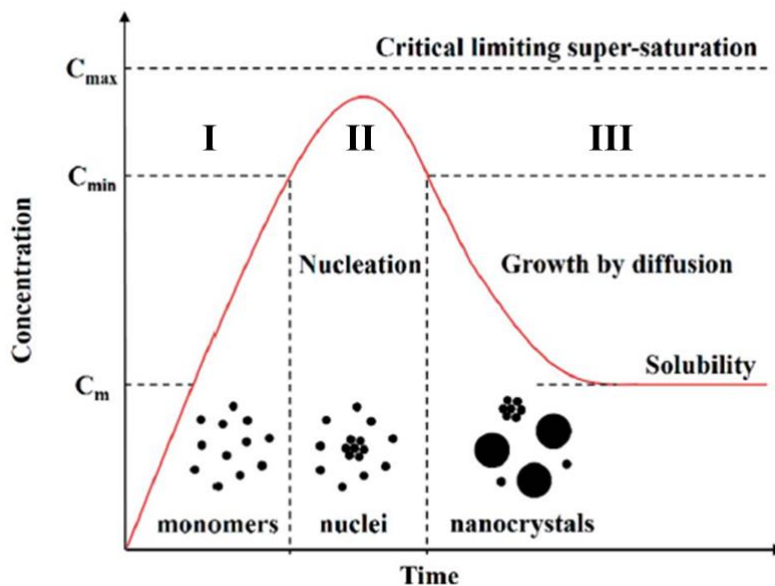


Figure 1.1 Outline of nanocrystal synthesis phases. First, a buildup of monomer occurs, until a critical concentration is reached. Monomers then begin to coalesce into nuclei. Eventually, further nucleation is disfavored, and growth of existing particles preferentially occurs.³

Since these early experiments, an innumerable array of different synthetic systems has been developed for the production of an equally diverse set of materials. These materials have found their way into a myriad of uses in modern life, ranging from the cutting edge of technical advancements to the unlikeliest of everyday consumer products.

One particular area in which nanotechnology holds a great deal of promise, and where a is in the development of semiconductor nanomaterials, which were first investigated and developed by Louis Brus and coworkers at Bell Labs during the 1980s.⁴⁻⁶ Since their work, semiconductor nanocrystals have seen widespread adoption into a number of areas such as photocatalysis,⁷ energy conversion, photoluminescence, sensors, and bioimaging, among others.

The greatest strength of semiconductor nanomaterials is the ability to control their optical and electronic properties through manipulation of their size, composition, and surface chemistry (Figure 1.2). As the size of the nanocrystals decreases, quantum confinement leads to an overall increase in the band gap between the valence and conduction bands in the material, relative to bulk values, allowing one to customize the material to suit the desired application. This is particularly relevant for applications related to energy conversion applications such as thermoelectrics, where matching the band gap to the desired operation temperature is critical to achieving the best performance possible.

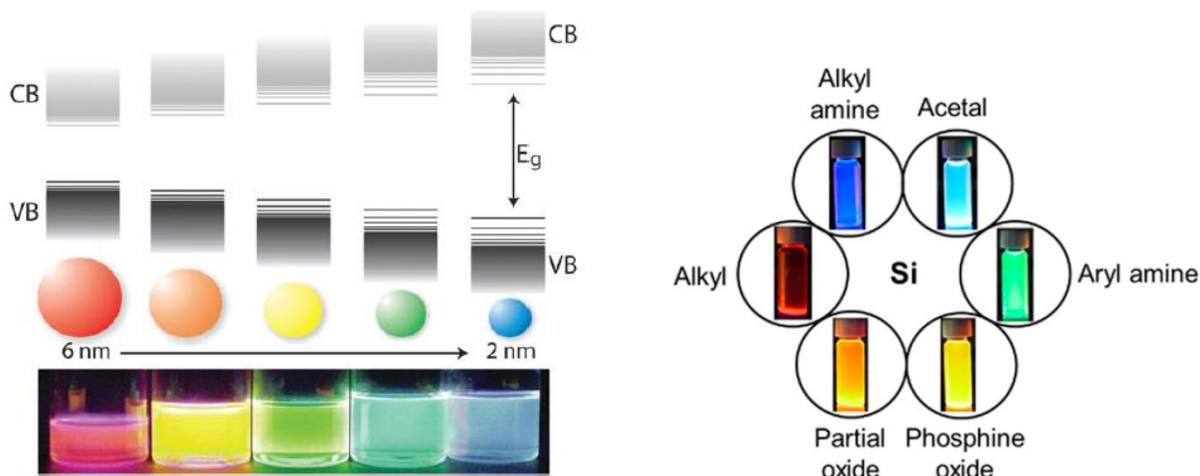


Figure 1.2 a) Influence of size on CdSe nanocrystal luminescence and band structure.⁸ b)

Influence of surface ligand on Si nanocrystal luminescence.⁹

1.2 World Energy Consumption

The creation and consumption of electrical energy has become inextricably linked with modern society's daily function. Finite resources, coupled with increasing demand have spurred the development of alternative methods for the production of electricity. Thermoelectric materials, which are capable of producing electricity when in the presence of a thermal gradient,

present an attractive approach towards utilizing heat energy which would otherwise be wasted.¹⁰ The ubiquity of anthropogenic heat sources makes thermoelectric power generation potentially more reliable compared to other alternative energy production methods that rely on environmental factors, such as sunlight, water, and wind. Currently, approximately 90% of the world's power is generated through the combustion of fossil fuels. Typically, the heat engines used in these processes only operate at 30–40% efficiency.¹¹ On a global scale, this translates into a loss of more than 15 terawatts (15,000 gigawatts) of energy annually. Furthermore, a number of other energy-intensive heat sources exist, principally in the industrial sector, where up to 50% of consumed energy is lost as waste heat.¹² Accessing even a small fraction of the energy lost from these types of sources has the potential to provide a contribution on par with, or greater than, other renewable sources.

1.3 The Principles of Thermoelectric Materials

The conversion of thermal energy directly into electricity was discovered by Thomas Seebeck in 1821. In thermoelectric materials, thermal excitation generates charge carriers at the hot side of the material. These charge carriers then diffuse towards the cold side. The resulting buildup of charge leads to the generation of an electrostatic potential that can then be exploited when the material is integrated into a circuit.

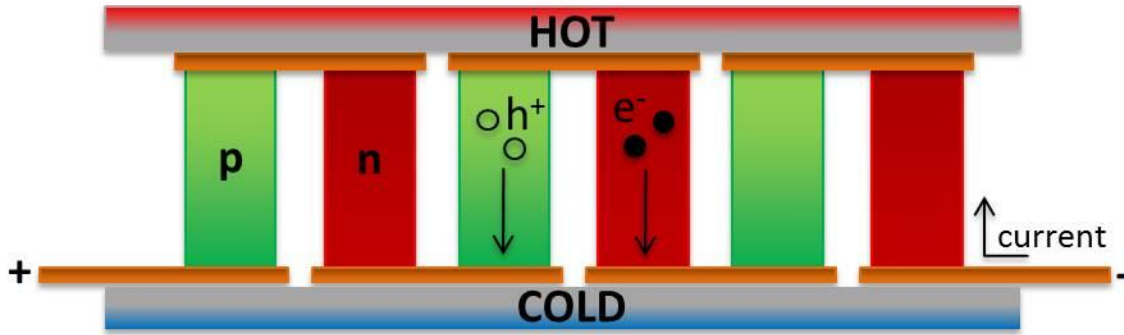


Figure 1.3 Schematic of a thermoelectric device. Alternating p- and n-type semiconductors are placed electrically in series and thermally in parallel. When a thermal gradient is applied to the system, thermal excitation generates charge carriers at the hot side. Diffusion and subsequent buildup of these charges at the cold side produces a voltage that can be exploited.

The performance of thermoelectric materials is benchmarked through its “figure of merit”, zT , which is defined by the equation below.^{10,13,14}

$$zT = \frac{\sigma S^2 T}{\kappa}$$

The figure of merit is dependent on electrical conductivity, σ , the Seebeck coefficient, S , absolute temperature, T , and thermal conductivity, κ . The term σS^2 is often referred to as the power factor, and is representative of the material’s ability to generate energy from a given thermal gradient, with a larger power factor representing more effective conversion of heat into electricity. The overall efficiency of a thermoelectric material is a function of this figure of merit and the Carnot efficiency according to the following equation:^{14,15}

$$\eta = \frac{T_h - T_c}{T_h} \frac{\sqrt{1 + zT} - 1}{\sqrt{1 + zT} + T_c/T_h}$$

where T_h and T_c are the temperature of the hot and cold side of the device, respectively.

Electrical conductivity is related to carrier concentration, n , and carrier mobility, μ , through the relationship:^{10,13,14}

$$\sigma = ne\mu$$

As with electrical conductivity, the Seebeck coefficient is also dependent on carrier concentration; however, its inverse relationship puts it directly at odds with what would benefit electrical conductivity. m^* in this equation represents the carrier's effective mass.^{10,13,14}

$$S = \frac{8\pi^2 k_b^2}{3eh^2} m^* T \left(\frac{\pi}{3n}\right)^{\frac{2}{3}}$$

Conceptually, the Seebeck coefficient can be thought of as the voltage generated per degree of temperature difference between the hot and cold sides of a thermoelectric device ($\Delta V/\Delta T$).

Minimizing thermal conductivity is another key factor in improving the performance of thermoelectric devices, owing to the necessity of maintaining as large a ΔT as possible between the hot and cold sides of the thermoelectric device.^{10,13,14}

$$\kappa = \kappa_e + \kappa_l$$

Two key sources of thermal conductivity need to be considered in thermoelectric materials. The first is the electronic component, κ_e . This is the heat that is transported along by the excited charge carriers (both electrons and holes) as they migrate through the material. This

is of particular importance in semiconductor systems, since they rely on doping to increase their number of generated charge carriers in order to achieve better electrical conductivity values. The electronic contribution to thermal conduction is temperature dependent, and is defined in the Wiedemann-Franz law as:^{10,13,14}

$$\kappa_e = L\sigma T$$

Where L is the Lorentz factor, which varies with carrier density and electron scattering in semiconductor systems. In contrast to phonon thermal conduction, the electronic contribution to thermal conduction generally increases along with temperature, as more charge carriers are generated.

The second source, κ_l , is referred to as the lattice thermal conductivity, which arises from phonon propagation through the material. Phonons can be described as coherent oscillations or vibrations of the atoms making up the material. In crystalline materials, as temperature increases, the thermal conductivity contribution from phonons actually decreases. This is related to the fact that while the number of phonons increases linearly with temperature, phonon specific heat remains relatively constant, as described by the Dulong-Petit law.¹⁶ Since phonon-phonon scattering is directly proportional to the number of phonons present, the greater number of phonons present results in an increased rate of phonon scattering and an overall lower thermal conductivity.

Although improving zT may seem straightforward at first glance, a closer examination at the individual factors contributing to the overall performance of a thermoelectric material reveals the conflicts that arise when trying to manipulate various properties to attain the highest zT possible. Figure 1.4 illustrates how the Seebeck coefficient, electrical conductivity, and thermal

conductivity change with increasing carrier concentration, along with the effect this has on the overall figure of merit. As carrier concentration increases, both electrical and thermal conductivities show an exponential increase, while the Seebeck coefficient steadily decreases. The optimal carrier concentration can be found in the region of 10^{19} to 10^{21} carriers per cm^3 .¹⁰

Attaining the highest possible values for zT involves decoupling the electrical and thermal conductivities of a material. Ideally, the material should behave as a crystalline material for the purposes of electrical conduction, but as a glass for phonon conduction.^{10,13,14,17} In a glass, thermal energy is not transferred through the lattice via phonon transport, but rather, the thermal energy is propagated through a “random walk” of energy, due to the lack of an extended ordered structure. Conversely, the best electronic transport properties are achieved in crystalline materials, due to the increased scattering and lower effective carrier masses present in amorphous materials. Strategies for addressing these issues to obtain improved zT values are discussed later in this chapter.

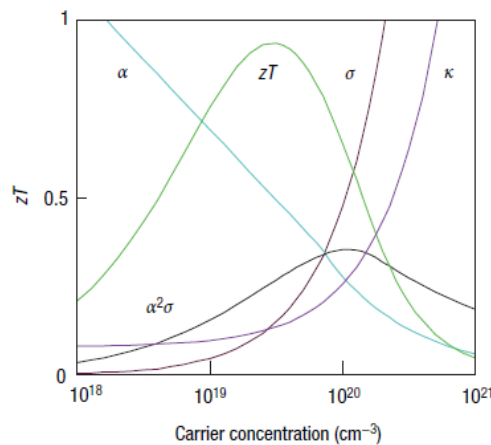


Figure 1.4 The complex relationship between the Seebeck coefficient, α , electrical conductivity, σ , and thermal conductivity, κ , and their effect on the figure of merit with respect to carrier concentration.¹⁰

1.4 Current Materials

The earliest high performance thermoelectric material discovered was bismuth telluride, Bi_2Te_3 , which was the first material to reach a zT of 1, back in the 1950s. It was also the material of choice used by Hicks and Dresselhaus for their investigations into the effects of quantum confinement on thermoelectric performance.^{18,19} Bismuth telluride crystallizes in the tetradymite crystal structure, and has a melting point of 586 °C. Its ideal operating temperature range is significantly lower than other thermoelectric materials, with nanostructured thin film devices comprised of Bi_2Te_3 and Sb_2Te_3 having achieved zT values as high as 2.4 at room temperature.²⁰ However, its operation is limited to “low” temperature applications, up to about 200 °C.

Lead chalcogenides have been studied since the field of thermoelectrics emerged, and have demonstrated zT values well past 2.0 in the highest performing nanostructured devices.^{21,22} Lead chalcogenides exhibit greater thermal stability compared to bismuth telluride, and are most useful for mid-temperature applications between 200–600 °C. Although lead telluride is typically the focus for obtaining high zT values, doped lead selenide devices with zT values as high as 1.5 have also been developed.²³ Lead sulfide devices have attained zT values of 1.1 after doping while completely avoiding the use of antimony and tellurium.²⁴

An extension of lead chalcogenides, “LAST- m ” (lead-antimony-silver-tellurium) alloys, comprised of $(\text{PbTe})_m\text{-AgSbTe}_2$, are capable of reaching zT values as high as 2.2.²⁵ The origins of the high performance of LAST alloys are believed to be a result of its inhomogeneity at the nanoscale leading to substantially decreased thermal conductivity values.

Silicon–Germanium alloys are one of the best performing thermoelectric materials for high temperature (> 800 °C) operations. Their exceptional thermal stability has made them the

material of choice for a number of NASA's deep space exploration probes. Their nontoxicity and silicon's high natural abundance make SiGe alloys a more attractive alternative to other systems, however, achieving higher zT values comparable to the previously discussed systems has been difficult, due to the synthetic challenges associated with producing these materials, as well as their high thermal conductivity ($\sim 150 \text{ W m}^{-1} \text{ K}^{-1}$ at room temperature for bulk silicon).¹¹ Currently, the best values reported for SiGe alloys are approximately 1.3, for phosphorus-doped, nanostructured n-type materials.²⁶

Tellurium–Antimony–Germanium–Silver alloys, more commonly known as TAGS alloys, are an extension of germanium telluride thermoelectric materials, analogous to lead telluride and the LAST alloys. Their compositions are similarly tunable as $(\text{GeTe})_x(\text{AgSbTe}_2)_{1-x}$, where x is generally between 75-90%. TAGS alloys typically possess zT values ranging from 1.2 to 1.5, attaining maximum values around $500 \text{ }^\circ\text{C}$, making them one of the highest performing p-type materials known.²⁷

Half-Heusler alloys are a set of structurally complex intermetallic alloys, with the general formula ABC, where A and B are transition metals and C is either a metal or an *sp* metalloid. Structurally, these materials adopt a rock salt structure comprised of A and C, with the B atoms occupying half of the tetrahedral holes of the “A” atom FCC lattice, as in the zinc blende structure (Figure 1.5).²⁸ Compared to other systems, Half-Heusler alloys offer much more freedom in exploiting doping to fine tune electrical and thermal properties, as A, B, and C can all be doped independently. In the highest performing HH alloys, zT values of approximately 1 have been achieved for *n*-type materials, with further improvement possible through nanostructuring.²⁸ An added benefit of these alloys is their extremely good thermal stability, up to temperatures as

high as 900 °C, which, alongside SiGe alloys, makes them a viable choice for high temperature applications.

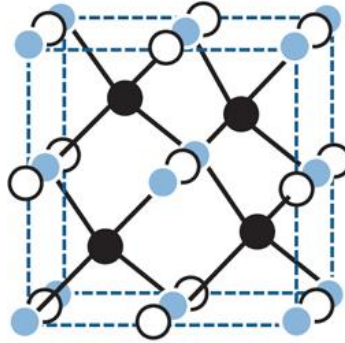


Figure 1.5 Crystal structure of Half-Heusler materials.²⁹

1.5 Modern Strategies for Improving Thermoelectric Performance

The mathematical descriptions of thermoelectric material performance outlined in the previous section highlight the two strategies for increasing the figure of merit: modifying the electrical properties of the material, or decreasing the thermal conductivity.

The first advent of thermoelectric materials design occurred in the 1950s, as the basic principles of the science were firmly established and the use of heavily-doped semiconductors was found to provide reasonable performance in devices. However, subsequent progress in producing higher zT values remained stagnant for the next 40 years. Then, the work of Hicks and Dresselhaus in 1993 proposing the use of quantum confinement as a way to improve zT values reignited the interest into developing new thermoelectric materials, resulting in the development of several materials displaying zT values of 1.5 or more.

Modification of Electronic Properties

Several methods for modifying the electrical properties of a material are available. As shown earlier in Figure 1.4, carrier concentration is critical to the overall power factor, and by extension, the ZT of a material. This value can be easily manipulated through doping of the material, as is ubiquitous in many semiconductor materials. However, pushing the carrier concentration too high eventually results in significant increases in thermal conductivity, which, when combined with the lowered Seebeck coefficient, results in a lower ZT. A variation on the doping concept, known as modulation doping, has been shown to improve power factor values above the levels of standard uniform doping.^{26,30,31} In contrast to the standard “uniform” doping approach, modulation doping begins with a two phase composite matrix, with dopant atoms introduced into only one of the two species. Mechanistically, charge carriers are believed to “spill over” from the doped species into the undoped matrix, resulting in ionization of the doped regions. In contrast to uniform doping, the sequestration of the ionized regions results in decreased scattering of the carriers and therefore, a higher mobility.

Nanostructuring of thermoelectric devices as a way to enhance the power factor of thermoelectric materials is principally responsible for the resurgence of interest and success that new materials have enjoyed. Using bismuth telluride, Bi_2Te_3 , the premier thermoelectric material up to that point, Hicks and Dresselhaus calculated that the introduction of nanostructures to produce quantum confinement effects could lead to substantially increased figure of merit values for bismuth telluride relative to the corresponding bulk material, due to changes in the electronic density of states in the nanostructured material.^{16,18,19} However, subsequent work showed that the improvement in thermoelectric performance was a result of increased phonon scattering at interfaces, as opposed to enhancement of the Seebeck coefficient.³²

A third method for manipulating the electrical transport properties involves the creation of potential energy barriers in nanocomposites comprised of a semiconductor matrix with metallic inclusions.³²⁻³⁴ At the junction between a semiconductor and a metal, a phenomenon known as band bending occurs, resulting from Fermi level pinning of surface states generated at the interface between the semiconductor and metal. The consequence of this band bending is the scattering of low energy, or “cold”, carriers without impediment of high energy “hot” carriers (Figure 1.6). This energy dependent scattering results in an increase in the Seebeck coefficient, but the introduction of these inclusions can also result in changes to other parameters, such as carrier mobility, and carrier concentration as well. However, any negative influences as a result of heterostructure inclusion are generally cancelled out by the increase in Seebeck coefficient. The scattering of low energy excited carriers also has the added benefit of reducing the thermal conductivity associated with those scattered carriers, which also contributes to the improvement in ZT.

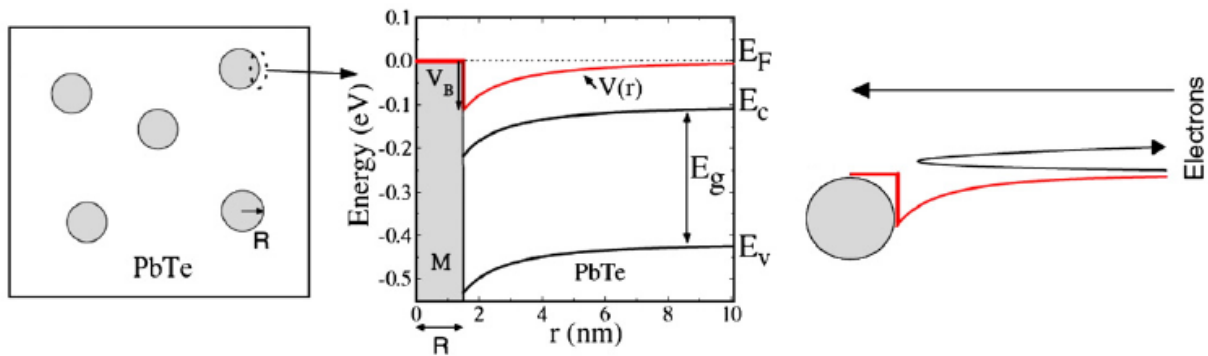


Figure 1.6 Example of energy filtering barriers through the inclusion of metallic Pb particles in a host PbTe matrix.³²

Modification of Thermal Conduction Properties

The development of approaches for reducing thermal conductivity have, in general, proven to be much easier to employ as a way to improve thermoelectric material performance. Among the different methods for decreasing thermal conductivity, alloying, which was first proposed in the 1950s, is one of the earliest and most easily employed techniques. This is the process of modifying an existing crystal lattice by introducing a different element in such a way as to either partially replace the host material (substitutional alloying) or insert into vacancies within the host's crystal lattice (interstitial alloying). Alloying isoelectronic elements into thermoelectric materials works by introducing disorder into the material at the atomic level, with the alloyed element functioning much like a point defect. The difference in mass of the alloyed constituents aids in phonon scattering, particularly for phonons that have short wavelengths, resulting in an overall decrease in lattice thermal conductivity without significantly impeding electrical performance.^{10,35} In general, the greater the mass difference between the matrix and alloying elements, the greater the effect on phonon propagation.

Another similar approach is to make use of materials with more complex crystal structures containing interstitial substitutions or large void spaces which can be filled with a variety of different atoms.^{10,36,37} As with alloying, the idea of atomic disorder and “rattling cages” are the principle mode of action for reducing phonon propagation. Skutterudites and clathrates are two prime examples for these types of crystal structures, and both have been the subject of extensive research as potential thermoelectric materials.^{37,38} Binary skutterudites of the form MX_3 , where M is a metal and X is a pnictogen, have received the most attention as potential thermoelectric materials. These are semiconducting cubic crystals containing 32 atoms per unit cell. Large void spaces exist within the unit cells, with radii that can exceed 2.0

Angstroms, making them suitable for hosting a wide array of guest atoms such as rare earth elements, to serve as rattling points for phonon scattering. In addition, these binary skutterudites also exhibit several other beneficial characteristics, such as heavy constituent atomic masses, a high degree of covalency among atoms, and large carrier mobilities. Clathrates are another type of host-guest structure. Inorganic clathrates exist in five different structural forms, but most interest for thermoelectric applications has been focused on those inorganic clathrates that fall into the Type-I structure.³⁷ Similar to skutterudites, clathrates also display semiconducting behavior, and contain a number of void spaces per unit cell that aid in scattering phonons.

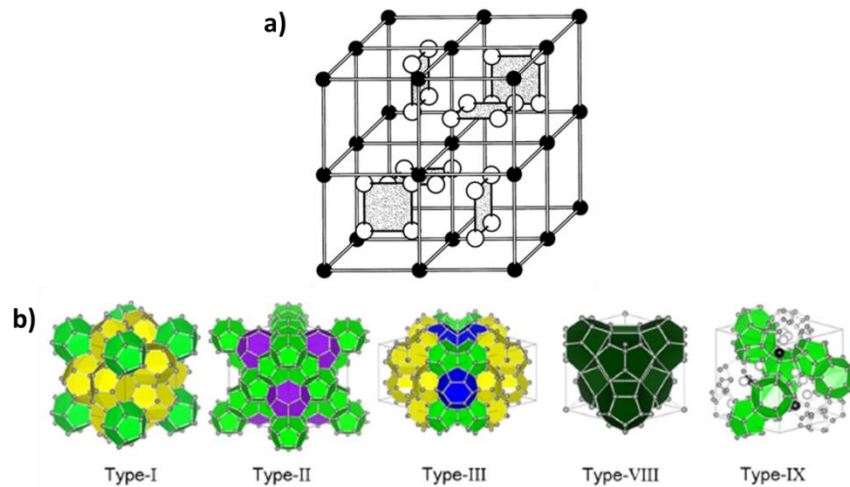


Figure 1.7 General crystal structures of a) skutterudites and b) clathrates.³⁷

The application of nanoscale engineering has revolutionized the landscape of thermoelectrics particularly when considering its effect on thermal conductivity.³⁹ The geometry of devices incorporating nanoscale domains can drastically reduce the mean free path of phonons without a significantly adverse effect charge carrier transport, resulting in significantly improved ZT values.^{10,11,40} The benefits of reducing grain size have been known and exploited for decades, and become apparent even before reduction down to nanoscale levels. For example,

polycrystalline silicon–germanium alloys exhibited a 28% decrease in thermal conductivity compared to single crystal samples when the average grain size was reduced below 5 μm , with no change in either the Seebeck coefficient or electrical conductivity values.⁴¹ When this concept was applied to nanoscale grain sizes, a full order of magnitude reduction in thermal conductivity for nanoscale silicon compared to bulk was measured. In addition, the use of nano-sized grains magnified the effect of germanium alloying, resulting in a zT of 0.95 at only 5 at.% Ge, on par with the performance of larger grained $\text{Si}_{0.8}\text{Ge}_{0.2}$ alloys.⁴²

In addition to their energy scattering effects for improving power factors, the incorporation of heterostructures has also been demonstrated to lead to decreased thermal conductivities. These effects have been well exemplified in “TAGS” (tellurium–antimony–germanium–silver) alloys and lead chalcogenide-based systems, such as “LAST” (lead–antimony–silver–tellurium) alloys and lead telluride, where lattice thermal conductivity values have been successfully reduced by more than 50%.^{25,43} The incorporation of these inclusions has the potential to improve the viability of materials that have been limited by high thermal conductivities, such as silicon and germanium. Spontaneous phase segregation of metastable states has also been used to produce complex heterostructures, such as the lamellar segregation of $\text{Pb}_2\text{Sb}_6\text{Te}_{11}$ into Sb_2Te_3 and PbTe .⁴⁴

From all the work that has been done on elucidating the factors that contribute to improving the performance of thermoelectric materials, two key factors are highlighted, which we aim to leverage in our studies:

- 1) Complexity at a number of different length scales is a useful tool for drastically reducing thermal conductivity, leading to improved performance. This can be

accomplished through methods such as alloying and fabricating devices from films of nanocrystalline material to introduce a large number of grain boundaries.

- 2) The introduction of metallic heterostructures can lead to an energy filtering effect, eliminating “cold” charge carriers and increasing the overall thermopower of the material.

1.6 Thesis Objectives

In comparison to other thermoelectric materials, there are several advantages to employing the use of silicon–germanium alloys, particularly with regard to envisioning any large-scale adoption for public use. The greater availability of silicon and germanium compared to other popular choices such as tellurium, selenium, and bismuth makes them a more practical choice. In addition, the established silicon industry would aid in transitioning from laboratory to large scale processing.

Despite these advantages, significant synthetic challenges associated with Group IV materials synthesis have limited investigations into improving the performance of silicon–germanium alloy thermoelectrics through the various strategies described earlier in this chapter. Many of the existing protocols for Group-IV materials are discriminatory to either silicon-only or germanium-only products, and those few procedures that have been demonstrated for the production of alloys of the two require the use of specialized equipment that may or may not be amenable to large scale production. Solution-phase syntheses provide a number of advantages in reaction scalability, flexibility, and tunability compared to alternative vapor and solid state reactions. The expansion of current solution-phase synthetic protocols for the production of Group-IV nanomaterials to encompass silicon–germanium alloys and other Group-IV-based

nanomaterials would represent an important advancement in silicon and germanium materials synthesis, and is an important prerequisite step for the creation of solution processed silicon and germanium devices.

The goals of the work here are to provide a synthetic foundation from which a variety of Group IV-based nanomaterials can be produced. By developing new synthetic protocols for the production of silicon–germanium alloys and metal germanide and silicide materials, we aim to further expand the synthetic toolbox available for the production of Group IV materials and uncover new insight into the parameters that influence their resultant properties, particularly with regards to metal germanides and silicides, as the conditions for their production are not firmly established with regards to solution phase syntheses. With the knowledge gained here, the materials needed for the production of a variety of Group IV-based films will be accessible, paving the way for subsequent investigations into the performance of alloyed SiGe films, as well as heterostructured films of semiconductor nanocrystals and metal silicides or germanides (Figure 1.8); an area that has yet to be explored by the scientific community. It is our hope that these investigations will provide additional momentum towards the larger scale adoption of silicon and germanium thermoelectrics for real world applications.

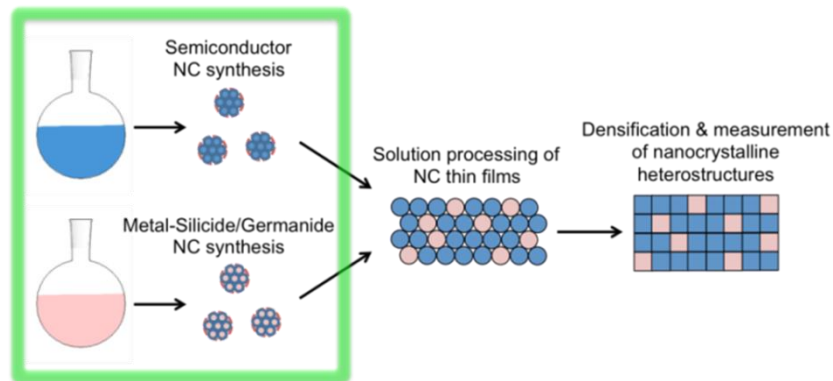


Figure 1.8 Outline of the fabrication of solution-processed Group IV-based devices for evaluation as thermoelectric materials. This dissertation focuses on the materials synthesis aspects of the project.

The next chapter will discuss two different synthetic approaches for attempts to produce silicon–germanium alloy nanocrystals, one drawing from high temperature methodologies used in silicon and germanium nanocrystal synthesis, and the other utilizing a room-temperature approach. Chapter three will discuss the adaptation of an existing germanium nanocrystal synthetic method for the production of metal germanide nanocrystals, as well as the production of heterostructured silicon/nickel–silicide nanowire arrays from an established silicon nanowire synthetic method.

The final two chapters will cover a separate body of work, unrelated to chapters 2 and 3. Chapter four will present work into the synthesis of isolable alkenylgold(I) complexes through the use of a hitherto unreported transmetalation reaction between zirconium and gold. Finally, chapter five will discuss the development of a new experimental setup for use with single-molecule microscopy, and its use in the real-time imaging of a platinum–sulfur bond formation reaction.

1.7 References

- (1) LaMer, V. K.; Dinegar, R. H. *J. Am. Chem. Soc.* **1950**, *72*, 4847-4854.
- (2) Yin, Y.; Alivisatos, A. P. *Nature* **2005**, *437*, 664-670.
- (3) Chang, J.; Waclawik, E. R. *RSC Advances* **2014**, *4*, 23505.
- (4) Steigerwald, M. L.; Alivisatos, A. P.; Gibson, J. M.; Harris, T. D.; Kortan, R.; Muller, A. J.; Thayer, A. M.; Duncan, T. M.; Douglass, D. C.; Brus, L. E. *J. Am. Chem. Soc.* **1988**, *110*, 3046-3050.
- (5) Brus, L. *J. Phys. Chem.* **1986**, *90*, 2555-2560.
- (6) Brus, L. E. *J. Chem. Phys.* **1984**, *80*, 4403.
- (7) Lines, M. G. *J. Alloy. Compd.* **2008**, *449*, 242-245.
- (8) de Mello Donega, C. *Chem. Soc. Rev.* **2011**, *40*, 1512-1546.
- (9) Dasog, M.; De los Reyes, G. B.; Titova, L. V.; Hegmann, F. A.; Veinot, J. G. C. *ACS Nano* **2014**, *8*, 9636-9648.
- (10) Snyder, G. J.; Toberer, E. S. *Nat. Mater.* **2008**, *7*, 105-114.
- (11) Hochbaum, A. I.; Chen, R.; Delgado, R. D.; Liang, W.; Garnett, E. C.; Najarian, M.; Majumdar, A.; Yang, P. *Nature* **2008**, *451*, 163-167.
- (12) BCS Inc. *Waste Heat Recovery- Technologies and Opportunities in U.S. Industry* 2008.
- (13) Bulusu, A.; Walker, D. G. *Superlattice. Microst.* **2008**, *44*, 1-36.
- (14) *CRC Handbook of Thermoelectrics*; CRC Press: Washington D. C., 1995.
- (15) Baranowski, L. L.; Jeffrey Snyder, G.; Toberer, E. S. *J. Appl. Phys.* **2013**, *113*, 204904.
- (16) Pichanusakorn, P.; Bandaru, P. *Mat. Sci. Eng. R* **2010**, *67*, 19-63.
- (17) Dresselhaus, M. S.; Chen, G.; Tang, M. Y.; Yang, R. G.; Lee, H.; Wang, D. Z.; Ren, Z. F.; Fleurial, J. P.; Gogna, P. *Adv. Mater.* **2007**, *19*, 1043-1053.

- (18) Hicks, L. D.; Dresselhaus, M. S. *Phys. Rev. B* **1993**, *47*, 12727-12731.
- (19) Hicks, L. D.; Harman, T. C.; Dresselhaus, M. S. *Appl. Phys. Lett.* **1993**, *63*, 3230.
- (20) Venkatasubramanian, R.; Silvola, E.; Colpitts, T.; O'Quinn, B. *Nature* **2001**, *413*, 597-602.
- (21) LaLonde, A. D.; Pei, Y.; Wang, H.; Snyder, J. G. *Mater. Today* **2011**, *14*, 526-532.
- (22) Heremans, J. P.; Thrush, C. M.; Morelli, D. T. *J. Appl. Phys.* **2005**, *98*, 063703.
- (23) Lee, Y.; Lo, S. H.; Chen, C.; Sun, H.; Chung, D. Y.; Chasapis, T. C.; Uher, C.; Dravid, V. P.; Kanatzidis, M. G. *Nat. Commun.* **2014**, *5*, 3640.
- (24) Zhao, L. D.; Lo, S. H.; He, J.; Li, H.; Biswas, K.; Androulakis, J.; Wu, C. I.; Hogan, T. P.; Chung, D. Y.; Dravid, V. P.; Kanatzidis, M. G. *J. Am. Chem. Soc.* **2011**, *133*, 20476-20487.
- (25) Quarez, E.; Hsu, K.-F.; Pcionek, R.; Frangis, N.; Plochoniadis, E. K.; Kanatzidis, M. G. *J. Am. Chem. Soc.* **2005**, *127*, 9177-9190.
- (26) Yu, B.; Zebarjadi, M.; Wang, H.; Lukas, K.; Wang, H.; Wang, D.; Opeil, C.; Dresselhaus, M.; Chen, G.; Ren, Z. *Nano Lett.* **2012**, *12*, 2077-2082.
- (27) Levin, E. M.; Bud'ko, S. L.; Schmidt-Rohr, K. *Adv. Func. Mater.* **2012**, *22*, 2766-2774.
- (28) Xie, W.; Weidenkaff, A.; Tang, X.; Zhang, Q.; Poon, J.; Tritt, T. *Nanomater.* **2012**, *2*, 379-412.
- (29) Lin, H.; Wray, L. A.; Xia, Y.; Xu, S.; Jia, S.; Cava, R. J.; Bansil, A.; Hasan, M. Z. *Nat. Mater.* **2010**, *9*, 546-549.
- (30) Zebarjadi, M.; Joshi, G.; Zhu, G.; Yu, B.; Minnich, A.; Lan, Y.; Wang, X.; Dresselhaus, M.; Ren, Z.; Chen, G. *Nano Lett.* **2011**, *11*, 2225-2230.

- (31) Dingle, R.; Störmer, H. L.; Gossard, A. C.; Wiegmann, W. *Appl. Phys. Lett.* **1978**, *33*, 665.
- (32) Medlin, D. L.; Snyder, G. J. *Curr. Opin. Colloid In.* **2009**, *14*, 226-235.
- (33) Zhang, Z.; Yates, J. T., Jr. *Chem. Rev.* **2012**, *112*, 5520-5551.
- (34) Neophytou, N.; Kosina, H. *J. Appl. Phys.* **2013**, *114*, 044315.
- (35) Wright, D. A. *Nature* **1958**, *181*, 834.
- (36) Zhang, Y.; Stucky, G. D. *Chem. Mater.* **2014**, *26*, 837-848.
- (37) Takabatake, T.; Suekuni, K.; Nakayama, T.; Kaneshita, E. *Rev. Mod. Phys.* **2014**, *86*, 669-716.
- (38) Nolas, G. S.; Morelli, D. T.; Tritt, T. M. *Annu. Rev. Mater. Sci.* **1999**, *29*, 89-116.
- (39) Pernot, G.; Stoffel, M.; Savic, I.; Pezzoli, F.; Chen, P.; Savelli, G.; Jacquot, A.; Schumann, J.; Denker, U.; Monch, I.; Deneke, C.; Schmidt, O. G.; Rampnoux, J. M.; Wang, S.; Plissonnier, M.; Rastelli, A.; Dilhaire, S.; Mingo, N. *Nat. Mater.* **2010**, *9*, 491-495.
- (40) Liu, W.; Yan, X.; Chen, G.; Ren, Z. *Nano Energy* **2012**, *1*, 42-56.
- (41) Rowe, D. M.; Shukla, V. S.; Savvides, N. *Nature* **1981**, *290*, 765-766.
- (42) Zhu, G. H.; Lee, H.; Lan, Y. C.; Wang, X. W.; Joshi, G.; Wang, D. Z.; Yang, J.; Vashaee, D.; Guilbert, H.; Pillitteri, A.; Dresselhaus, M. S.; Chen, G.; Ren, Z. F. *Phys. Rev. Lett.* **2009**, *102*, 196803.
- (43) Hsu, K.-F.; Loo, S.; Guo, F.; Chen, W.; Dyck, J. S.; Uher, C.; Hogan, T.; Polychroniadis, E. K.; Kanatzidis, M. G. *Science* **2004**, *303*, 818-821.
- (44) Ikeda, T.; Collins, L. A.; Ravi, V. A.; Gascoin, F. S.; Haile, S. M.; Snyder, G. J. *Chem. Mater.* **2007**, *19*, 763-767.

Chapter 2: The Synthesis of Silicon–Germanium Alloy

Nanocrystals

2.1 Introduction

Silicon and germanium nanomaterials have been a constant source of interest for researchers for their potential applications in a number of technological areas. However, significant synthetic hurdles such as high crystallization temperatures, oxygen and moisture sensitivity, and limited surface functionalization options have made mastery over development of these materials an ongoing challenge.

More recently, alloys of silicon and germanium have garnered increased attention as promising materials. In comparison to many other alloy systems, silicon and germanium offer the rare advantage of being entirely miscible in the solid state, allowing for compositional tuning as a route to manipulating optoelectronic properties rather than relying on size alone, making these a potentially useful class of materials for a variety of applications.¹⁻⁷ However, the controlled creation of these alloys requires taking an already challenging synthetic system and developing procedures to smoothly incorporate both elements. In this chapter, the results of two different attempts- a high temperature approach and a room temperature approach- will be presented.

2.2 The Properties of Silicon and Germanium

The success of the semiconductor industry is inextricably linked with silicon, beginning with the creation of the first silicon-based chip in 1961. Silicon is an indirect band gap material, with a Bohr exciton radius of approximately 4.9 nm and band gap of approximately 1.12 eV for bulk material, with the lowest energy direct gap transition measuring approximately 3.4 eV.⁸ The indirect nature of silicon's band gap necessitates the need for a phonon-assisted pathway for release of a photon, resulting in poor photoluminescence for silicon-based materials. Despite this, photoluminescence has been observed from silicon nanostructures, beginning with Canham's work on porous silicon in 1990.⁹ Since then, luminescence from silicon nanostructures spanning the entire visible spectrum has been successfully demonstrated.^{10,11} It has been observed that upon reaching extremely small sizes (around 1-2 nm) silicon's band structure changes and exhibits pseudo-direct behavior.¹² Silicon crystallizes in the diamond cubic structure, with a lattice parameter of 5.431 Angstroms. The diamond cubic lattice (shown in Figure 2.1) is best described as two interpenetrating FCC lattices offset by $\frac{1}{4}$ of the lattice parameter in the x, y, and z directions. Silicon's electron and hole mobilities are $\sim 1400 \text{ cm}^2\text{V}^{-1}\text{s}^{-1}$ and $450 \text{ cm}^2\text{V}^{-1}\text{s}^{-1}$ respectively.⁸ Bulk silicon's high thermal conductivity of approximately $150 \text{ Wm}^{-1}\text{K}^{-1}$ at room temperature is problematic for its use in thermoelectric materials, for the reasons outlined in Chapter 1.

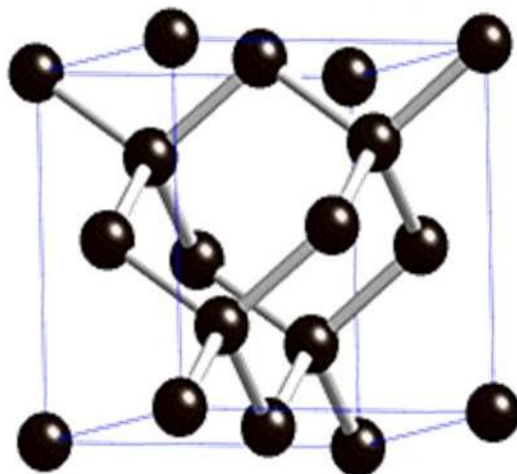


Figure 2.1 Diamond cubic crystal structure.

Germanium, which shares several similarities to silicon, was the original material of choice for semiconductor devices. It also crystallizes in the diamond cubic motif, with a larger lattice constant of 5.658 Angstroms. It is also an indirect band gap material, with a bulk band gap of only 0.67 eV. Unlike silicon, the smallest direct band gap transition is only slightly higher in energy than its indirect gap, at 0.8 eV. Germanium's Bohr exciton radius of ~10 nm is also significantly larger than in silicon. Photoluminescence from germanium nanomaterials is also very well known, and has been demonstrated to span a large portion of the visible spectrum as with silicon, extending out into the near-infrared region as well.¹³ In stark contrast to silicon, germanium does not form a stable oxide layer, which, in addition to its lower abundance compared to silicon, has been a principal reason that it has not seen more use in the semiconductor industry. Germanium's electron ($\sim 3900 \text{ cm}^2\text{V}^{-1}\text{s}^{-1}$) and hole ($\sim 1900 \text{ cm}^2\text{V}^{-1}\text{s}^{-1}$) mobilities are both significantly higher than in silicon. Its thermal conductivity is significantly lower than that of silicon, roughly $60 \text{ Wm}^{-1}\text{K}^{-1}$ at room temperature.⁸

2.3 Synthetic Approaches for Silicon Nanomaterials

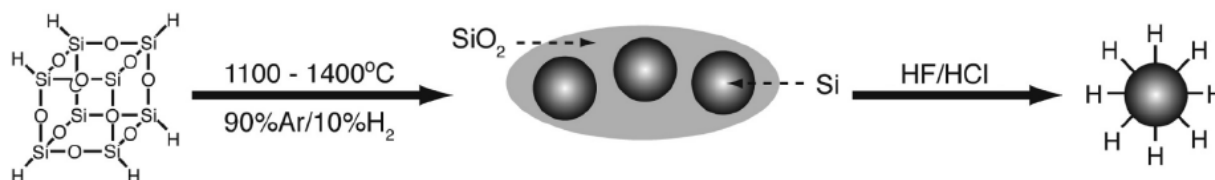
Since the discovery of room temperature photoluminescence from silicon nanocrystals in 1990, interest in the optical and electrical properties of nanoscale silicon has grown exponentially.⁹ Consequently, an incredibly diverse set of synthetic approaches for the production of silicon nanomaterials has evolved.¹⁴ Solid, liquid, and gas phase reactions have all been successfully utilized, with each system presenting different advantages and drawbacks.

High energy ball milling of silicon powder has been utilized in the production of silicon nanocrystals as small as 2–5 nanometers.¹⁵⁻¹⁷ Silicon oxide can be used as a precursor when an external reducing agent such as aluminum, graphite, or magnesium is included in the milling process.^{16,18} Ball milling also offers the advantage of large scale nanocrystal production. However, the products produced from this approach are often polydisperse, and there is evidence that a crystalline to amorphous transformation can also occur during the milling process.^{19,20}

Etching bulk silicon wafers to produce porous silicon and silicon nanowire arrays has remained popular since Canham's seminal work in 1990.⁹ Several variations on the procedure exist, making use of electrochemical, chemical, and metal assisted electroless etching processes.^{11,21,22} These procedures are very useful for the production of well-ordered nanomaterials, but, like other top-down synthetic approaches, their overall yield is limited and they require high quality silicon wafers as their source material, which are not inconsequential to produce. This process is described in more detail in Chapter 3.

Thermal decomposition of sol-gel precursors such as hydrogen silsesquioxane or hydrolyzed trichlorosilane is another very popular method for silicon nanocrystal production (Scheme 2.1).^{11,18,23-25} Very monodisperse, size-controlled products are produced, which, when

etched to remove the SiO₂ matrix byproduct, can be easily and cleanly isolated and passivated to produce particles between 1-20 nm in diameter. Unfortunately, the overall utility of this method is limited by the low yield of nanocrystal products, as much of the silicon content from the precursor is lost as part of the oxide matrix.



Scheme 2.1 Thermal decomposition of hydrogen silsesquioxane to produce silicon nanocrystals.²⁵

The use of non-thermal plasmas for the decomposition of silane and/or silicon tetrachloride has been shown to produce high quality, monodisperse silicon nanocrystals in the range of 1-10 nm which are terminated with either hydrogen or chloride, depending on the precursor choice.^{26,27} However, in addition to the limited throughput and specialized equipment required, the final products from the reaction are prone to aggregation while in the reaction vessel. Subsequent surface functionalization has been demonstrated through hydrosilylation and Grignard reactions to produce soluble, passivated nanocrystals.

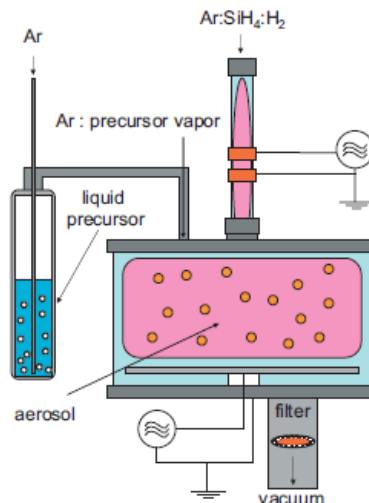


Figure 2.2 Outline of non-thermal plasma nanocrystal synthesis reaction setup.²⁸

Laser pyrolysis of silane is also capable of producing silicon nanocrystals between 1-10 nm in diameter.²⁹ Similar to the use of non-thermal plasmas, this reaction produces good quality products, but is limited in throughput and very energy intensive. The ability to manipulate the size of the resulting products is also not straightforward, and size control through this synthetic method is a result of variation of the etching conditions used in the subsequent processing steps.

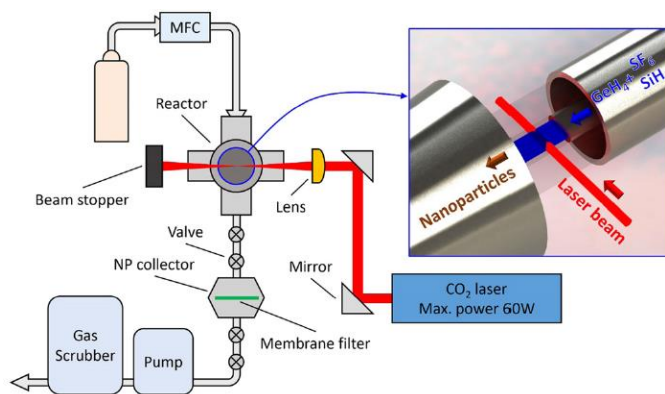
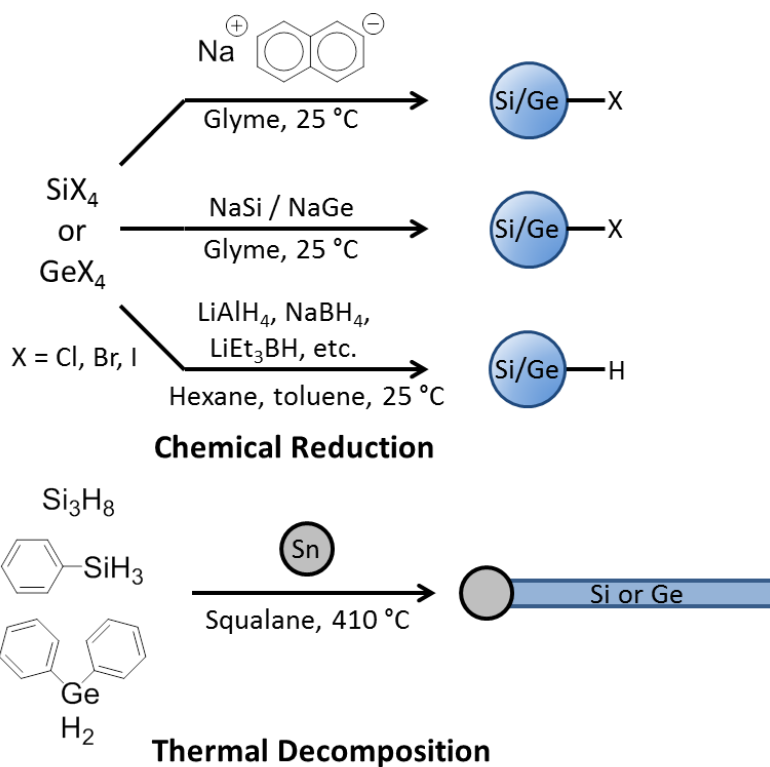


Figure 2.3 Outline of laser pyrolysis apparatus for nanocrystal synthesis.³⁰

Colloidal syntheses of silicon nanocrystals generally fall under two different approaches: low temperature reduction of silicon halides or high temperature decomposition of organosilanes (Scheme 2.2). The first colloidal synthesis of silicon nanocrystals was reported by Heath in 1992, and involved the reduction of silicon tetrachloride and octyltrichlorosilane at high pressure and temperature in supercritical hexane using a dispersion of sodium metal as the reductant.³¹ This yielded extremely polydisperse crystals ranging from 5 nm up to 3 microns.



Scheme 2.2 Colloidal approaches to Si and Ge nanomaterials synthesis.

High temperature syntheses require temperatures of 400 °C or greater, and are generally accomplished using non-coordinating hydrocarbons solvents such as squalane in conjunction with organosilanes such as phenylsilane or trisilane.³² Introduction of the precursors to the hot solvents induces rapid decomposition, yielding elemental silicon. In order to avoid aggregation, a

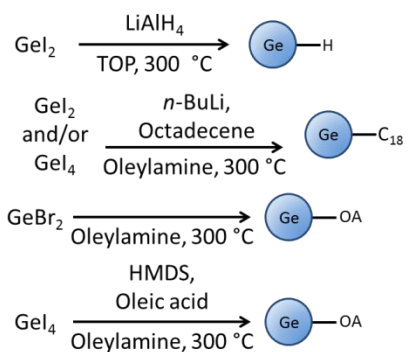
solution-liquid-solid approach is generally employed, which involves the use of seed nanoparticles, such as gold or tin.³³⁻³⁵ As the silicon precursor decomposes, it diffuses into the seed materials, and after becoming saturated, the silicon is extruded from the seed to produce highly crystalline silicon nanowires. Subsequent etching can be used to remove the undesired seed nanocrystals and yield hydride terminated nanowires suitable for passivation through hydrosilylation.

Room temperature colloidal syntheses of silicon nanocrystals have been accomplished through a variety of conditions. These syntheses, which are generally performed in ethereal solvents, hexane, or toluene, involve the reaction of a silicon tetrahalide with any of a number of reductants. Zintl salts, such as NaSi and MgSi, and alkali naphthalides have both been used successfully to produce silicon nanoparticles ranging from 3-10 nm.^{36,37} Functionalization of the particles, which are natively halide terminated, has been accomplished through reactions with Grignard reagents or through alkoxylation through addition of an alcohol.^{38,39}

In conjunction with quaternary alkylammonium salts, similarly sized products can also be produced using hydride-based reducing agents, such as lithium aluminum hydride (LiAlH₄) and sodium borohydride (NaBH₄), although care must be taken with these approaches, as the production of silane gas is possible, which can not only decrease overall yield, but also present a safety hazard.⁴⁰⁻⁴² These particles are hydride terminated as synthesized, and platinum catalyzed hydrosilylation is generally employed for functionalization, although UV-light has also been demonstrated to be a viable alternative.⁴⁰ Small changes in particle size have been demonstrated through tuning of the surfactant alkyl chain length, though the overall sizes of particles produced through this route are still limited to 1-10 nm.

2.4 Synthetic Approaches for Germanium Nanomaterials

Germanium nanomaterials have been synthesized through several of the same approaches that have been employed for silicon^{33,43-48} Gas-phase syntheses utilizing nonthermal plasmas and laser pyrolysis have been used to produce germanium nanocrystals analogously to the methods used for silicon.^{49,50} However, several different solution routes not seen with silicon have also been established (Scheme 2.3), using coordinating amine and phosphine solvents.^{13,51,52} High boiling point amines such as oleylamine are effective for producing nanocrystals from germanium halide precursors.^{53,54} Germanium differs from silicon in having a stable +2 oxidation state that is more easily reduced down to Ge(0), although germanium tetrahalides still require the aid of a powerful reducing agent. This has allowed for syntheses where oleylamine has served as solvent, reductant, and capping ligand all in one, without the need for a separate strong reducing agent as with silicon.^{52,55,56} Reduction is believed to occur through a mixed amine/halide intermediate, although no specific mechanistic studies have been performed to support this hypothesis.⁵⁷ Expanding this system through the use of mixed Ge(II/IV) precursor ratios has been shown to be a useful approach for controlling the size of the resulting products.¹³



Scheme 2.3 Germanium specific colloidal syntheses.

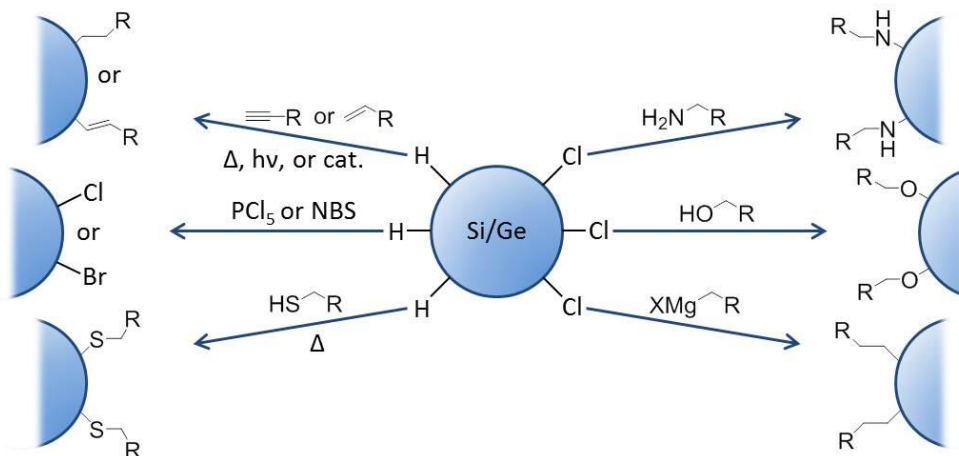
2.5 Synthetic Approaches for Silicon–Germanium Alloy Nanomaterials

Despite the large variety of synthetic methods that have been used for the production of pure silicon and germanium nanomaterials, methods for the production of alloys of the two elements are much less common. Ball milling of mixed silicon and germanium powders has been used to produce SiGe alloys, but as with the pure elements, this method produces extremely polydisperse products and requires extensive workup in acidic conditions to remove contaminating oxide and byproducts.⁵⁸ High temperature solid state reductions of mixed silsesquioxane and germanium halide precursors have been shown to be somewhat useful in producing alloyed products.⁵⁹ Although this is an excellent method for producing pure silicon nanocrystals (Scheme 2.1), it was found that the resulting products from the reduction of hydrogen silsesquioxane and germanium(II) iodide led to particles containing silicon rich and germanium rich regions, rather than resulting in even alloying. Sputtered films prepared from silicon and germanium have been used to produce monodisperse nanocrystals after subsequent annealing and etching steps.⁶⁰ This method also allows for incorporating dopants such as boron and phosphorus into the resulting products. However, this synthetic approach is very energy intensive and limited in throughput. Laser pyrolysis and plasma assisted decomposition of silane and germane have been shown to produce high quality alloy nanocrystals, similar to its use for both pure elements, with a high degree of control over elemental composition.^{30,61-63} Traditional vapor-liquid-solid synthesis techniques have also been useful for producing SiGe nanowires.⁶⁴ Despite all these advances in SiGe alloy synthesis, a colloidal approach to nanoscale products has remained elusive.

2.6 Functionalization of Silicon and Germanium Surfaces

Proper functionalization of silicon and germanium surfaces is crucial to maintaining their desired properties. Both silicon and germanium oxidize readily in air, which can result in significant changes to their optoelectronic properties.^{10,23,65,66} This is especially problematic for germanium due to the instability of its oxide and its solubility in water.⁶⁷ Ligand choice is especially important when considering nanoparticle systems, as they will dictate the solubility properties of the particles they are bound to, and can also impact the performance of devices fabricated from the particles. In addition, the luminescence properties of these particles are inextricably linked to their surface chemistry, enabling luminescence across the entire visible spectrum.^{10,68-70}

The bulk of known surface passivation methodologies for silicon and germanium relate to the chemistry of hydride and halide terminated surfaces; the former are the result of reductions in hydrogen containing atmospheres, from hydride reducing agents, or as the result of etching with hydrofluoric acid, while the latter can be attained through the reductions of tetrahalides using radical or Zintl salt approaches.⁷¹ Halide surfaces can also be generated through the reaction of hydride terminated surfaces with halogenating agents such as phosphorus pentachloride (PCl₅), or *N*-bromosuccinimide (NBS).^{10,72} Scheme 2.4 summarizes some of the more important surface reactions that have been reported.



Scheme 2.4 Surface modification approaches for silicon and germanium nanocrystals.

Hydride terminated surfaces for both silicon and germanium are known to react with alkenes and alkynes through addition across the unsaturated bond; a reaction referred to as hydrosilylation (or hydrogermylation).¹⁰ This addition generally occurs in an anti-Markovnikov fashion, and results in the formation of a new silicon–carbon or germanium–carbon bond. These alkyl layers are very effective at preventing surface oxidation. Unfortunately, this stability also means it is extremely difficult to remove such ligands from the surface once they have been attached. Alkylated surfaces can provide an effective barrier against oxidation for surfaces exposed to ambient conditions on timescales as long as months.

A variety of different approaches have been utilized for the alkylation of hydride surfaces. In the absence of any catalysts, functionalization can be accomplished at temperatures above 150 °C.^{73,74} Though effective, this limits the scope of viable ligands to longer chain hydrocarbons, which, although effective for producing soluble, oxidatively stable products, are not ideal when attempting to create electrically conductive devices.

Several metal catalysts have also been used to catalyze hydrosilylation.⁷⁵ Among these, platinum catalysts are the most widely utilized.^{40,41,44} Mechanistically, the most widely accepted

mode of action is through the Chalk–Harrod mechanism (Scheme 2.6), wherein the platinum catalyst inserts into the silicon–hydride bond first in an oxidative addition. Next, a pi-complex is formed with the alkene or alkyne, which then undergoes a migratory insertion with the Pt–hydride generated in the first step. Finally, reductive elimination regenerates the original platinum catalyst and releases the product, containing the newly formed silicon–carbon bond.^{76,77}

Some success has also been achieved using Lewis acids as catalysts in place of more traditional metal catalysts.^{75,78} This is especially important, given that trace metal contamination remaining from the catalysts can affect the optoelectronic properties of the particles they are attached to. Borane, aluminum trichloride, tris(pentafluorophenyl)borane and ethylaluminum dichloride have all been utilized successfully as catalysts for room temperature alkylation.^{78,79} The proposed mechanism of action of these catalysts is through coordination to the unsaturated carbon–carbon bond, increasing their electrophilicity and making them more susceptible to nucleophilic attack from the hydride, which in turn facilitates attachment of the alkyl chain to the silicon or germanium surface. However, more work into the role of these catalysts is needed, as it has been observed that there are substantial differences in performance of various catalysts depending on the nature of the material surface being functionalized.

Ultraviolet light has also been employed as a promoter for the room temperature alkylation of hydride-terminated silicon and germanium nanocrystals. Both radical and exciton mediated pathways have been proposed as reaction mechanisms.⁸⁰⁻⁸² Compared to other approaches, UV mediated functionalization is extremely attractive for its comparatively fast reaction times, mild conditions, and compatibility with a wide range of synthetic systems. Unfortunately, the success of UV light as a promoter is size dependent in regard to the particles being functionalized, potentially limiting its overall usefulness.⁸¹

Thiols have also been successfully used as surface ligands for hydride-terminated silicon and germanium, generating alkylated surfaces through the formation of surface silicon–sulfur and germanium–sulfur bonds.^{23,83} Thermal functionalization is currently the only approach that has been reported; successful functionalization of germanium has been accomplished as low as 80 °C, but silicon functionalization has only been reported at significantly higher temperatures, around 190 °C, similar to the conditions used for thermal hydrosilylation. The resulting thiolate protected surfaces are effective for preventing oxidation of germanium materials, but silicon surfaces are still prone to oxidation over extended periods of exposure to air.

Halide-terminated surfaces are equally valuable synthetic handles as hydride terminated surfaces. Although halide terminated surfaces are still extremely prone to oxidation, particles bearing halide surface ligands can still form stable colloidal solutions when dispersed into hard donor solvents, and could provide a useful starting point for device or film fabrication prior to a passivation step.^{26,84}

Halide terminated surfaces are highly reactive, and can be exchanged at room temperature using a variety of ligands.⁸⁵ Alkylation of halide terminated surfaces can be obtained through introduction of a Grignard reagent. Similarly, the introduction of alcohols or amines results in the formation of alkoxy- or amine- terminated surfaces with concurrent liberation of HX (X = Cl, Br).^{36,86} This approach has been used in combination with conjugated amines as a way to improve the photoluminescence quantum yields of silicon nanocrystals.⁸⁶

2.7 Results and Discussion

Investigations of Silicon–Germanium Nanocrystal Synthesis in High Boiling Point Solvents

Colloidal syntheses for germanium and silicon nanocrystals can be roughly divided into two different classes: low and high temperature syntheses. Our initial work with high temperature syntheses of pure germanium nanocrystals in oleylamine following a previously established method provided monodisperse, crystalline products, and seemed to be an ideal starting point for incorporating silicon. In general, the synthetic procedure involved heating a solution of germanium(II) iodide and germanium(IV) iodide in dry oleylamine under nitrogen. Reduction of the germanium(II) iodide as the reaction was heated produced Ge(0) seed crystals. Upon reaching 200 °C, a solution of the strong reducing agent n-butyllithium in octadecene was added to facilitate reduction of the remaining germanium precursors. Continued heating to 300 °C provided time for the nanocrystals to grow and also resulted in exchange of the surface bound amine for octadecyl groups from the octadecene. Omission of the octadecene does not preclude the production and isolation of germanium nanocrystals, and simply results in oleylamine-capped nanocrystals, which display similar behavior to the octadecyl-capped particles, but were prone to aggregation and loss of solubility with repeated washing. The products are shown in Figure 2.4.

Our first attempt at synthesizing silicon–germanium alloy nanocrystals involved introducing silicon(IV) iodide into the reaction using the previously established conditions. Since silicon and germanium form a solid solution, and both exist in the diamond cubic crystal structure, successful incorporation of silicon should result in an observable shift in 2-theta values associated with different lattice planes in x-ray diffraction; a phenomenon known as Vegard's law. Unfortunately, no shift was observed relative to the pure germanium products as silicon

content was increased, even when increasing silicon content up as high as 50%, suggesting that silicon was not being incorporated into the products. This was further corroborated by the lack of any isolable products from the silicon-only version of the reaction. A gradual decrease in overall crystallinity was also observed as silicon content was increased, suggesting that the formation of germanium nanocrystals was also being impacted.

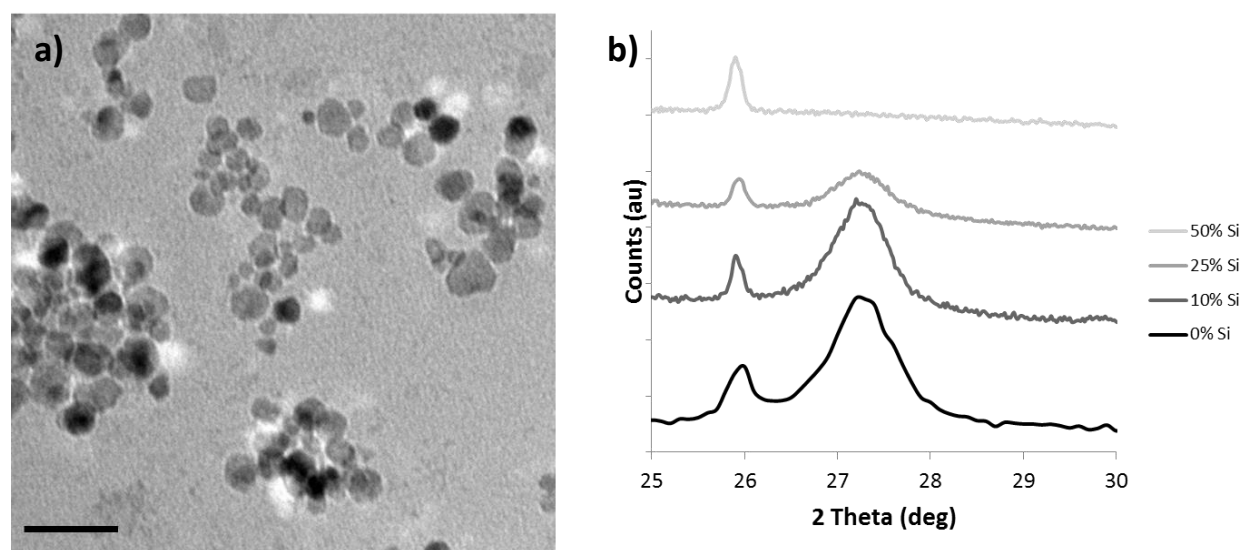


Figure 2.4 a) TEM of Ge nanocrystals from oleylamine and *n*-BuLi (50 nm scalebar) and b) XRD close up of (111) plane of Ge / SiGe alloy reactions. The peak at 26° is GeO_2 .

Silicon and germanium halides are known to form very complex coordination complexes with electron donating solvents, which can involve direct exchange with the halide ligands as well as outer sphere coordination complexes.⁸⁷⁻⁸⁹ Unfortunately, little is known about the reactivity of these complexes, although research is still ongoing. Coordination complexes with silicon are of particular interest for their potential access to stable Si(II) compounds, such as has been achieved with the use of N-heterocyclic carbenes. However, complexes with other ligands have demonstrated a remarkable resilience to reduction, as was demonstrated in Levason and

coworker's report on phosphine complexes of silicon tetrahalides. In their work, their attempts to reduce the complexes obtained by combining silicon tetrachloride with chelating diphosphines such as 1,2-bis(dimethylphosphino)ethane were unsuccessful even when employing reductants such as potassium on graphite (KC_8) and sodium naphthalide.⁸⁷ Reaction of the silicon precursor with oleylamine to form a stable silyl amine complex may preclude its reduction to nanocrystal products and explain its lack of incorporation in these experiments.⁹⁰

Because of the difficulty we observed with the use of coordinating solvents, we turned out attention to the use of the non-coordinating solvent squalane (2,6,10,15,19,23-hexamethyltetracosane). Squalane is the solvent generally employed for the high temperature decomposition of organosilanes and germanes employed in silicon and germanium nanowire synthesis. Under similar reaction conditions, replacing oleylamine with squalane led to the production of observable nanoparticles for silicon, germanium, and all attempted ratios of the two (Figure 2.5). Briefly, silicon and/or germanium tetrahalides were added to squalane and heated to 250 °C at a constant rate under nitrogen. A solution of n-butyllithium in either octadecene or squalane (2 equiv. relative to total halide content) was injected into the reaction, resulting in rapid production of a brown solid. After recovering to 250 °C, the reaction was heated to 300 °C before being cooled to room temperature. Freestanding particles of comparable size were observed with the tetrachlorides and tetrabromides, with lattice fringes observable using HRTEM. For all conditions, a large amount of aggregated byproducts were observed, and were intermixed with the particles, preventing isolation of clean products. In contrast to the tetrachloride and tetrabromide, the tetraiodides consistently yielded large aggregates of material.

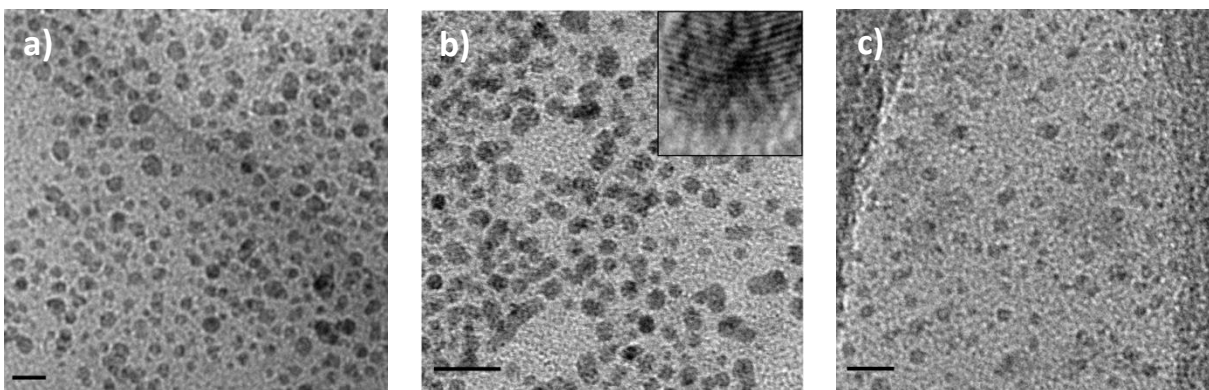


Figure 2.5 TEM images of a) Si, b) 1:1 Si:Ge (with inset HRTEM displaying lattice fringes), and c) Ge nanocrystals. Scalebars for low res images are 10 nm.

Raman spectroscopy (Figure 2.6) of the reactions for silicon and germanium confirm the presence of Si–Si and Ge–Ge bonding at $\sim 520\text{ cm}^{-1}$ and $\sim 300\text{ cm}^{-1}$, respectively. Attempts to observe Si–Ge bonding, which should be detected at $\sim 400\text{ cm}^{-1}$, were unsuccessful.

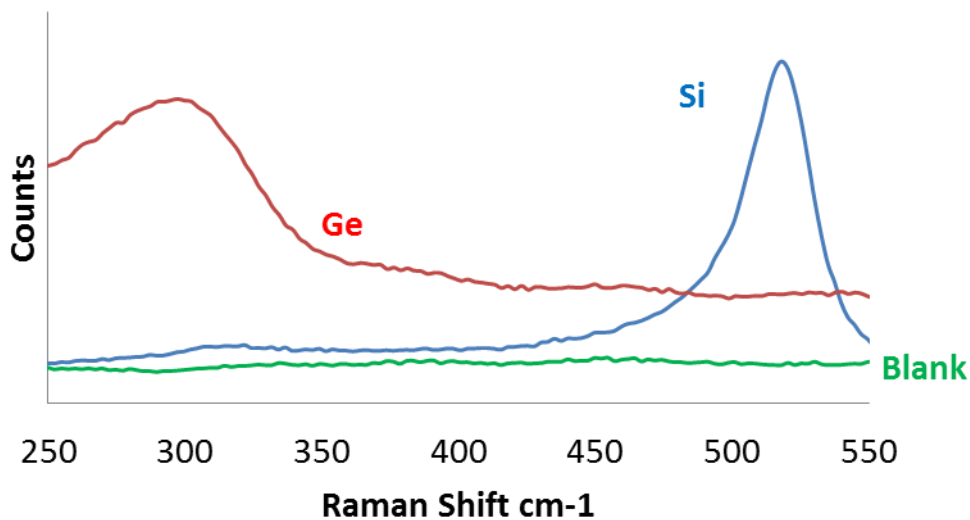


Figure 2.6 Raman spectroscopy for silicon only and germanium only reactions.

The functionalization of silicon and germanium nanomaterials synthesized at high temperatures is challenging, due to the instability of common surface functionalities such as halides and hydrides under these conditions, as well as the unsuitable temperatures, which eliminate the possibility of using anything other than long chain, high boiling point compounds. Other high temperature syntheses have employed an intermediate HF etching step to clean and prepare products for alkylation after the initial synthesis. However, attempting such etching with these products did not yield any isolable products, most likely due to complete etching away of the products, even for minimal etching times. Our attempts to induce alkylation via thermal hydrosilylation/hydrogermylation through the introduction of octadecene both during and after nanocrystal formation were unsuccessful. Infrared spectroscopy of the products (Figure 2.7) obtained were consistent with alkoxy-terminated surfaces, most likely the result of methanol used during post-synthetic rinsing step. The broad -OH stretch at 3400 cm^{-1} and triplet of peaks from $\sim 1330\text{-}1675\text{ cm}^{-1}$ are consistent with a methoxide surface. In addition, there is some evidence of alkyl stretches around 2900 cm^{-1} .

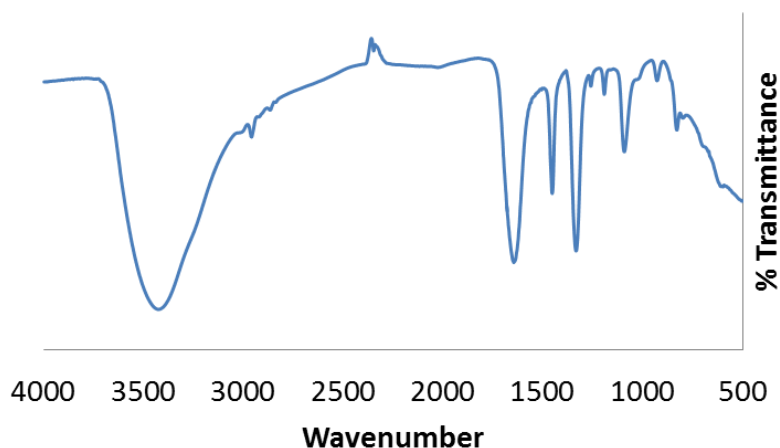


Figure 2.7 Infrared spectroscopy of nanocrystals synthesized in squalane.

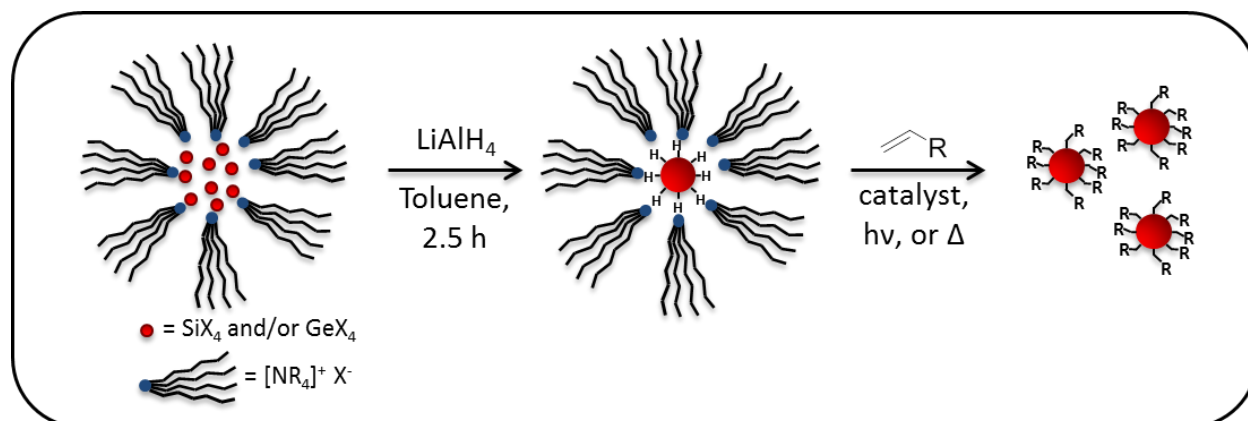
Although we were able to successfully demonstrate the ability to reduce both silicon and germanium tetrahalides at high temperatures to produce nanoscale crystalline products, ultimately, the inability to functionalize the products or purify the products away from undesirable byproducts limited the usefulness of this synthetic approach.

Investigations of Silicon–Germanium Nanocrystal Synthesis Under Room Temperature Conditions

The second paradigm for the production of Group IV nanocrystals is through the use of strong reducing agents at room temperature. In contrast to high temperature syntheses, where conditions limit the types of surface ligands that can be used to functionalize the final particles to higher boiling point (i.e. longer chain) species, room temperature reactions have the potential to be compatible with a wider set of surface ligands, including smaller ligands that are too volatile to employ in high temperature synthesis. The size of these surface ligands can have a profound impact on the electrical behavior of devices created from nanocrystalline films, as close, tight packing of the individual particles is necessary for effective charge transport.^{13,57}

Since both silicon and germanium nanocrystals have been successfully synthesized through a number of different room temperature routes and produced comparable products, we believed that utilizing a mixture of precursors under identical conditions should yield alloyed products. For our investigations, we chose to utilize a synthesis employing hydride reducing agents in conjunction with quaternary ammonium salts as a surfactant to help stabilize the particles and prevent aggregation, as shown in Scheme 2.5. The approach is similar in concept to the well-known Brust-Schiffrin synthetic scheme for producing colloidal gold nanoparticles; the quaternary ammonium salt forms micelles in the reaction solvent. The greater polarity of the core

of the micelle leads to migration of the silicon and germanium tetrahalide precursors into the center. Subsequent addition of the hydride reagent leads to reduction of the tetrahalide precursors within the micelles, generating hydride-terminated nanocrystals.



Scheme 2.5 Surfactant-mediated room temperature synthesis of Group IV nanocrystals.

Our initial experiments with this synthesis utilized lithium aluminum hydride as the reductant, silicon and germanium tetrachloride as the precursor materials, and tetra-n-octylammonium bromide as the surfactant. To investigate the flexibility of the system across the entire continuum of elemental ratios, we focused on five different targets: 100% silicon, 3:1 Si:Ge, 1:1 Si:Ge, 1:3 Si:Ge, and 100% germanium.

The parameters of our initial synthetic attempts were derived from the work of the Tilley and coworkers, who have reported the production of both silicon and germanium nanocrystals from this method. Initial concerns about the extremely high surfactant concentration of 15 mg/ml they reported proved to be valid, as in our hands, the products produced were impossible to separate from the surfactant when following the reported workup procedures. In order to alleviate this, we decided to examine the effect of surfactant concentration by establishing a minimum concentration that would still produce freestanding particles when applied to the

synthesis of silicon nanocrystals. To our great surprise, we found that freestanding nanocrystals were obtained when decreasing the surfactant loading to 10% and 5% of established values. Furthermore, isolable products were produced even when the surfactant was omitted entirely (Figure 2.8). When the same conditions were applied to germanium, however, visible aggregation occurred when the surfactant was omitted. In contrast, freestanding particles were still isolable at 5% and 10% surfactant loading, relative to reported literature precedent.

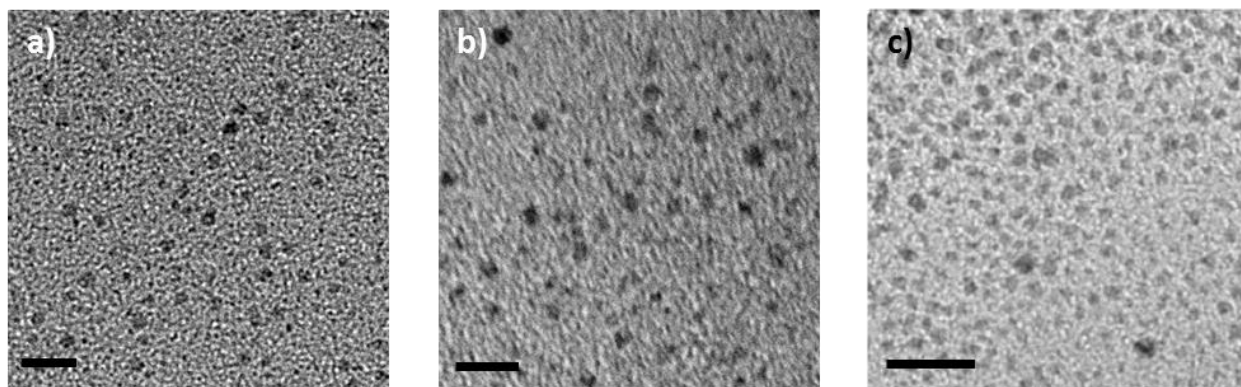


Figure 2.8 Products of SiCl_4 reduction using LiAlH_4 with TOAB concentrations of a) 1.5 mg/mL, b) 0.75 mg/mL, and c) no surfactant. Scalebars are 10 nm.

In order to avoid issues of aggregation when including germanium, we decided to adopt a surfactant loading of 1.5 mg/ml (10% relative to initial experiments). Using these conditions, we were able to produce and isolate colloidally stable products for our five ratios of interest, which are shown in Figures 2.9 and 2.10. The particle sizes remained relatively constant at approximately 3.5 nm across all silicon:germanium ratios.

In all cases, the crystallinity of the products obtained was confirmed through selected area electron diffraction (SAED) and the observation of lattice fringes using high-resolution transmission electron microscopy (HRTEM). The diffraction patterns for the pure silicon and

germanium samples were successfully indexed to their respective elements (Table 2.1). In the patterns that were obtained, a signal that matches the (200) plane is clearly evident in all samples. For the diamond cubic crystal structure, this plane should correspond to a systematic absence and not be observed. Instances of the (200) plane appearing in diffraction patterns for both silicon and germanium nanomaterials exist, although a definitive explanation for its appearance has not been ventured.⁹¹ Double diffraction, arising from multiple scattering events of a single diffracted electron, is an often cited phenomenon for the observation of forbidden diffraction spots.

Ring	Si	Ge	Plane
1 st	3.1 Ang.	3.3 Ang.	(111)
2 nd	2.6 Ang.	2.8 Ang.	(200)
3 rd	1.9 Ang.	2.0 Ang.	(220)
4 th	1.6 Ang.	1.7 Ang.	(311)

Table 2.1 Indexing of selected area electron diffraction rings observed in TEM for Si and Ge only samples

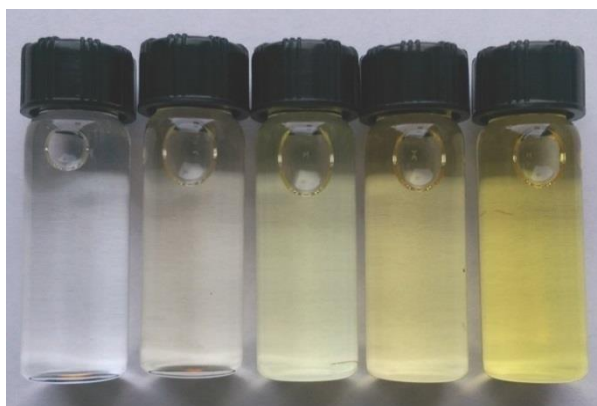


Figure 2.9 Hexane solutions of isolated nanocrystal products. Left to right: Si only, 3:1 Si:Ge, 1:1 Si:Ge, 1:3 Si:Ge, and Ge only.

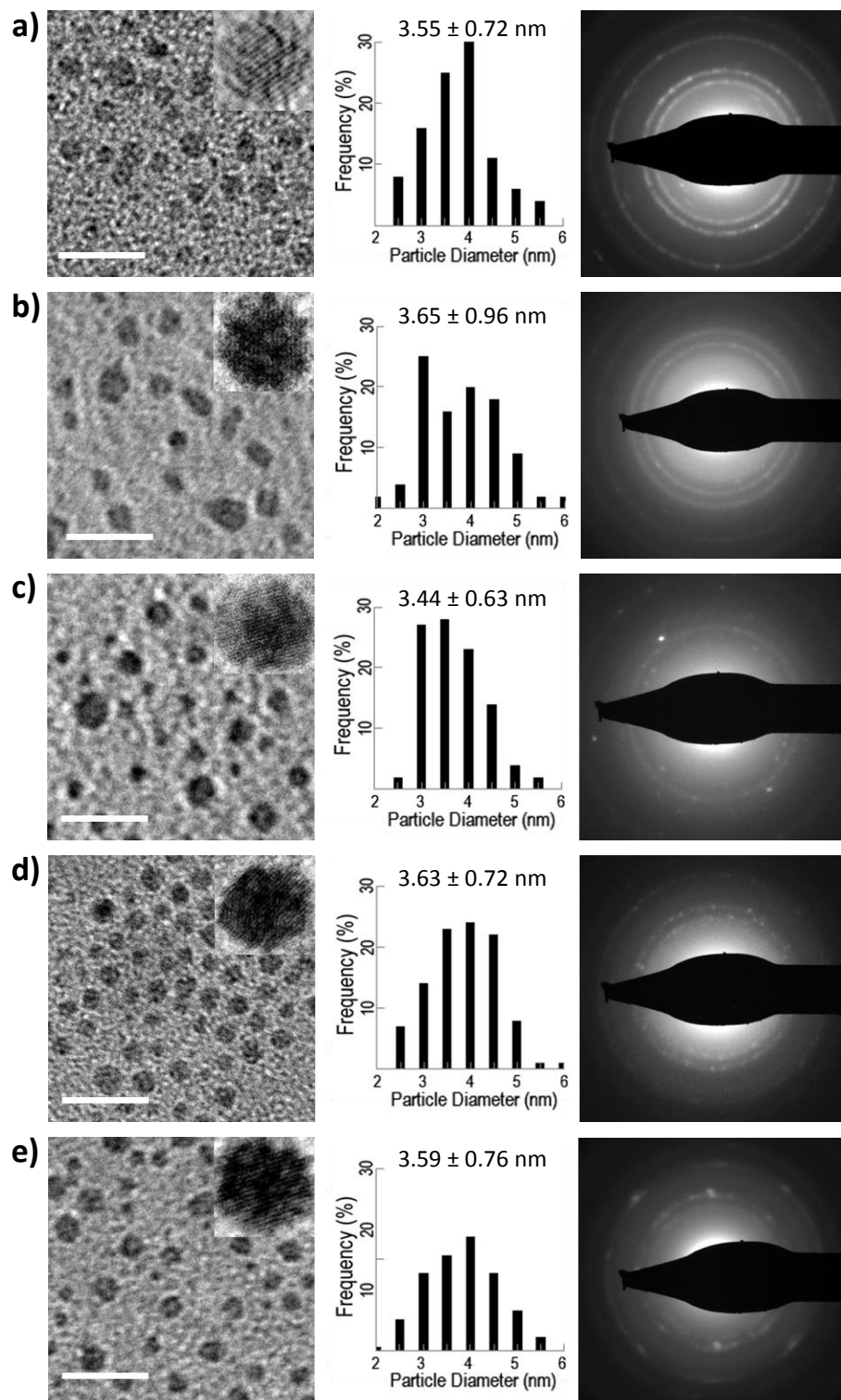


Figure 2.10 TEM images (10 nm scalebars), histograms, and selected area electron diffraction patterns for a) Si only, b) 3:1 Si:Ge, c) 1:1 Si:Ge, d) 1:3 Si:Ge, and e) Ge only reactions.

Normalizing the behavior of the silicon and germanium precursors such that they behave analogously under the reaction conditions is crucial to producing alloyed products where elemental incorporation is relatively even and tracks with changes in precursor ratios. In this synthetic approach, that is accomplished through the use of lithium aluminum hydride, which rapidly reduces both the silicon and germanium precursors. Elemental analysis of TEM samples of each of the products is shown in Figure 2.11. The data displayed represents the average of data collected from four different areas of the TEM grid, and agrees well with planned experimental ratios, suggesting that at a bulk level analysis, both silicon and germanium are being evenly incorporated into the final products. This is important to note, as previous reports utilizing hydride reducing agents with tetrahalide precursors have indicated that silane and germane, both volatile gases, are observed byproducts, and the preferential loss of one over the other would skew the final product composition. The results of this ensemble analysis demonstrate compositional control across the entire range of elemental composition, a feat which, to date, has only been accomplished using laser pyrolysis and nonthermal plasmas, and never before been demonstrated from a solution based synthesis.

Raman microscopy confirms that alloying of both elements is present in the products, rather than production of separate subpopulations of Si and Ge only particles. For the silicon and germanium only syntheses, only the expected Si–Si and Ge–Ge shifts are observed at approximately 500 cm^{-1} and 280 cm^{-1} respectively.^{92,93} The exact peak positions are slightly red shifted in comparison to bulk, which is consistent with previously reported observations in other Si and Ge nanoparticle systems and has been attributed to quantum confinement of phonons.⁹⁴ For the 3:1 and 1:3 Si:Ge syntheses, the dominant bonding modes observed are still Si–Si and

Ge–Ge, respectively, however, a new signal corresponding to Si–Ge bonds is observed around 390 cm^{-1} , which also becomes the dominant signal in the 1:1 Si:Ge sample.⁹⁵

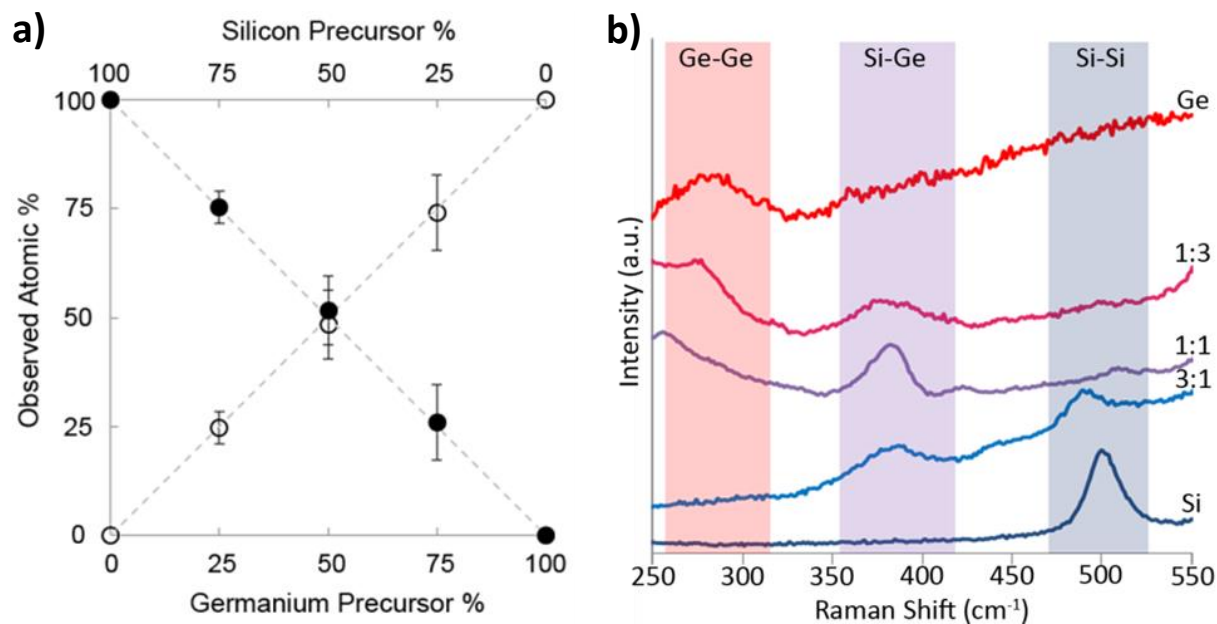


Figure 2.11 a) Ensemble elemental analysis and b) Raman spectra of SiGe reactions at various ratios.

Previous reports utilizing this “inverse micelle” synthetic approach have investigated the effect of different surfactants as well as different reducing agents as methods for controlling the size of particles produced from this reaction.^{41,43} However, even when manipulating these parameters, the sizes accessible through this reaction have still generally been limited to a narrow range of roughly 1-5 nm, except in rare instances where much larger particles >20 nm have been produced. We next investigated what effect our reduced surfactant concentration might have in conjunction with reductants of different strength. To accomplish this we examined the use of six different reductants for the reduction of silicon tetrachloride- lithium aluminum hydride, lithium triethylborohydride (SuperHydride), sodium borohydride, lithium tri-*sec*-butylborohydride, sodium cyanoborohydride, and sodium triacetoxyborohydride. The results are

shown in Figure 2.12. Similar to other reports, we observed the following trend of particle size from smallest to largest: lithium aluminum hydride < lithium triethylborohydride < sodium borohydride < lithium tri-*sec*-butylborohydride. However, the size range that was obtained from these reductants was smaller than was reported for those systems utilizing a larger amount of surfactant.⁴³ This suggests that the surfactant may impact the kinetics of the reduction and/or growth process of the particles during the synthesis. The discrepancy in product size between the use of the triethyl- and tri-*sec*-butyl- borohydrides was also interesting, as their reducing power should be nominally equivalent, owing to the similar electron donating power of the ethyl and *sec*-butyl groups. The difference in particle sizes obtain from these reductants could indicate that an interaction between the surfaces of the growing particles and the Lewis acidic byproducts of the expended reducing agents should not be discounted, as the steric differences of the residual alkylboranes might account for why larger particles are obtained from the more sterically bulky *sec*-butylborohydride.

Neither sodium cyanoborohydride nor sodium triacetoxyborohydride were capable of reducing silicon tetrachloride to produce particle products. However, the use of silicon tetraiodide did lead to isolable particles, shown in Figure 2.13. While the cyanoborohydride produced freestanding particles, the triacetoxyborohydride only yielded large aggregates.

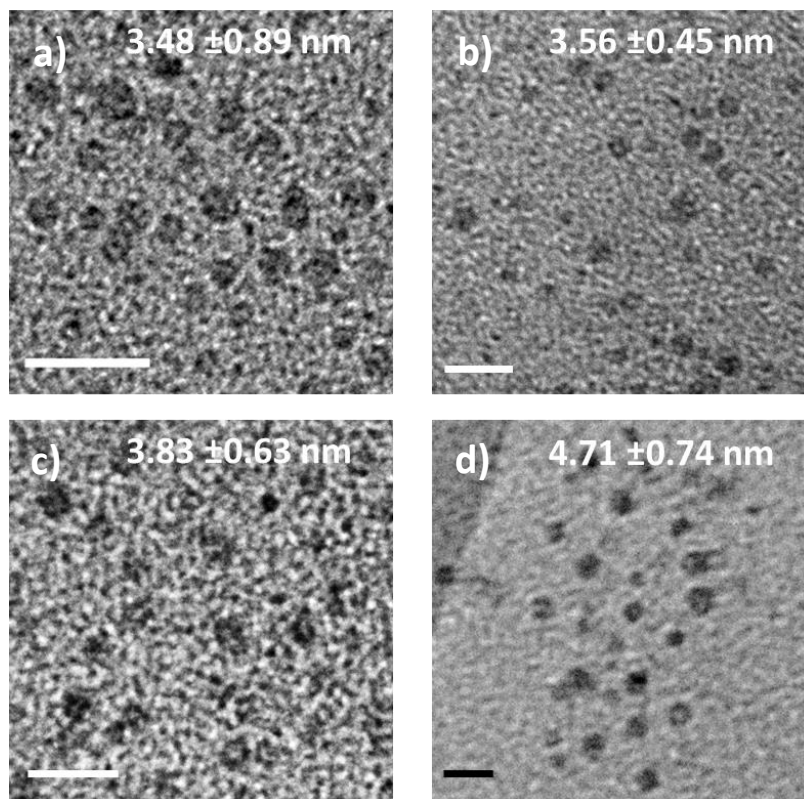


Figure 2.12 Results from reductant screen. a) Lithium aluminum hydride, b) lithium triethylborohydride, c) sodium borohydride, d) lithium tri-*sec*-butylborohydride. Scale bars are 10 nm.

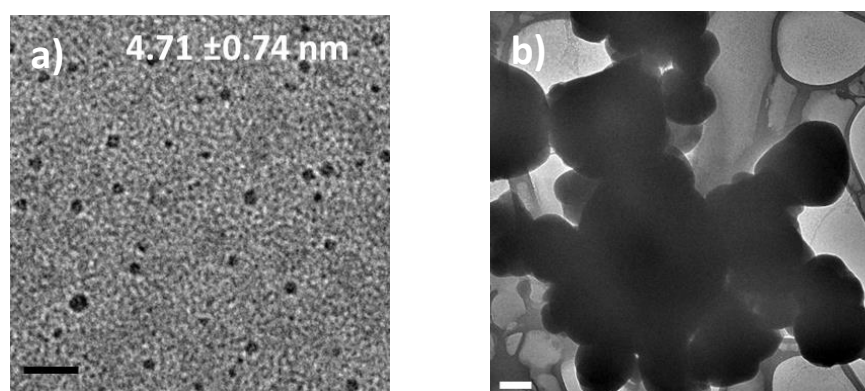
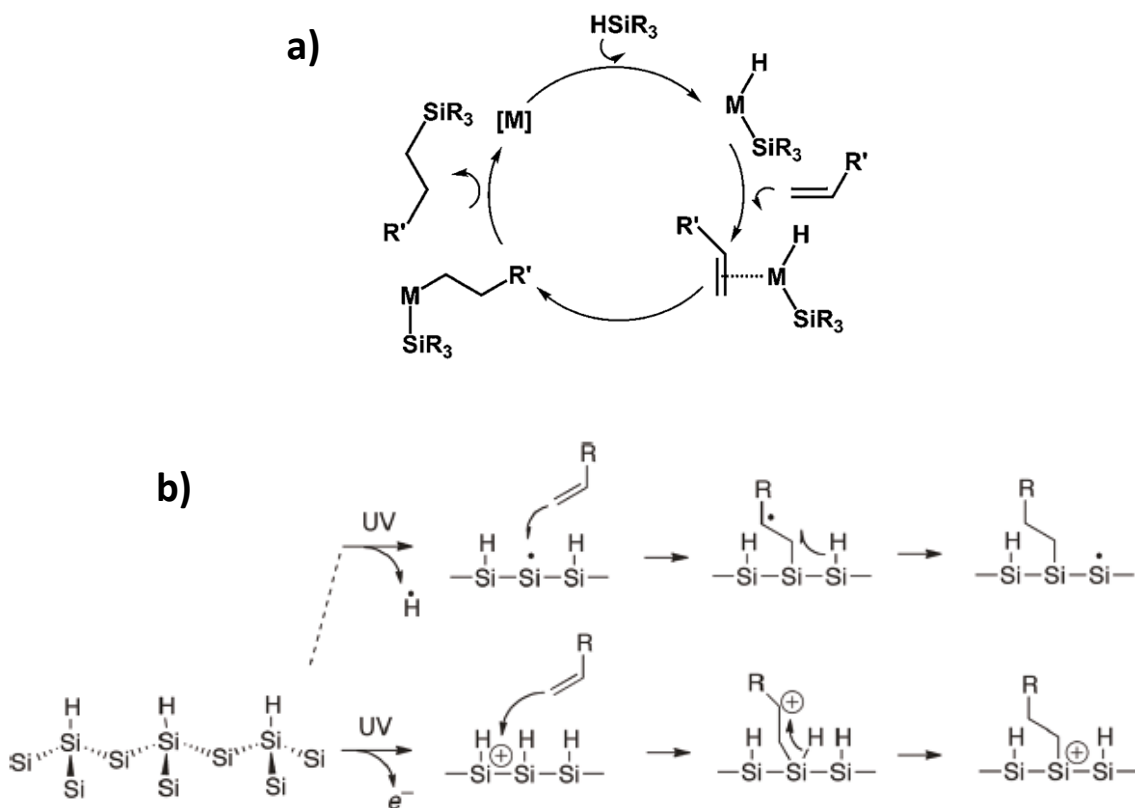


Figure 2.13 Products of SiI_4 reduction with a) sodium cyanoborohydride (20 nm scalebar) and b) sodium triacetoxyborohydride (200 nm scalebar).

In this synthetic approach, the use of a hydride reducing agent results in nanocrystals bearing hydride terminated surfaces. These surfaces render the nanocrystals susceptible to oxidation, and insoluble in all solvents. Hydride surfaces are a common intermediate across a variety of synthetic approaches for both silicon and germanium, and are generally accessed through hydrofluoric acid etching of crude products. Under the conditions utilized to produce these $\text{Si}_x\text{Ge}_{1-x}$ nanocrystals, only two surface functionalization methods have been successfully reported: platinum catalyzed alkylation through the use of Speier's catalyst, and UV-mediated alkylation. Both methods result in the formation of new carbon bonds to the surface from either alkene or alkyne precursors. Platinum catalyzed hydrosilylation is believed to occur through the Chalk-Harrod mechanism, outlined in Scheme 2.6a, in which oxidative addition of the silicon (or germanium) hydride bond to the platinum catalyst is followed by migratory insertion of the hydride into the alkene (or alkyne). Reductive elimination releases the alkylated product and regenerates the platinum catalyst. UV-mediated functionalizations, in contrast, are not as well understood, and a number of mechanisms have been proposed, involving excited surface species such as exciton or free radical generation (Scheme 2.6b).



Scheme 2.6 Proposed mechanisms for a) Pt catalyzed and b) UV-mediated hydrosilylation/hydrogermylation.

Initially, we utilized the platinum catalyzed approach for functionalization of our products, using hexene as our surface ligand (Scheme 2.6a). Unfortunately, following the reported procedures for this method produced inconsistent results, but when successful, did result in colloiddally stable solutions of nanocrystals. The IR spectra for the various products are shown in Figure 2.14. Alkylation of the surfaces is evident through the presence of characteristic C–H stretching modes located from 2800-3000 cm^{-1} . The peaks observed from 1260-1460 cm^{-1} are consistent with the scissoring and bending modes associated with Si–C and Ge–C bonds. Unfortunately, broad stretches between 1000-1100 cm^{-1} are also regularly observed, and are consistent with the peaks corresponding to surface oxidation.

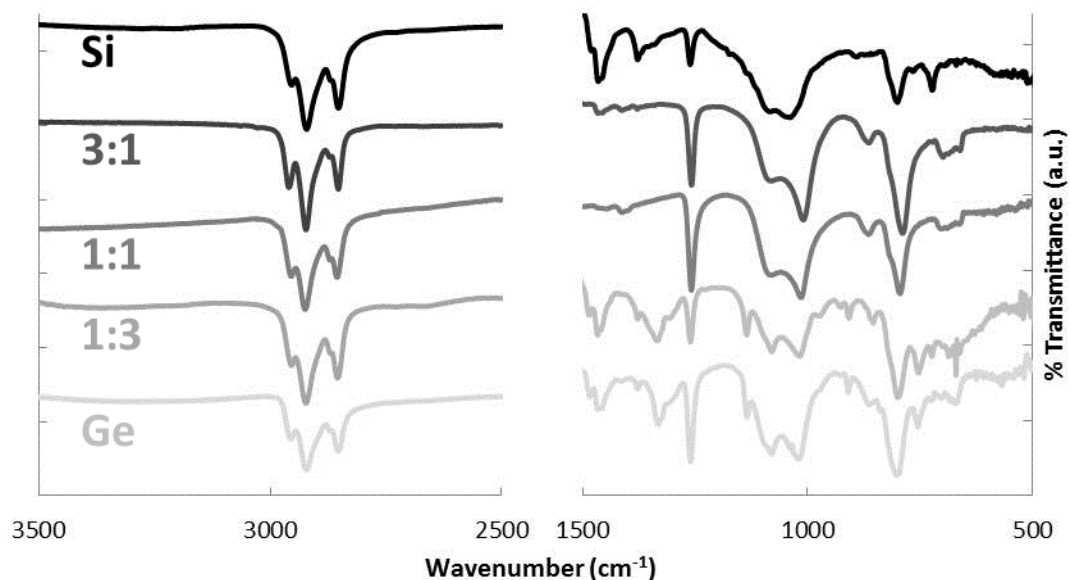


Figure 2.14 IR spectra for nanocrystal products from various ratios of Si and Ge.

The presence of oxidation in spite of maintaining rigorously air and moisture free conditions from start to finish suggests incomplete functionalization of the nanocrystal surfaces, which may arise from a number of sources. Increasing steric crowding at the particle surface as successive alkylations occur may hinder complete passivation, leaving unpassivated surface atoms that oxidize upon exposure to atmospheric conditions. This crowding could also be a result of coordinated surfactant molecules performing a similar role. Furthermore, the nature of the platinum catalyzed functionalization may also be to blame. The formation of colloidal platinum in the hydrosilylation of molecular silanes is known to occur, but of little consequence, as the colloidal platinum still catalyzes the reaction. However, in our systems, colloidal platinum species could lead to reduced efficiency of the surface functionalization, or deposition of platinum onto the nanocrystals themselves, as has been reported for other transition metal catalyzed hydrosilylation of silicon surfaces. Additionally, a number of non-productive side reactions are known to occur with transition metal catalysts, such as hydrogenation, olefin

isomerization, and hydride redistribution.⁷⁵ All of these could interfere with the desired alkylation of the nanocrystal surfaces. To avoid these issues, later functionalization reactions were performed using an ultraviolet light mediated approach (Scheme 2.6b) to facilitate alkylation.

The optoelectronic properties of the hexyl-capped alloy nanocrystals are shown in Figure 2.15. A continual decrease in band gap size is observed with increasing germanium content, demonstrated through the gradual red shifting in absorbance onset. The blue shift in absorbance onset relative to bulk values for the pure elements (0.67 eV for Ge and 1.1 eV for Si) is consistent with electronic confinement and in good agreement with previous reports for solution syntheses of silicon and germanium nanocrystals. At an average diameter of 3.5 nm and with increasing Ge content, one would expect opposing effects of increasing electronic confinement, due to the larger Bohr exciton radius of Ge, and decreasing band gap, due to the narrower band gap of Ge. Our data suggest the latter effect is dominant in determining the absorption properties of alloy $\text{Si}_x\text{Ge}_{1-x}$ nanocrystal solutions, resulting in a bulk-like trend of decreasing band edge absorption onset energy with increasing Ge content. These data also demonstrate the ability to finely control the optoelectronic properties by compositional control of solution-grown $\text{Si}_x\text{Ge}_{1-x}$ nanocrystals.

The emission properties of the various nanocrystals were also examined. The results of these investigations are also shown in Figure 2.11. Several different excitation wavelengths were utilized, ranging from 300-400 nm. The resulting emission curves are consistent across the entire series of nanocrystal compositions, with the greatest emission intensity occurring from excitation using 320-340 nm excitation light, resulting in an emission maximum of approximately 385 nm. This insensitivity in emission characteristics has been previously observed for alloyed $\text{Si}_x\text{Ge}_{1-x}$

nanocrystals produced via a nonthermal plasma. Specifically, the particles that were passivated through subsequent hydrosilylation/hydrogermylation to produce alkylated surfaces were all observed to possess nearly identical emission maxima. Other reports on the luminescence properties of silicon and germanium nanocrystals produced through similar solution routes have displayed results similar to ours.^{40,41,43} Previous reports have suggested that below a specific size threshold of approximately 5 nm, the band structure of germanium shifts such that the lowest conduction band state changes in character from an *L*-derived state to an *X*-derived state, leading to silicon-like behavior, which may account for the lack of any change in emission properties.⁹⁶

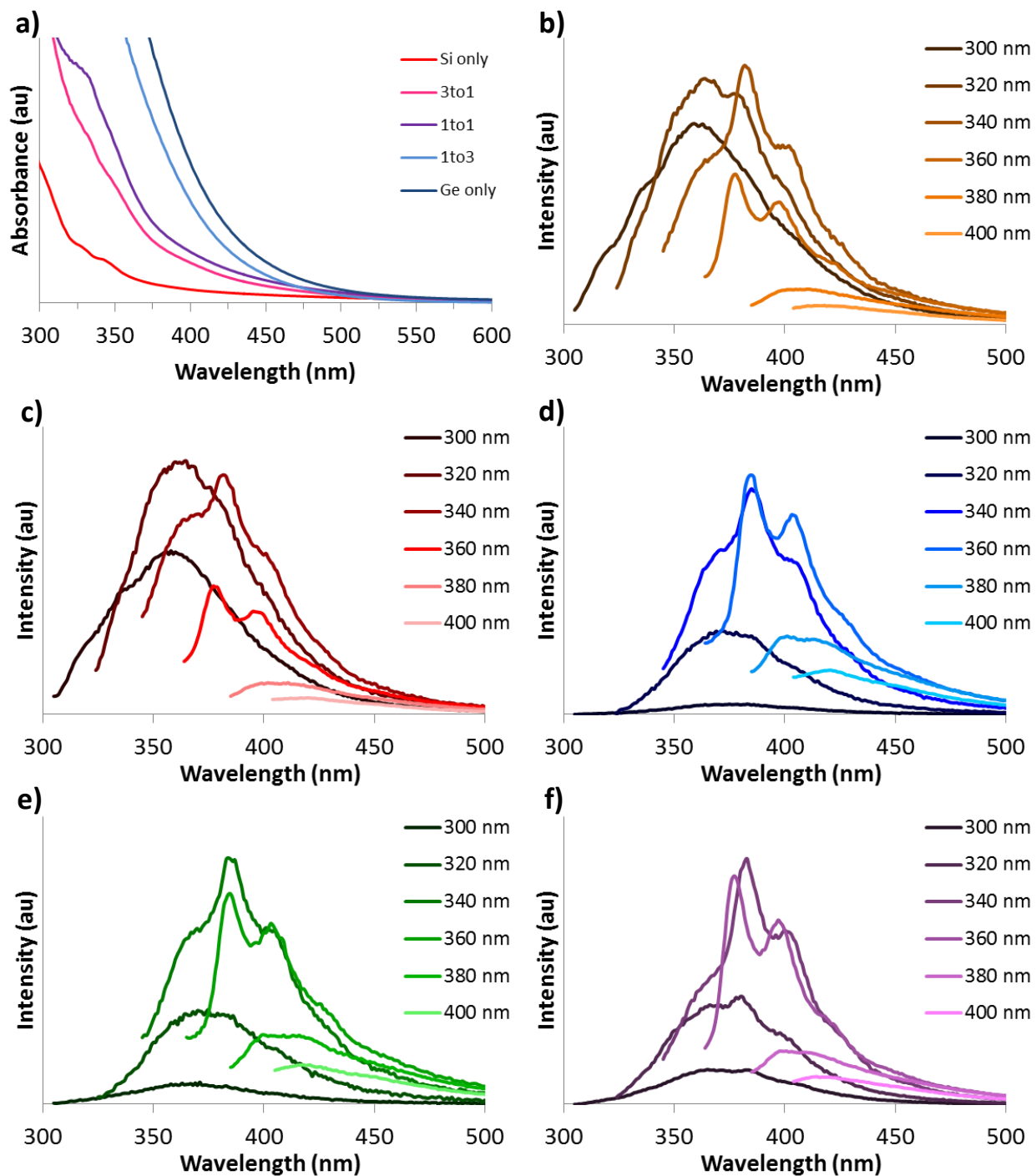


Figure 2.15 a) UV-Vis absorbance and emission profiles for b) Si, c) 3:1 Si:Ge, d) 1:1 Si:Ge, e) 1:3 Si:Ge, and f) Ge nanocrystals.

2.8 Conclusions and Future Work

The results presented here demonstrate the successful production of alloyed $\text{Si}_x\text{Ge}_{1-x}$ nanocrystals through adaptation of an existing room temperature solution-phase approach. The use of a strong reducing agent serves as a method for normalizing the different reactivity of silicon and germanium halides, resulting in smooth incorporation of both elements into the particles produced from the reaction. The utility of this synthetic approach could be further improved in several ways-

Modification of reaction parameters to produce a larger range of particle sizes would be a useful extension of this methodology by expanding the range of accessible optoelectronic properties. This would allow for additional tuning of these materials to desired specifications. In addition, small silicon nanocrystals have been demonstrated to have a lower thermopower due to increased coupling between charge carriers and phonons, making size control critical for any intended thermoelectric use.¹²

Introducing dopant atoms into semiconductors is a well-established technique for improving their electrical properties, specifically with regards to carrier concentration. For these nanocrystals to be used in electronic devices, having access to the ability to produce n- and p-type products would be extremely beneficial for improving performance. A recent report has demonstrated that this method is amenable for incorporating metal dopants, suggesting that it may serve as a viable basis for other non-metal elements as well.⁹⁷

Surface chemistry is another crucial aspect to producing stable, soluble, electrically conductive products. Currently, there are a very limited number of demonstrated surface functionalization routes. Unfortunately, the use of the strong reductants utilized here limits

options in this regard, unless quenching is performed prior to functionalization, which can be problematic in preserving the hydride surface of the particles.⁹⁸ Addressing this issue is extremely important to producing products that are useful as functional materials, rather than just academic novelties.

2.9 Experimental Procedures

High temperature SiGe procedure

In a glovebox, a total of 0.6 mmol of silicon and/or germanium precursors (MX₄ X = Cl, Br, I) were added to 5 ml of dry, degassed squalane in an oven-dried three neck round bottom flask. A water condenser was attached, the apparatus was sealed and the setup was transferred to a Schlenk line and placed under flowing N₂. The reaction was heated to 250 °C at a rate of 10 °C/min. At this point, a solution of 2 equiv. of *n*-butyllithium was prepared in 1 mL of squalane. This solution was added to the reaction, resulting in a color change to a brown solution. The reaction was heated to 300 °C and then cooled to room temperature.

The solution was transferred to a centrifuge tube using 5 mL of toluene, and the products were precipitated through the addition of methanol and isolated through centrifugation at 10,000 g for 5 minutes. The products were resuspended in toluene and precipitated two additional times to remove salt byproducts. The final products were stored as brown solids in a glovebox.

Room temperature SiGe procedure

In a glovebox, a total of 0.87 mmol of silicon and/or germanium precursors (generally the tetrachloride) were added to 50 mL of anhydrous toluene in an oven dried round bottom flask. 0.247 mmol of tetra-*n*-octylammonium bromide were added to the flask and the solution was

allowed to stir for 30 minutes. To induce reduction, a solution of 2.0 equiv. of the desired reductant were then added dropwise, and the reaction was left to stir for 2 hours.

Platinum catalyzed hydrosilylation

After 2 hours, the excess reductant was quenched through addition of 20 mL of anhydrous alcohol (either methanol or isopropanol). Separately, 150 μ L of a 0.1 M solution of chloroplatinic acid hexahydrate in anhydrous isopropanol was prepared and added to the reaction with 3 mL of dry, degassed 1-hexene. The reaction was stirred overnight at room temperature.

UV-mediated hydrosilylation

After 2 hours, 3 mL of 1-hexene was added to the reaction, and the solution was transferred to a quartz reaction tube, which was then sealed. The tube was removed from the glovebox and transferred to a UV-light chamber, where it was irradiated with UV light overnight.

Purification

Following established protocols, the crude solutions were evaporated on a rotary evaporator to yield a viscous oil and colorless solid. 50 mL of hexane were added and the solution was sonicated. 50 mL of *N*-methylformamide were added to extract salts and residual surfactant, while the products remained in the hexane layer. This washing step was repeated a total of three times, after which the hexane layer was evaporated by rotary evaporation to yield UV-luminescent oils. These products were dried under vacuum overnight and stored as neat oils.

2.10 References

- (1) Zhu, Z.; Xiao, J.; Sun, H.; Hu, Y.; Cao, R.; Wang, Y.; Zhao, L.; Zhuang, J. *Phys. Chem. Chem. Phys.* **2015**, *17*, 21605-21610.
- (2) Yi, S.-i.; Yu, C. *J. Appl. Phys.* **2015**, *117*, 035105.
- (3) Pulikkotil, J. J.; Auluck, S. *AIP Advances* **2015**, *5*, 037145.
- (4) Pethuraja, G. G.; Welser, R. E.; Sood, A. K.; Lee, C.; Alexander, N. J.; Efstathiadis, H.; Haldar, P.; Harvey, J. L. *Materials Sciences and Applications* **2012**, *03*, 67-71.
- (5) Yu, B.; Zebarjadi, M.; Wang, H.; Lukas, K.; Wang, H.; Wang, D.; Opeil, C.; Dresselhaus, M.; Chen, G.; Ren, Z. *Nano Lett.* **2012**, *12*, 2077-2082.
- (6) Wang, X. W.; Lee, H.; Lan, Y. C.; Zhu, G. H.; Joshi, G.; Wang, D. Z.; Yang, J.; Muto, A. J.; Tang, M. Y.; Klatsky, J.; Song, S.; Dresselhaus, M. S.; Chen, G.; Ren, Z. *F. Appl. Phys. Lett.* **2008**, *93*, 193121.
- (7) Joshi, G.; Lee, H.; Lan, Y.; Wang, X.; Zhu, G.; Wang, D.; Gould, R. W.; Cuff, D. C.; Tang, M. Y.; Dresselhaus, M. S.; Chen, G.; Ren, Z. *Nano Lett.* **2008**, *8*, 4670-4674.
- (8) *Handbook series on semiconductor parameters 1. 1*; World Scientific: Singapore [u.a.], 2000.
- (9) Canham, L. T. *Appl. Phys. Lett.* **1990**, *57*, 1046.
- (10) Dasog, M.; De los Reyes, G. B.; Titova, L. V.; Hegmann, F. A.; Veinot, J. G. C. *ACS Nano* **2014**, *8*, 9636-9648.
- (11) Ghosh, B.; Shirahata, N. *Sci. Technol. Adv. Mat.* **2014**, *15*, 014207.
- (12) Singh, V.; Yu, Y.; Sun, Q. C.; Korgel, B.; Nagpal, P. *Nanoscale* **2014**, *6*, 14643-14647.
- (13) Ruddy, D. A.; Johnson, J. C.; Smith, E. R.; Neale, N. R. *ACS Nano* **2010**, *4*, 7459-7466.
- (14) Mangolini, L. *J. Vac. Sci. Technol. B* **2013**, *31*, 020801.

- (15) Švrček, V.; Rehspringer, J. L.; Gaffet, E.; Slaoui, A.; Muller, J. C. *J. Cryst. Growth* **2005**, *275*, 589-597.
- (16) Araujo-Andrade, C. *Scripta Mater.* **2003**, *49*, 773-778.
- (17) Lam, C.; Zhang, Y. F.; Tang, Y. H.; Lee, C. S.; Bello, I.; Lee, S. T. *J. Cryst. Growth* **2000**, *220*, 466-470.
- (18) Snedaker, M. L.; Zhang, Y.; Birkel, C. S.; Wang, H.; Day, T.; Shi, Y.; Ji, X.; Kraemer, S.; Mills, C. E.; Moosazadeh, A.; Moskovits, M.; Snyder, G. J.; Stucky, G. D. *Chem. Mater.* **2013**, *25*, 4867-4873.
- (19) Shen, T. D.; Koch, C. C.; McCormick, T. L.; Nemanich, R. J.; Huang, J. Y.; Huang, J. G. *J. Mater. Res.* **1995**, *10*, 139-148.
- (20) Shen, T. D.; Shmagin, I.; Koch, C. C.; Kolbas, R. M.; Fahmy, Y.; Bergman, L.; Nemanich, R. J.; McClure, M. T.; Sitar, Z.; Quan, M. X. *Phys. Rev. B* **1997**, *55*, 7615-7623.
- (21) Kolasinski, K. W. *Curr. Opin. Solid St. M.* **2005**, *9*, 73-83.
- (22) Choi, J.; Wang, N. S.; Reipa, V. *Langmuir* **2009**, *25*, 7097-7102.
- (23) Yu, Y.; Rowland, C. E.; Schaller, R. D.; Korgel, B. A. *Langmuir* **2015**, *31*, 6886-6893.
- (24) Mastronardi, M. L.; Maier-Flaig, F.; Faulkner, D.; Henderson, E. J.; Kubel, C.; Lemmer, U.; Ozin, G. A. *Nano Lett.* **2012**, *12*, 337-342.
- (25) Hessel, C. M.; Reid, D.; Panthani, M. G.; Rasch, M. R.; Goodfellow, B. W.; Wei, J.; Fujii, H.; Akhavan, V.; Korgel, B. A. *Chem. Mater.* **2012**, *24*, 393-401.
- (26) Wheeler, L. M.; Neale, N. R.; Chen, T.; Kortshagen, U. R. *Nat. Commun.* **2013**, *4*, 2197.
- (27) Pereira, R. N.; Rowe, D. J.; Anthony, R. J.; Kortshagen, U. *Phys. Rev. B* **2012**, *86*.
- (28) Mangolini, L.; Kortshagen, U. *Adv. Mater.* **2007**, *19*, 2513-2519.

- (29) Lacour, F.; Guillois, O.; Portier, X.; Perez, H.; Herlin, N.; Reynaud, C. *Physica E: Low-dimensional Systems and Nanostructures* **2007**, *38*, 11-15.
- (30) Kim, S.; Yi Park, S.; Jeong, J.; Kim, G. H.; Rohani, P.; Suk Kim, D.; Swihart, M. T.; Young Kim, J. *Nanotechnol.* **2015**, *26*, 305703.
- (31) Heath, J. T. *Science* **1992**, *258*, 1131-1133.
- (32) Lee, D. C.; Hanrath, T.; Korgel, B. A. *Angew. Chem. Int. Ed. Engl.* **2005**, *44*, 3573-3577.
- (33) Lu, X.; Korgel, B. A. *Chemistry* **2014**, *20*, 5874-5879.
- (34) Lu, X.; Hessel, C. M.; Yu, Y.; Bogart, T. D.; Korgel, B. A. *Nano Lett.* **2013**, *13*, 3101-3105.
- (35) Tuan, H.-Y.; Lee, D. C.; Hanrath, T.; Korgel, B. A. *Nano Lett.* **2005**, *5*, 681-684.
- (36) Sletnes, M.; Maria, J.; Grande, T.; Lindgren, M.; Einarsrud, M. A. *Dalton Trans.* **2014**, *43*, 2127-2133.
- (37) Atkins, T. M.; Cassidy, M. C.; Lee, M.; Ganguly, S.; Marcus, C. M.; Kauzlarich, S. M. *ACS Nano* **2013**, *7*, 1609-1617.
- (38) Baldwin, R. K.; Pettigrew, K. A.; Ratai, E.; Augustine, M. P.; Kauzlarich, S. M. *Chem. Comm.* **2002**, 1822-1823.
- (39) Tanke, R. S.; Kauzlarich, S. M.; Patten, T. E.; Pettigrew, K. A.; Murphy, D. L.; Thompson, M. E.; Lee, H. W. H. *Chem. Mater.* **2003**, *15*, 1682-1689.
- (40) McVey, B. F.; Tilley, R. D. *Acc Chem Res* **2014**, *47*, 3045-3051.
- (41) Linehan, K.; Doyle, H. *Small* **2014**, *10*, 584-590.
- (42) Wang, J.; Sun, S.; Peng, F.; Cao, L.; Sun, L. *Chem Commun. (Camb)* **2011**, *47*, 4941-4943.
- (43) Carolan, D.; Doyle, H. *J. Nanomater.* **2015**, *2015*, 1-9.

- (44) Carolan, D.; Doyle, H. *J. Mater. Chem. C* **2014**, *2*, 3562-3568.
- (45) Wheeler, L. M.; Levij, L. M.; Kortshagen, U. R. *J. Phys. Chem. Lett.* **2013**, *4*, 3392-3396.
- (46) Prabakar, S.; Shiohara, A.; Hanada, S.; Fujioka, K.; Yamamoto, K.; Tilley, R. D. *Chem. Mater.* **2010**, *22*, 482-486.
- (47) Ma, X.; Wu, F.; Kauzlarich, S. M. *J. Solid State Chem.* **2008**, *181*, 1628-1633.
- (48) Chiu, H. W.; Kauzlarich, S. M. *Chem. Mater.* **2006**, *18*, 1023-1028.
- (49) Holman, Z. C.; Kortshagen, U. R. *Langmuir* **2009**, *25*, 11883-11889.
- (50) Gresback, R.; Holman, Z.; Kortshagen, U. *Appl. Phys. Lett.* **2007**, *91*, 093119.
- (51) Lu, X.; Korgel, B. A.; Johnston, K. P. *Chem. Mater.* **2005**, *17*, 6479-6485.
- (52) Vaughn, D. D.; Bondi, J. F.; Schaak, R. E. *Chem. Mater.* **2010**, *22*, 6103-6108.
- (53) Muthuswamy, E.; Zhao, J.; Tabatabaei, K.; Amador, M. M.; Holmes, M. A.; Osterloh, F. E.; Kauzlarich, S. M. *Chem. Mater.* **2014**, *26*, 2138-2146.
- (54) Vaughn, D. D., 2nd; Schaak, R. E. *Chem. Soc. Rev.* **2013**, *42*, 2861-2879.
- (55) Muthuswamy, E.; Iskandar, A. S.; Amador, M. M.; Kauzlarich, S. M. *Chem. Mater.* **2013**, *25*, 1416-1422.
- (56) Xue, D. J.; Wang, J. J.; Wang, Y. Q.; Xin, S.; Guo, Y. G.; Wan, L. J. *Adv. Mater.* **2011**, *23*, 3704-3707.
- (57) Ruddy, D. A.; Erslev, P. T.; Habas, S. E.; Seabold, J. A.; Neale, N. R. *J. Phys. Chem. Lett.* **2013**, *4*, 416-421.
- (58) Zebarjadi, M.; Joshi, G.; Zhu, G.; Yu, B.; Minnich, A.; Lan, Y.; Wang, X.; Dresselhaus, M.; Ren, Z.; Chen, G. *Nano Lett.* **2011**, *11*, 2225-2230.
- (59) Barry, S. D.; Yang, Z.; Kelly, J. A.; Henderson, E. J.; Veinot, J. G. C. *Chem. Mater.* **2011**, *23*, 5096-5103.

- (60) Kanno, T.; Fujii, M.; Sugimoto, H.; Imakita, K. *J. Mat. Chem. C* **2014**, *2*, 5644.
- (61) Stoib, B.; Langmann, T.; Matich, S.; Antesberger, T.; Stein, N.; Angst, S.; Petermann, N.; Schmechel, R.; Schierning, G.; Wolf, D. E.; Wiggers, H.; Stutzmann, M.; Brandt, M. S. *Appl. Phys. Lett.* **2012**, *100*, 231907.
- (62) Erogbogbo, F.; Liu, T.; Ramadurai, N.; Tuccarione, P.; Lai, L.; Swihart, M. T.; Prasad, P. N. *ACS Nano* **2011**, *5*, 7950-7959.
- (63) Pi, X. D.; Kortshagen, U. *Nanotechnol.* **2009**, *20*, 295602.
- (64) Lee, E. K.; Yin, L.; Lee, Y.; Lee, J. W.; Lee, S. J.; Lee, J.; Cha, S. N.; Whang, D.; Hwang, G. S.; Hippalgaonkar, K.; Majumdar, A.; Yu, C.; Choi, B. L.; Kim, J. M.; Kim, K. *Nano Lett.* **2012**, *12*, 2918-2923.
- (65) Dohnalova, K.; Gregorkiewicz, T.; Kusova, K. *J. Phys. Condens. Matter* **2014**, *26*, 173201.
- (66) Reboredo, F. A.; Zunger, A. *Phys. Rev. B* **2001**, *63*.
- (67) Lee, D. C.; Pietryga, J. M.; Robel, I.; Werder, D. J.; Schaller, R. D.; Klimov, V. I. *J. Am. Chem. Soc.* **2009**, *131*, 3436-3437.
- (68) Fuzell, J.; Thibert, A.; Atkins, T. M.; Dasog, M.; Busby, E.; Veinot, J. G. C.; Kauzlarich, S. M.; Larsen, D. S. *J. Phys. Chem. Lett.* **2013**, *4*, 3806-3812.
- (69) Dasog, M.; Yang, Z.; Regli, S.; Atkins, T. M.; Faramus, A.; Singh, M. P.; Muthuswamy, E.; Kauzlarich, S. M.; Tilley, R. D.; Veinot, J. G. C. *ACS Nano* **2013**, *7*, 2676-2685.
- (70) Dasog, M.; Veinot, J. G. C. *Phys. Status Solidi A* **2012**, *209*, 1844-1846.
- (71) Atkins, T. M.; Louie, A. Y.; Kauzlarich, S. M. *Nanotechnol.* **2012**, *23*, 294006.
- (72) Webb, L. J.; Lewis, N. S. *J. Phys. Chem. B* **2003**, *107*, 5404-5412.

- (73) Yang, Z.; Iqbal, M.; Dobbie, A. R.; Veinot, J. G. *J. Am. Chem. Soc.* **2013**, *135*, 17595-17601.
- (74) Fok, E.; Shih, M.; Meldrum, A.; Veinot, J. G. *Chem. Commun. (Camb)* **2004**, 386-387.
- (75) Nakajima, Y.; Shimada, S. *RSC Adv.* **2015**, *5*, 20603-20616.
- (76) Roy, A. K.; Taylor, R. B. *J. Am. Chem. Soc.* **2002**, *124*, 9510-9524.
- (77) Sakaki, S.; Mizoe, N.; Sugimoto, M. *Organometallics* **1998**, *17*, 2510-2523.
- (78) Boukherroub, R.; Morin, S.; Bensebaa, F.; Wayner, D. D. M. *Langmuir* **1999**, *15*, 3831-3835.
- (79) Purkait, T. K.; Iqbal, M.; Wahl, M. H.; Gottschling, K.; Gonzalez, C. M.; Islam, M. A.; Veinot, J. G. *J. Am. Chem. Soc.* **2014**, *136*, 17914-17917.
- (80) Buriak, J. M. *Chem. Mater.* **2014**, *26*, 763-772.
- (81) Kelly, J. A.; Shukaliak, A. M.; Fleischauer, M. D.; Veinot, J. G. *J. Am. Chem. Soc.* **2011**, *133*, 9564-9571.
- (82) Kelly, J. A.; Veinot, J. G. *ACS Nano* **2010**, *4*, 4645-4656.
- (83) Holmberg, V. C.; Korgel, B. A. *Chem. Mater.* **2010**, *22*, 3698-3703.
- (84) Holman, Z. C.; Kortshagen, U. R. *Nano Lett.* **2011**, *11*, 2133-2136.
- (85) Wang, R.; Pi, X.; Yang, D. *Phys. Chem. Chem. Phys.* **2013**, *15*, 1815-1820.
- (86) Li, Q.; He, Y.; Chang, J.; Wang, L.; Chen, H.; Tan, Y. W.; Wang, H.; Shao, Z. *J. Am. Chem. Soc.* **2013**, *135*, 14924-14927.
- (87) Levason, W.; Pugh, D.; Reid, G. *Inorg. Chem.* **2013**, *52*, 5185-5193.
- (88) England, J.; Wieghardt, K. *Inorg. Chem.* **2013**, *52*, 10067-10079.
- (89) Levason, W.; Reid, G.; Zhang, W. *Coord. Chem. Rev.* **2011**, *255*, 1319-1341.
- (90) Passarelli, V.; Carta, G.; Rossetto, G.; Zanella, P. *Dalton Trans.* **2003**, 413-419.

- (91) Perraud, S.; Quesnel, E.; Parola, S.; Barbé, J.; Muffato, V.; Faucherand, P.; Morin, C.; Jarolimek, K.; Van Swaaij, R. A. C. M. M.; Zeman, M.; Richards, S.; Kingsley, A.; Doyle, H.; Linehan, K.; O'Brien, S.; Povey, I. M.; Pemble, M. E.; Xie, L.; Leifer, K.; Makasheva, K.; Despax, B. *Phys. Status Solidi A* **2013**, *210*, 649-657.
- (92) Vadavalli, S.; Valligatla, S.; Neelamraju, B.; Dar, M. H.; Chiasera, A.; Ferrari, M.; Desai, N. R. *Front. Phys.* **2014**, *2*, 1–9.
- (93) Meier, C.; Lüttjohann, S.; Kravets, V. G.; Nienhaus, H.; Lorke, A.; Wiggers, H. *Physica E* **2006**, *32*, 155-158.
- (94) Ren, S. -F.; Cheng, W.; Yu, P. Y. *Phys. Rev. B* **2004**, *69*, 235327.
- (95) Alonso, M. I.; Winer, K. *Phys. Rev. B* **1989**, *39*, 10056-10062.
- (96) Reboredo, F. A.; Zunger, A. *Phys. Rev. B* **2000**, *62*, R2275-R2278.
- (97) McVey, B. F.; Butkus, J.; Halpert, J. E.; Hodgkiss, J. M.; Tilley, R. D. *J. Phys. Chem. Lett.* **2015**, *6*, 1573-1576.
- (98) Dung, M. X.; Jeong, H.-D. *B. Kor. Chem. Soc.* **2012**, *33*, 4185-4187.

Chapter 3: The Synthesis of Metal–Germanide and Metal– Silicide Nanomaterials

3.1 Introduction

Metal silicide and germanide materials have long been known to the electronics industry for their utility as low resistivity contacts and as metal-to-semiconductor interconnects in germanium and silicon-based devices.¹⁻¹⁷ In addition, they can exhibit a number of interesting electronic, optical, magnetic, catalytic, and mechanical properties. These have made them target materials for applications such as thermoelectrics,¹⁸⁻²² spintronics,^{1,9,23} hydrogen evolution reaction (HER) catalysis,^{24,25} CMOS devices,^{7,26-28} MOSFETs,²⁶⁻²⁹ batteries,³⁰ and optoelectric devices,³¹ among others.³²⁻³⁴ However, there is limited knowledge about the properties of these materials at the nanoscale, due to the difficulties associated with their synthesis. The high temperatures often needed to induce silicide and germanide phase formation complicate the already demanding conditions required for pure germanium and silicon nanomaterials synthesis.^{26,27,35,36} Furthermore, the complex phase behavior of many metal germanide and silicide systems makes rational synthetic design of specific phase or phase pure products extremely challenging. However, the phase-dependent nature of the electronic properties of these silicides makes attaining this control as important as producing the silicides themselves.

The development of colloidal syntheses for metal–germanide and silicide nanomaterials would be a valuable addition to current group-IV nanomaterial chemistry. In addition to examining the electronic properties of the materials themselves, these colloidal silicides and germanides are a key component in the production of heterostructured devices for thermoelectric

applications, making development of synthetic protocols an important prerequisite before those goals can be realized. Furthermore, some metal silicides, such as manganese silicide and rhenium silicide are decent thermoelectric materials in their own right, with reported zT values of 0.7 and 0.8 respectively.¹⁰

3.2 Synthetic Approaches for Metal–Silicide Nanomaterials

The production of metal silicide nanomaterials has been dominated principally through vapor phase and solid state reactions, owing to the high temperatures needed to produce silicide phases. Existing reports on metal silicide nanomaterials, excluding thin films, are heavily biased towards the production of nanowires,³⁷ and can be loosely divided into four different reaction approaches; silicidation of silicon nanowires,^{5,10} introduction of silane to a metal surface,^{10,38} introduction of a volatile metal precursor to a silicon surface,^{10,33,39-41} or simultaneous deposition of silicon and metal species.^{10,42-44} Using these various approaches, several phases of several different silicides have been produced from iron (FeSi ,^{39,42} FeSi_2 ,^{33,45} Fe_5Si_3 ,⁴⁶ $\text{Fe}_{1-x}\text{Co}_x\text{Si}$ ^{47,48}), cobalt (CoSi ,^{43,49,50} CoSi_2 ,⁵¹ Co_2Si ,⁵⁰ Co_3Si ,⁵⁰), nickel (NiSi ,^{5,52} Ni_2Si ,⁵³ Ni_3Si ,⁵⁴ $\text{Ni}_{31}\text{Si}_{12}$,⁵⁵ Ni_3Si_2 ,⁵⁶ NiSi_2 ⁵⁷), chromium (CrSi_2),^{41,58,59} platinum (PtSi ,⁴⁰ Pt_6Si_5 ¹⁰), copper ($\text{Cu}_{15}\text{Si}_4$),⁶⁰ titanium (TiSi ,⁴⁴ TiSi_2 ,⁶¹⁻⁶³ Ti_5Si_3 ,⁶⁴ Ti_5Si_4 ⁶⁵), tantalum (TaSi_2),^{6,66} and manganese (MnSi ,¹⁰ Mn_4Si_7 ,⁶⁷ $\text{Mn}_{19}\text{Si}_{33}$).⁶⁸

In comparison, synthetic approaches for producing metal silicide nanocrystals, rather than wires, are almost nonexistent. The first solution phase report of a silicide synthesis was reported in 2010, for the production of iron silicide (Fe_3Si and/or FeSi_2) nanocrystals.⁶⁹ Schaak and coworkers very recently reported a solution phase synthesis of three different metal silicide nanocrystals through a two-step process in which pre-synthesized metal nanoparticles were

silicided via thermal decomposition of phenylsilane at high temperatures in squalane,²⁴ following a similar procedure to those used in the production of silicon and germanium nanowires via solution-liquid-solid methodologies popularized by Korgel and coworkers.⁷⁰

3.3 Synthetic Approaches for Metal–Germanide Nanomaterials

Just as was the case originally with silicon and germanium nanomaterials, metal germanide materials have, by and large, been overshadowed by the popularity of metal silicides. However, as interest in germanium has risen once again, so has interest in the analogous germanide materials. Just as with the previously discussed metal silicides, vapor phase and solid state reactions have been the methods of choice for the production of metal germanides. Germanide nanomaterials based off of iron ($\text{Fe}_{1.3}\text{Ge}$),^{71,72} nickel (Ni_2Ge ,⁷³ NiGe^{12}), cobalt (Co_5Ge_7),^{28,74} and copper (Cu_3Ge)¹¹ have all been successfully produced.

As with the silicides, examples of freestanding metal germanide nanocrystal syntheses are also exceedingly rare. Currently, the only example of metal germanide nanocrystals is from Schaak and coworkers, who recently reported the synthesis of iron germanide nanocrystals using an amine-based system in conjunction with iron pentacarbonyl.⁷⁵

3.4 Experimental Design for Metal–Germanide Nanomaterials

The ubiquity of germanium nanocrystal syntheses using amine solvents such as oleylamine suggested it as a good starting template for conducting experiments into the production of other germanium-based nanomaterials.⁷⁶ Earlier work had presented evidence for the successful incorporation of various dopant atoms into germanium nanocrystals, but was reliant upon the use of a strong external reducing agent (*n*-butyllithium).⁷⁷ To circumvent

potential complications of different precursor reactivity, we adopted a solvothermal reduction of GeBr_2 in oleylamine as our foundation reaction, which results in the production of germanium nanocrystals without the need for any external reducing agent.⁷⁸ For our metal sources, we envisioned the use of $\text{M}(0)$ precursors as ideal candidates due to their generally low thermal decomposition temperatures ($< 200\text{ }^\circ\text{C}$) and fully reduced nature of the metal atom.^{79,80} We believed that by controlling the addition of these complexes into the reaction after nucleation of the germanium nanocrystals we could incorporate the metal into the nanocrystals and induce a phase transformation to metal germanide products upon increased heating.

3.5 Experimental Design for Nickel Silicide Nanowire Arrays

The difficulty in production of freestanding silicon nanomaterials prompted us to pursue a different avenue for the production of metal silicide nanomaterials through sequential synthesis of silicon nanomaterials followed by subsequent metal deposition and annealing to produce the desired silicide. Electroless etching of silicon wafers through the action of silver nitrate (AgNO_3) in an aqueous hydrofluoric acid solution is a very well-studied system for producing aligned, well-defined arrays of silicon nanowires.⁸¹⁻⁸³ Rather than utilizing previously explored metal deposition approaches, we believed that the use of the aforementioned metal(0) precursors as soluble sources of thermally decomposable, free metal atoms might afford an easier approach to metal deposition. We chose nickel as our initial target metal owing to the desirable properties of nickel silicide nanowires as well as the commercial availability of bis(1,5-cyclooctadiene)nickel(0), which readily decomposes at mild temperatures ($\sim 60\text{ }^\circ\text{C}$).

3.6 Results and Discussion

Metal Germanide Nanocrystal Syntheses

The results of the basic germanium-only synthesis are shown in Figure 3.1. The particles are fairly monodisperse and roughly spherical in shape, with an average size of 4.90 ± 0.85 nm. The powder x-ray diffraction of the particles, shown in Figure 3.2, confirms their crystallinity and is consistent with the diamond cubic structure of germanium, with peaks at 27.2° , 45.2° , 53.7° , 65.8° , and 72.7° which correspond to the (111), (200), (311), (400), and (331) planes, respectively.

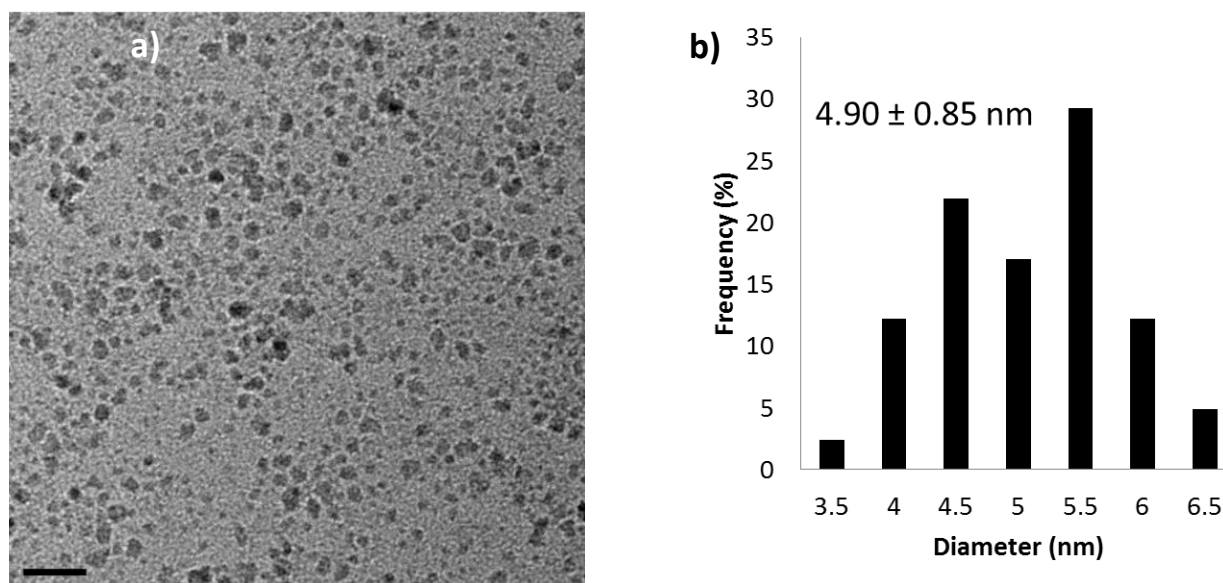


Figure 3.1 a) TEM image (the scalebar is 20 nm) and b) Size histogram of germanium nanocrystals.

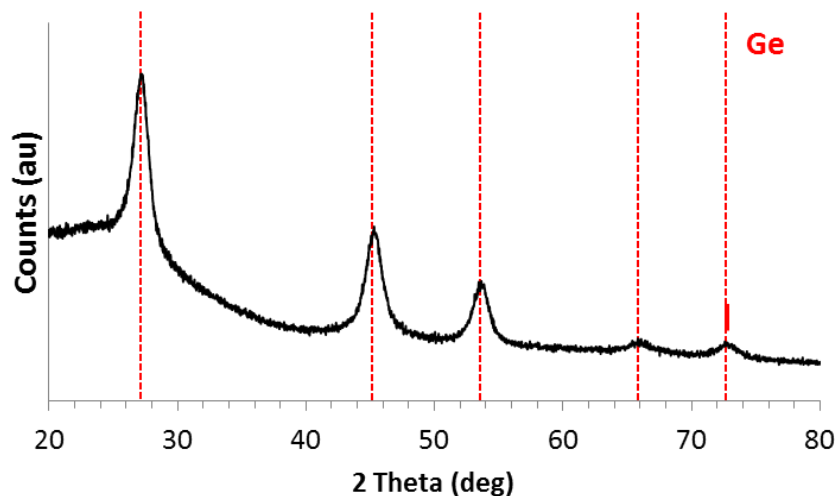


Figure 3.2 Powder x-ray diffraction of germanium nanocrystals.

Infrared spectroscopy of the nanocrystals (Figure 3.3) is consistent with the attachment of oleylamine to the nanocrystal surfaces. The sharp stretches observed around $2800\text{--}3000\text{ cm}^{-1}$ are characteristic of alkyl chain C-H stretching. The two small peaks at 3010 cm^{-1} and 1610 cm^{-1} correspond to =C-H and C=C stretches, respectively, indicative of the carbon-carbon double bond present in oleylamine.

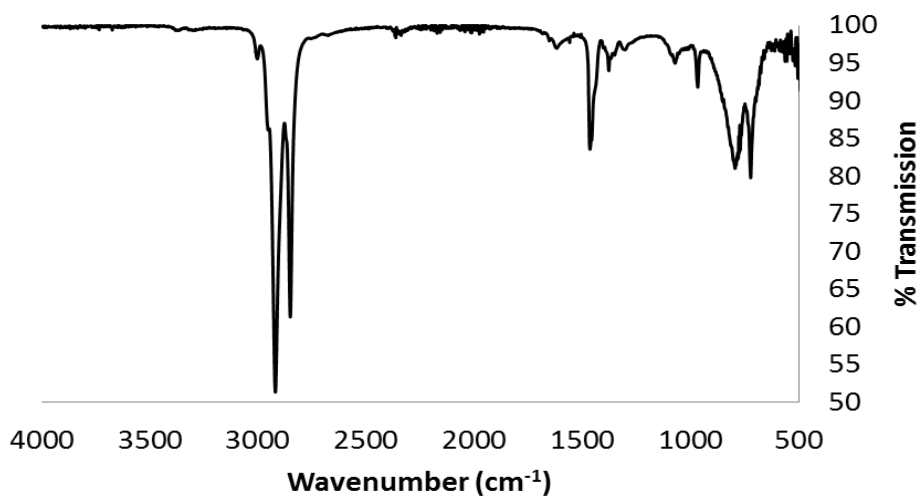


Figure 3.3 Infrared spectrum of germanium nanocrystals synthesized in oleylamine.

Synthesis of Nickel Germanide Nanocrystals Through the Use of Ni(0) Precursors

Nickel was chosen as the starting point for investigating the compatibility of M(0) incorporation. Two different Ni(0) complexes were investigated as metal sources; bis(1,5-cyclooctadiene)nickel(0), “Ni(COD)₂”, and bis(triphenylphosphine)dicarbonylnickel(0) (Figure 3.4). Ni(COD)₂ is an extremely labile compound and decomposes readily at temperatures as low as 60 °C. However, its limited stability even when stored at -80 °C prompted us to explore bis(triphenylphosphine)dicarbonylnickel(0). Solutions of both compounds were prepared in toluene and added dropwise to the reaction upon observation of nanocrystal formation from GeBr₂.

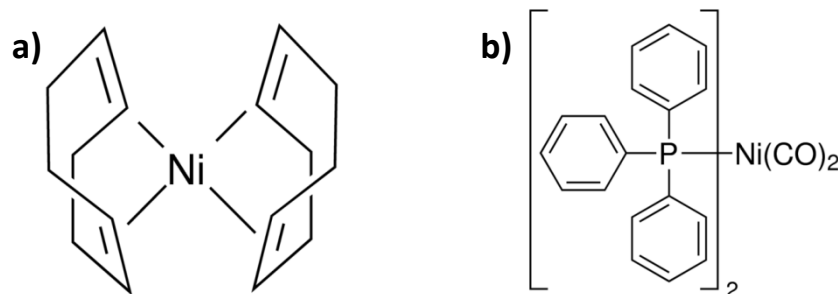


Figure 3.4 Nickel(0) precursors for the synthesis of nickel germanide nanocrystals a) bis(1,5-cyclooctadiene)nickel(0) and b) bis(triphenylphosphine)dicarbonylnickel(0).

Addition of both nickel precursors resulted in an immediate color change in the solution from brown to black. However, upon heating to 300 °C, experiments using the bis(triphenylphosphine)dicarbonylnickel(0) precursor resulted in a blue supernatant with concurrent precipitation of a greyish-white solid. This was accompanied by a very strong ammoniacal odor upon disassembly of the reaction apparatus. No soluble products were obtained

from these reactions. In contrast, the use of $\text{Ni}(\text{COD})_2$ resulted in products that could be redispersed into nonpolar solvents analogously to the products of the germanium only reaction.

The particles produced (Figure 3.5) are spherical and uniform in size and shape, with an average diameter of 11.1 ± 1.2 nm. The particles displayed a very noticeable outer shell lighter in contrast to the core of the particles. This same phenomenon was observed in the colloidal synthesis of iron germanide nanocrystals reported by Schaak and coworkers, whose investigations suggested this lighter contrast region to be an amorphous shell surrounding a crystalline core.⁷⁵

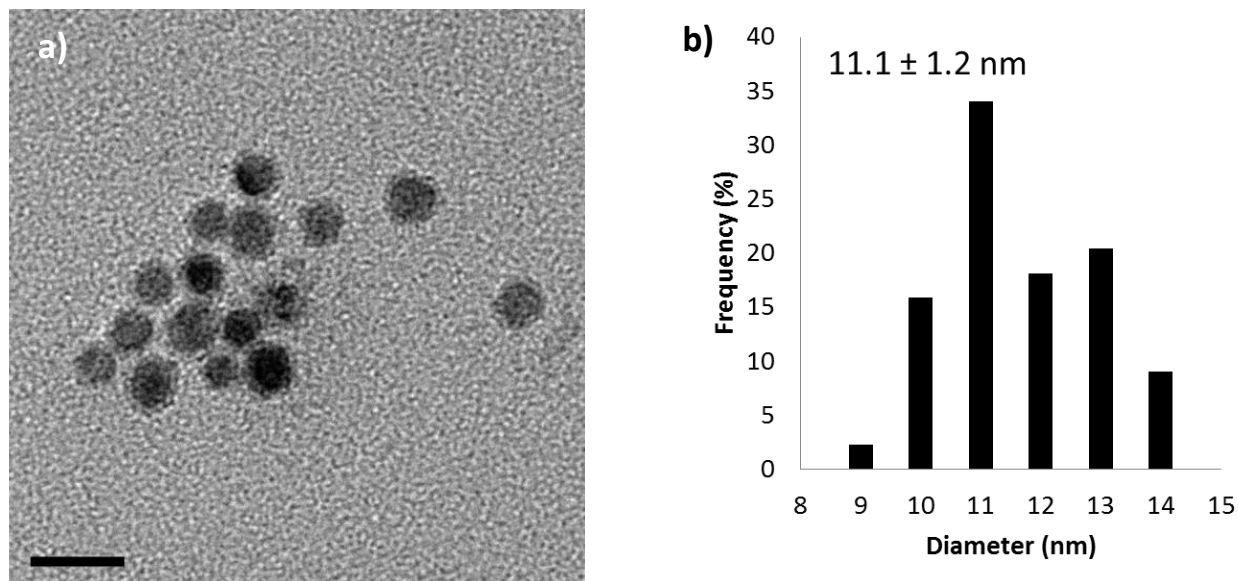


Figure 3.5 a) TEM image and b) Size histogram for nickel germanide nanocrystals produced using $\text{Ni}(\text{COD})_2$. The scalebar for the TEM image is 20 nanometers.

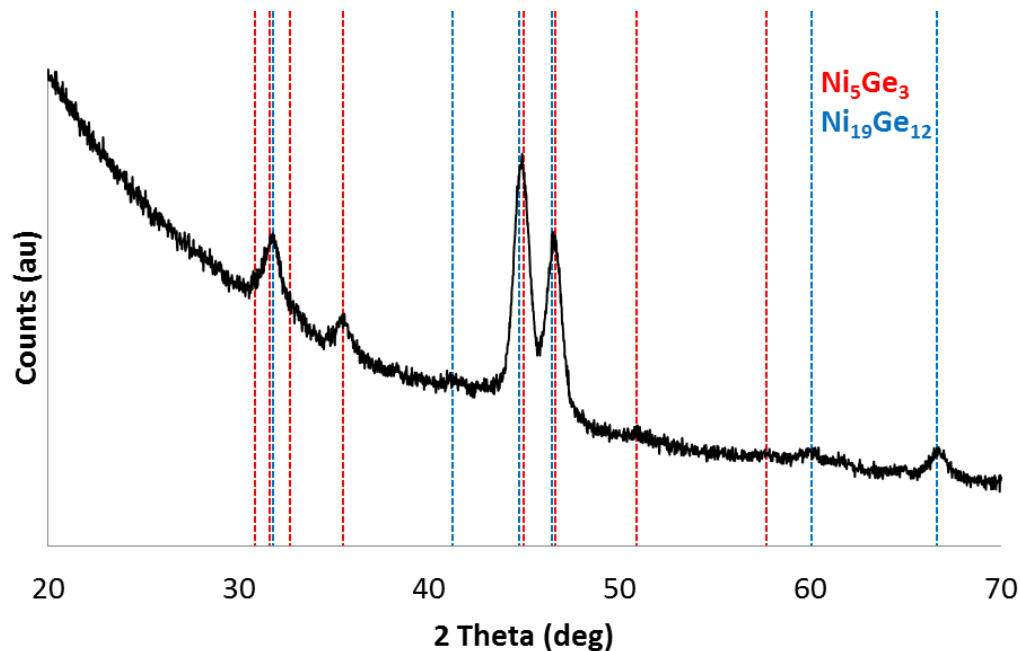


Figure 3.6 XRD of nickel germanide nanocrystals.

Figure 3.6 shows the results of XRD experiments. Powder X-ray diffraction of these products show a number of peaks that correspond to the Ni_5Ge_3 and $\text{Ni}_{19}\text{Ge}_{12}$ phases. This suggests a product composition that is slightly nickel enriched relative to experimental atomic ratios. This is in good agreement with energy dispersive spectroscopy (EDS) results, which consistently indicate a nickel to germanium ratio of approximately 2:1. The decreased germanium content observed in EDS indicates that some germanium is being lost during the course of the reaction. The production of a nickel enriched product was unanticipated, as the phase diagram for nickel germanide (Figure 3.7) suggests that only a NiGe phase should exist under the conditions utilized for this synthesis.⁸⁴ However, deviations in expected phase formation behavior have been observed in a number of other nanomaterials systems for metal silicides and germanides.^{75,85,86} Such deviations are believed to be the result of differences in the effects of strain on nanoscale materials, which can alter the relative thermodynamic stability of

various phases, resulting in the formation of metastable phases.⁸⁷ While this complicates the rational synthesis of specific phases, it also provides the opportunity to access unusual polymorphs not typically observed in bulk materials.

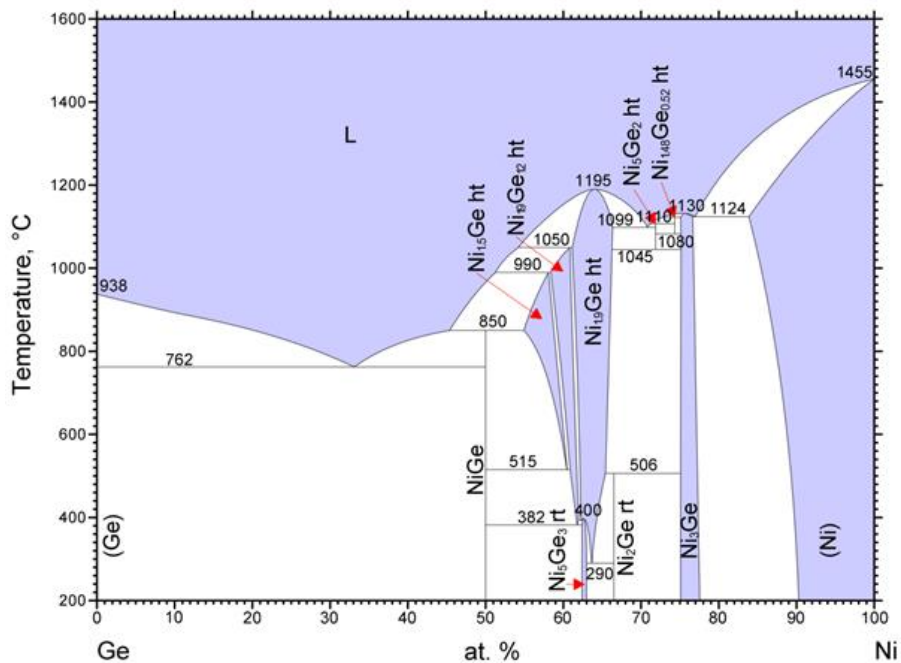


Figure 3.7 Phase diagram for nickel germanide.⁸⁴

Infrared spectroscopy of these products is still consistent with oleylamine bound to the surface of the particles (Figure 3.8), with identical stretching modes observed to those seen for the germanium-only products. This suggests similar surface interactions between the oleylamine and nickel germanide surface compared to the pure germanium nanocrystals. However, these nanocrystals are more prone to precipitation upon extended storage, possibly as a result of greater lability of the oleylamine surface ligands.

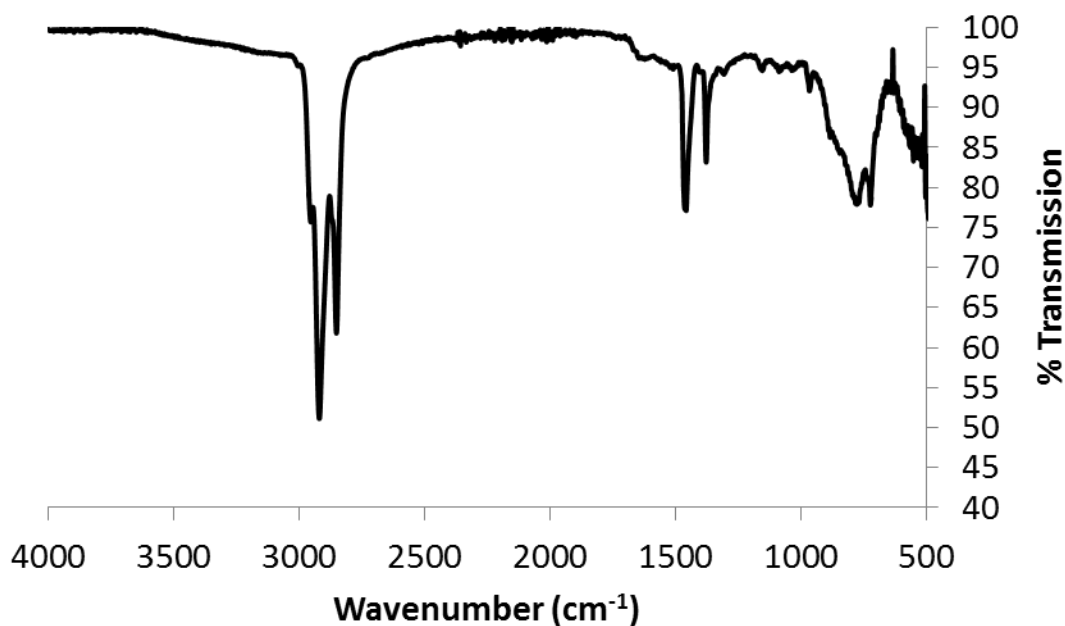


Figure 3.8 Infrared spectrum of nickel germanide nanocrystals.

To summarize, nickel germanide nanocrystals have been successfully synthesized for the first time through a colloidal route. The products are highly crystalline and uniform in size and shape. These results demonstrate the viability of employing molecular M(0) precursors as a method for introducing metal atoms into germanium nanocrystal syntheses to produce metal germanide nanocrystals.

Synthesis of Iron Germanide Nanocrystals Through the Use of Fe(0) Precursors

Iron germanide nanocrystals were examined as the next target for this synthetic system. The first report of a colloidal synthesis of any nanocrystalline metal germanide was for iron germanide, published while this research was underway, which provided a valuable benchmark for us to compare our system to.⁷⁵ The same iron(0) precursor, iron pentacarbonyl, was

employed for this reaction. When injected from toluene at 260 °C and heated to 300 °C, as per the conditions from the nickel germanide synthesis, only brown, amorphous products were obtained. However, lowering the injection temperature to 200 °C and utilizing oleylamine as the carrier solvent for FeCO₅ addition resulted in isolation of a black, crystalline solid. TEM of the material, shown in Figure 3.9, displays somewhat polydisperse particles, with an average size of 9.42 ± 2.75 nm. Many of the particles display a lighter contrast outer shell, as was also observed with the nickel germanide products.

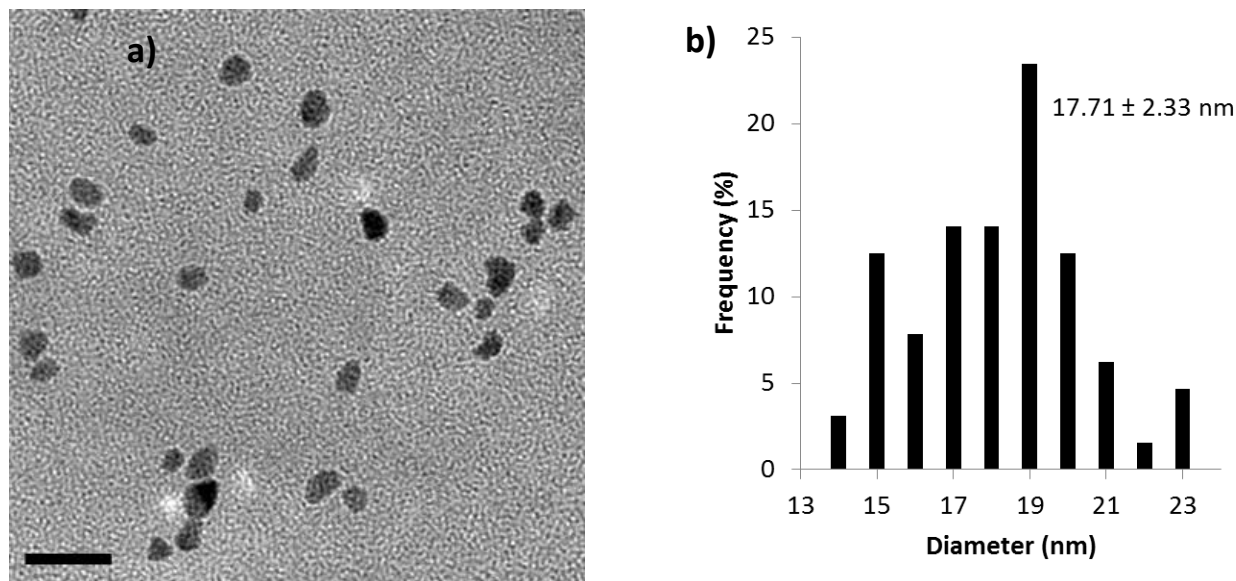


Figure 3.9 a) TEM and b) histogram for particles obtained from the iron germanide synthesis.

The scalebar is 50 nanometers.

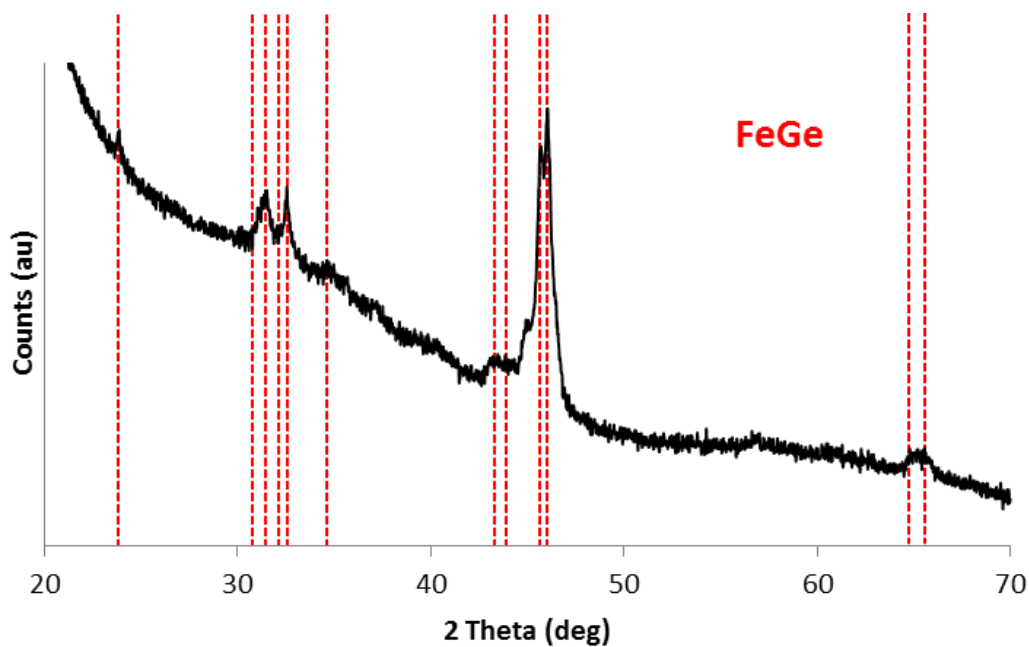


Figure 3.10 XRD of products from iron germanide nanocrystal synthesis.

The XRD pattern for the resulting particles is shown in Figure 3.10. The observed peaks are consistent with FeGe, which appears to be the only phase present, and matches what would be expected from the phase diagram for iron germanide (Figure 3.11).⁸⁴ The results of this synthesis highlight the unpredictable nature of metal germanide phase formation at the nanoscale, as in the experiments with nickel and palladium (shown in the next section), equimolar ratios of precursors resulted in metal rich products. Similarly, in comparison to the results from Schaak and coworkers, their approach, which utilized a more complex solvent system and different germanium source, initially yielded Fe₅Ge₃ nanocrystals at a temperature of 260 °C; lower than was necessary for germanide formation in this system.⁷⁵ Those same nanocrystals eventually formed FeGe nanowires at 300 °C, mimicking the phase behavior we observed, but differing in morphology. These discrepancies highlight the potential versatility and

diligence necessary in exploring a number of variables for these systems- solvents, temperatures, precursor choice, etc.

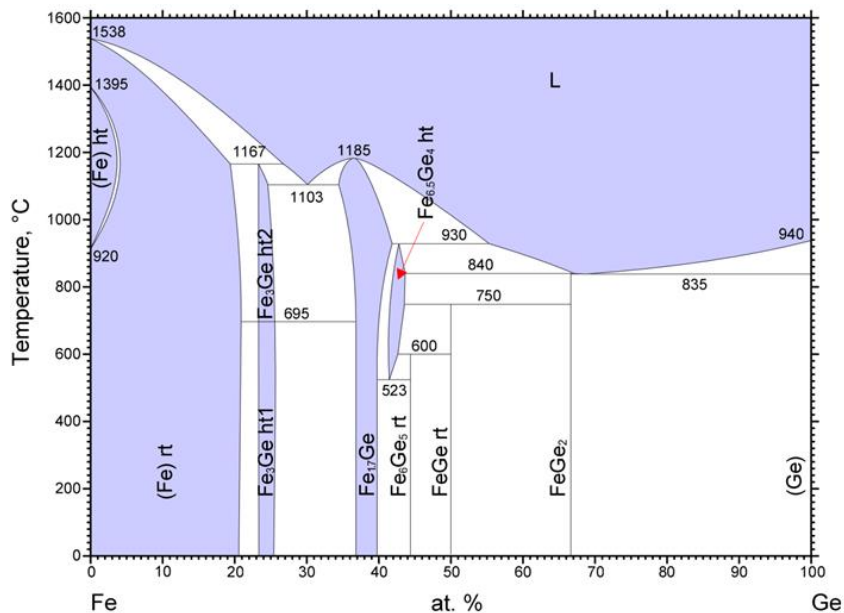


Figure 3.11 Iron germanide phase diagram.⁸⁴

As with earlier experiments, infrared spectroscopy still suggests good surface coverage of the nanocrystals with oleylamine, consistent with their continued solubility in nonpolar solvents. Figure 3.12 shows the spectrum for the iron germanide particles, which is consistent with those shown previously for both the germanium-only products and those from the nickel germanide synthesis.

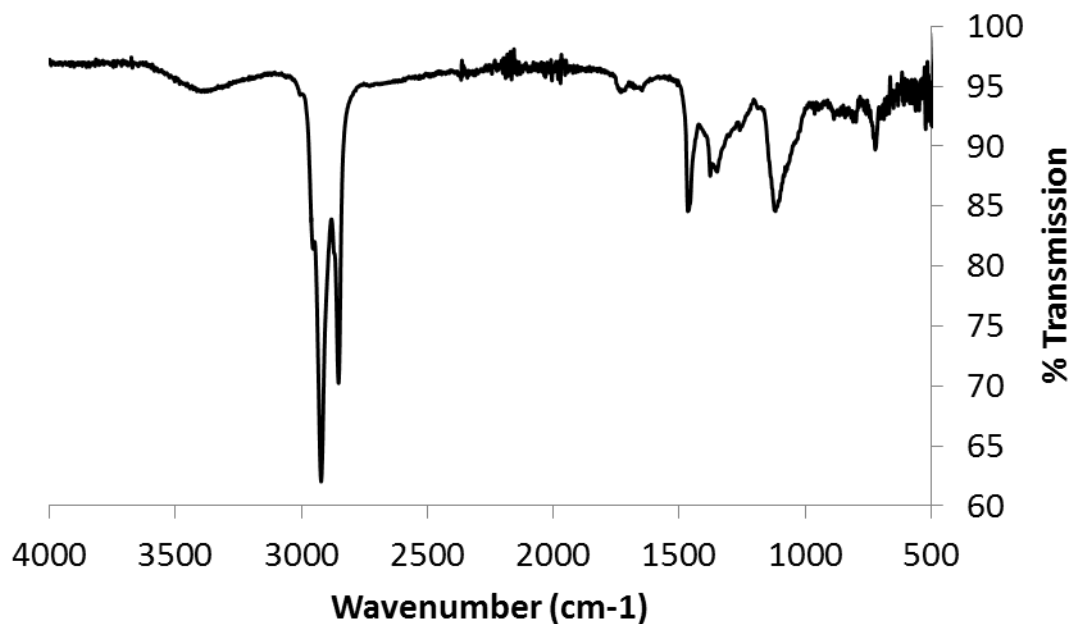


Figure 3.12 Infrared spectrum for iron germanide nanocrystals.

Synthesis of Palladium Germanide Nanocrystals Through the Use of Pd(0) Precursors

To further investigate the scope of the M(0) approach for the production of metal germanide nanocrystals, we next examined the use of tetrakis(triphenylphosphine)palladium(0) for the production of palladium germanide. Tetrakis(triphenylphosphine)palladium was principally chosen for its low decomposition temperature (~ 115 °C), but also for the known compatibility of phosphines in germanium reaction systems. The same synthetic scheme established with the nickel germanide synthesis was followed, utilizing a 50:50 ratio of GeBr_2 and $\text{Pd}(\text{PPh}_3)_4$. The production of freestanding palladium germanide nanomaterials, through colloidal methods or otherwise, at the time of this work, remains completely unexplored.

Figure 3.13 shows a TEM of the products produced from the reaction. In contrast to the particles from nickel and iron, the palladium germanide particles are much smaller in size, with

an average diameter of 3.34 ± 0.94 nm, but still spherical in shape. Unlike with the nickel germanide and iron germanide products, no lighter contrast shell was observed around the outer edge of the particles.

Powder x-ray diffraction of the products, shown in Figure 3.14, reveals that the as synthesized particles display minimal crystallinity. Resuspension of the particles into oleylamine and annealing in solution at 300 °C for 1 hour results in slightly improved crystallinity but gradual loss of solubility. Annealing at 400 °C in a tube furnace under nitrogen for 1 hour results in a crystalline product that matches with Pd₂Ge, however, the resulting black powder is no longer soluble in nonpolar organic solvents, consistent with dissociation/degradation of the oleylamine surface ligands.

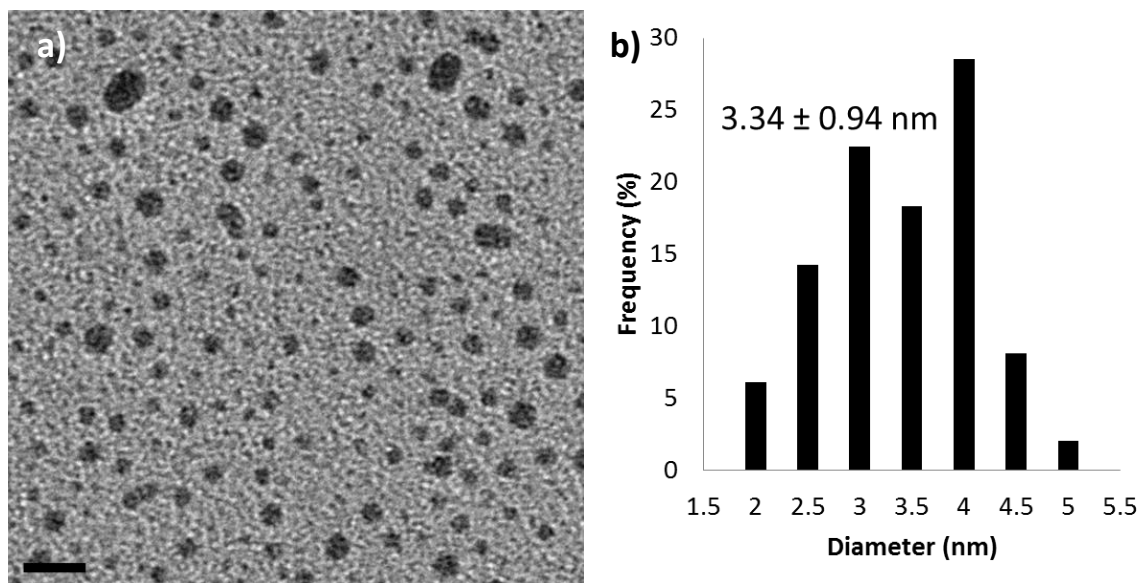


Figure 3.13 a) TEM and b) Size histogram of palladium germanide nanocrystals. The TEM scalebar is 10 nm.

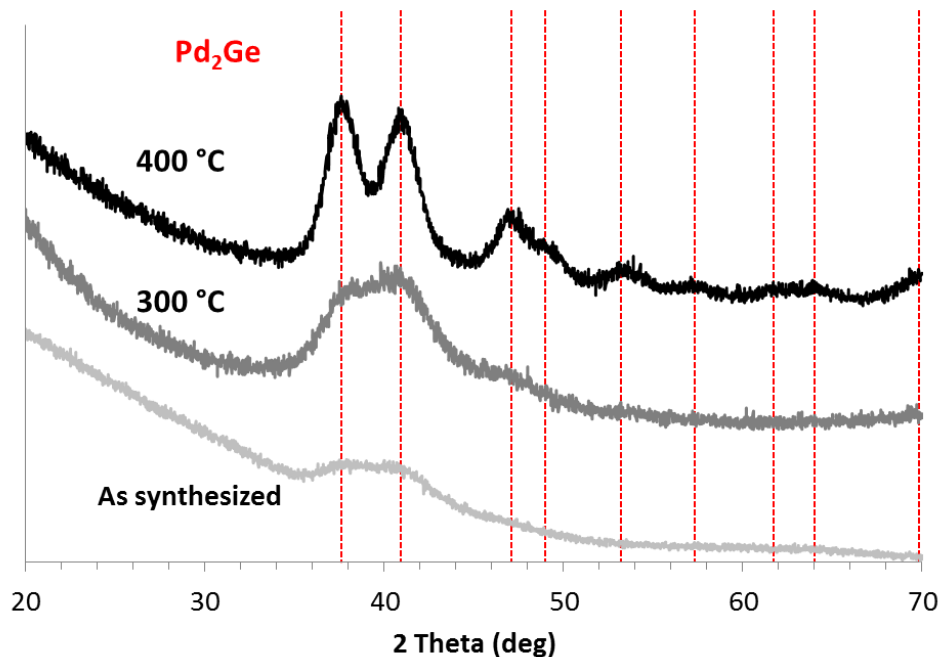


Figure 3.14 Powder XRD of palladium germanide nanocrystals from different processing temperatures.

The infrared spectrum of the resulting particles, shown in Figure 3.15, is also consistent with an oleylamine surface, as would be expected from the continued use of oleylamine as the reaction solvent. The consistency of the oleylamine not only as a suitable reaction solvent but also as a good capping ligand for the metal germanide products has made it a useful tool for these initial synthetic investigations, and suggests that it would be a prime candidate for continued exploration into additional metal germanide systems.

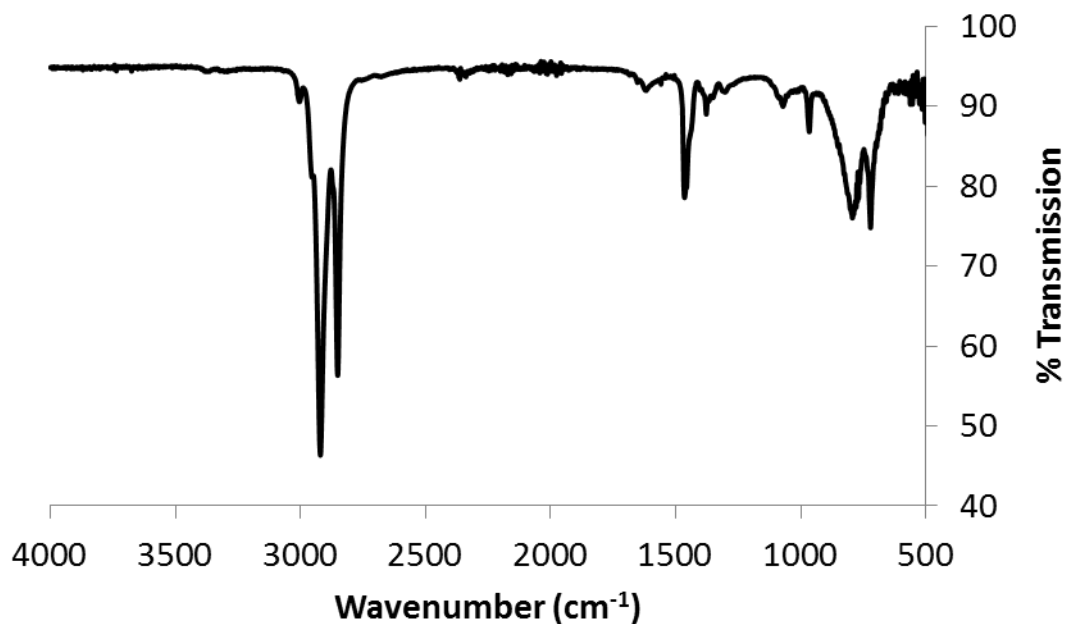
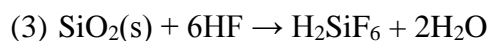
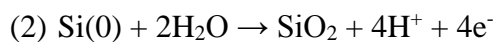
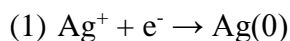


Figure 3.15 Infrared spectrum of palladium germanide nanocrystal products.

Synthesis of Silicon–Nickel Silicide Nanowire Arrays Through Sequential Electroless Etching and Solvothermal Deposition of a Ni(0) Precursor

Electroless etching to produce silicon nanowire arrays has become a popular method for the facile synthesis of large numbers of silicon nanowires. The synthesis of the wires utilizes a galvanic displacement approach in which the surface of a silicon wafer is oxidized through a redox interaction with a suitable electron acceptor, such as silver nitrate, AgNO_3 , and subsequently etched through the action of aqueous hydrofluoric acid.⁸¹⁻⁸³ These reactions can be summarized in the following equations⁸³



A schematic of the reaction is shown in Figure 3.16. Ag^+ ions in solution are reduced by the silicon surface, resulting in nucleation of metallic silver islands on the wafer surface, with concurrent oxidation of the silicon to SiO_2 underneath. This oxide is etched by the hydrofluoric acid in solution, leading to the formation of a pit underneath the deposited silver. Over time, this continued etching results in deep pores in the silicon surface, with nanowires of un-etched silicon produced.⁸¹

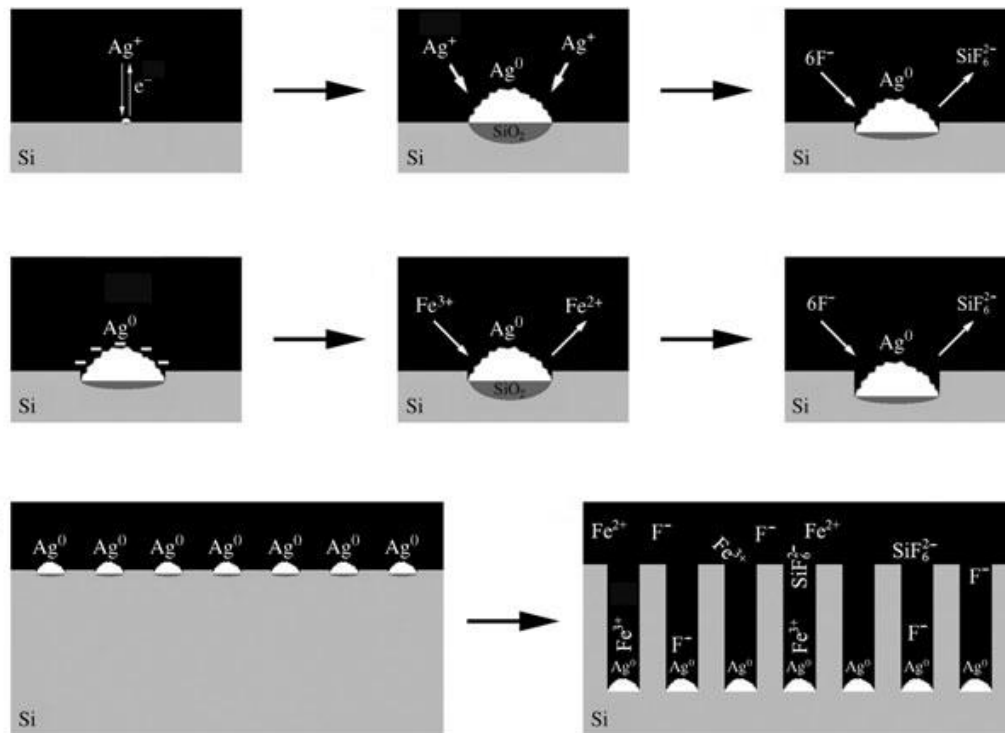


Figure 3.16 Overview of electroless etching process for producing silicon nanowires.⁸¹

The silicon nanowires produced by the procedure outlined in Section 3.5 are shown in Figure 3.17a. Densely packed, aligned wires approximately 25 micrometers in length result from the etching process. After introducing nickel(0) to the nanowire arrays via the thermal decomposition of $\text{Ni}(\text{COD})_2$, nickel islands of approximately 10–50 nm in diameter were observed to have nucleated randomly on the surfaces of the silicon wires (Figure 3.17b). The

thermal decomposition of $\text{Ni}(\text{COD})_2$ is indiscriminant, and results in plating of nickel onto all available surfaces. Suspending the samples in solution was necessary to promote even deposition of nickel throughout the wires and avoid excess deposition on their top portions.

Subsequent annealing of the wires leads to diffusion of the nickel islands into the silicon wire and the formation of nickel silicide phases within the wire. A minimal temperature of 650 °C was found to be necessary to achieve silicide formation. After annealing, nickel silicide phases are visible in TEM (Figure 3.18), as well as in SEM through the use of electron backscattering.

Powder XRD was used to monitor the evolution of the wires throughout the silicidation process. Figure 3.19a shows the pattern of the wires as synthesized, with a single peak corresponding to the (002) reflection. Pattern b, after nickel deposition shows two new nickel peaks at 44.5° and 51.9° corresponding to the (111) and (200) reflections, respectively. After annealing at 650 °C, pattern c displays the appearance of new peaks corresponding to NiSi and NiSi₂ phases around 28.3°, 35.8°, 47.3°, and 56.1°. The peaks observed for nickel in pattern b are also still visible, indicating excess nickel still remains on the surface of the wires, as was also observed in SEM (Figure 3.17c). Removal of the residual nickel deposits via a nickel etchant results in the loss of the nickel peaks in pattern d, leaving only signals attributed to silicon and nickel silicide phases. Nickel silicide phase formation has been well studied in thin film systems, in which experiments have demonstrated nickel to be the dominant diffusing species.⁸⁸⁻⁹⁰ In contrast to bulk systems, thin films will undergo a sequential series of phase transformations under annealing conditions, whereas in bulk, multiple phases are observed to be generated simultaneously.⁸⁵ For the Ni–Si binary system in particular, the first phase generally observed is Ni₂Si, which has been observed at temperatures as low as 200 °C.⁹¹ An increased temperature of

400 °C leads to the formation of NiSi. Finally, NiSi₂ is observed at even higher annealing temperatures of approximately 700 °C and above. Our observation of NiSi₂ is in good agreement with these values.

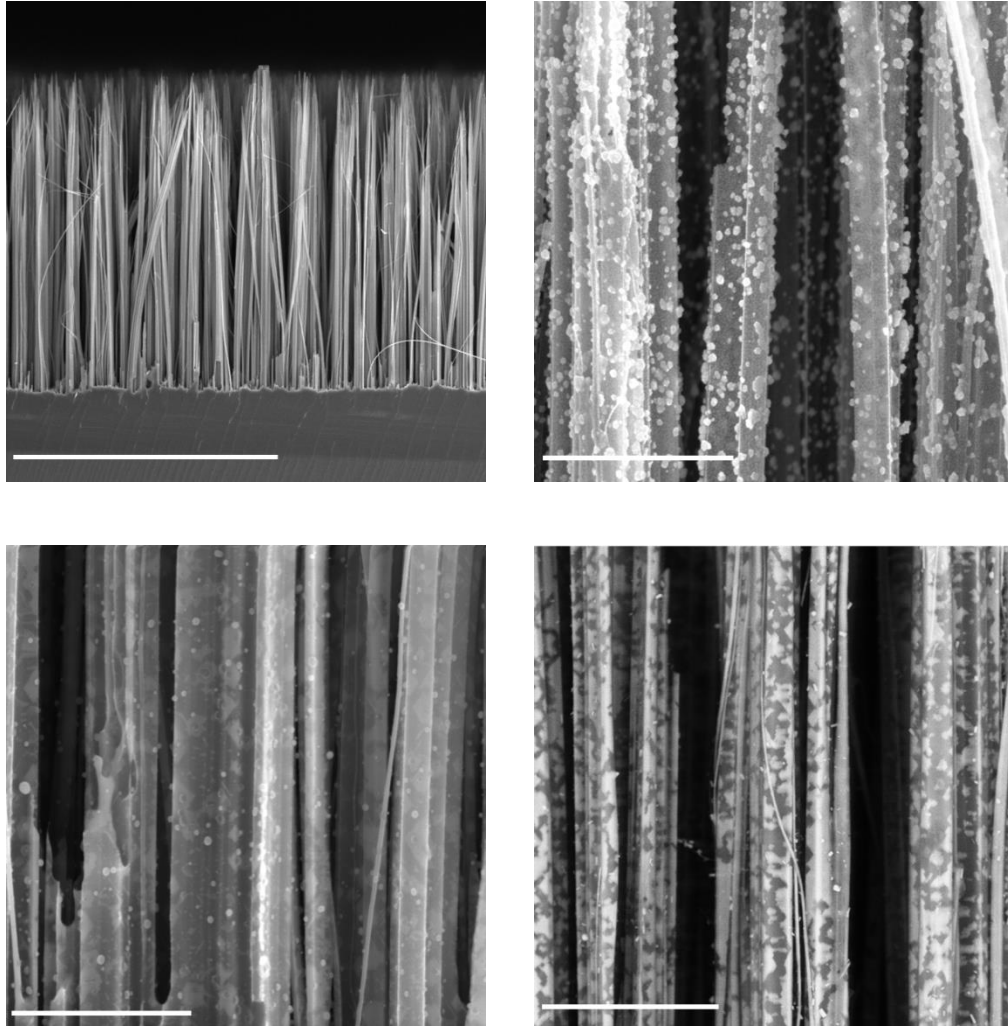


Figure 3.17 SEM images of nanowire synthesis a) Silicon nanowires etched from wafer substrates using AgNO₃ in aqueous HF (20 μm scalebar). b) Nanowires after nickel deposition (1 μm scalebar). c) Nanowires after annealing at 650 °C for 1 hour (1 μm scalebar). d) Electron backscattering image of final nickel silicide nanowires after removal of residual nickel metal (2 μm scalebar).

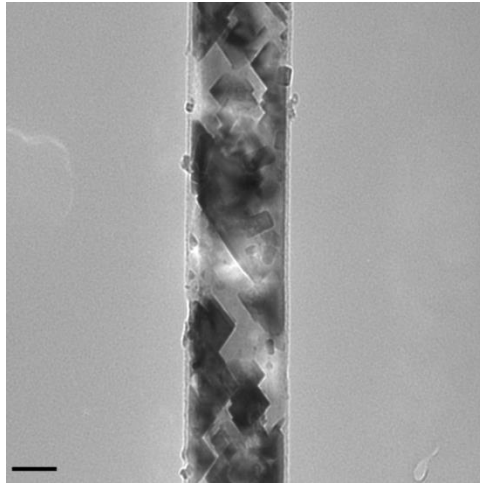


Figure 3.18 Transmission electron image of annealed nickel silicide wire. Scalebar is 100 nm.

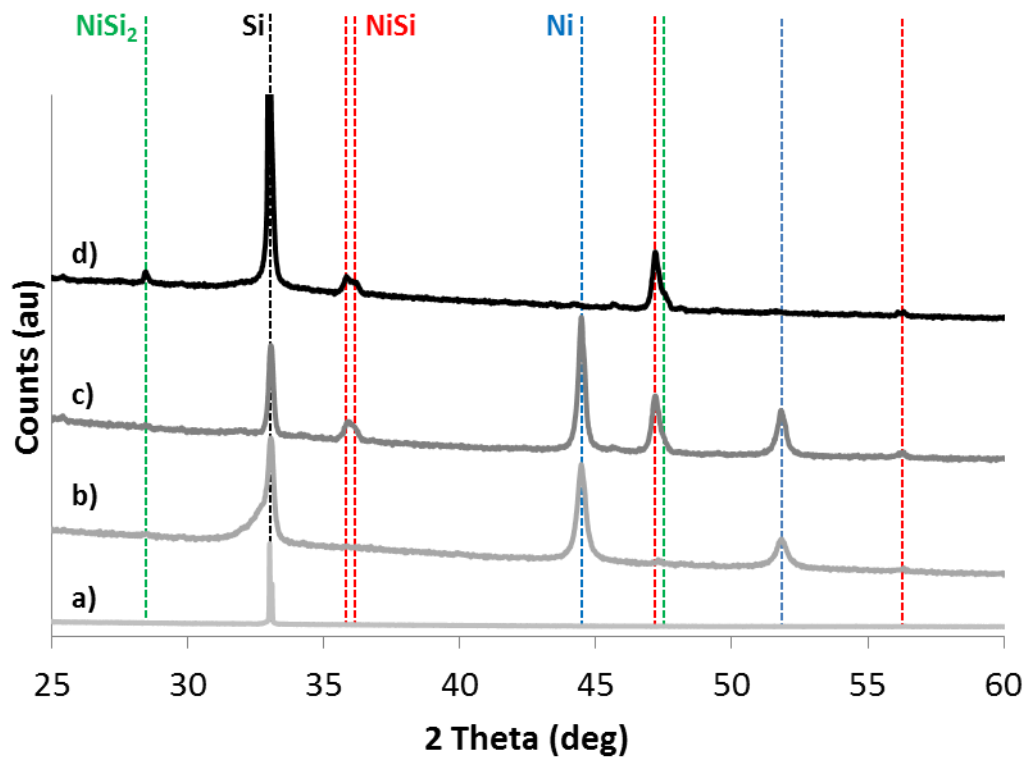


Figure 3.19 XRD series for the silicidation of silicon nanowires. a) Si nanowires as synthesized.

b) After nickel deposition. c) After annealing at 650 °C. d) After residual nickel removal.

The results of this new approach to nickel deposition and annealing are considerably different from preexisting solid state and vapor phase syntheses reported. The deposition of nickel into islands rather than as a thin film results in localized diffusion and nickel silicide formation, producing heterostructured silicon/nickel silicide wires in which clearly defined boundaries between the different phases can be observed. These types of heterostructures have been very valuable in improving the thermoelectric properties of a number of materials, and could hold promise for furthering the development of silicon-based thermoelectric materials.

3.7 Conclusions and Future Work

In this chapter, the colloidal synthesis of several new metal germanide nanocrystals as well as a new approach for the production of heterostructured silicon/nickel silicide nanowires have been described. The results of these experiments provide insight into experimental parameters that provide access to new classes of materials that have, until now, been limited in accessibility, which has hindered attempts to gain a better understanding of their properties.

With the establishment of these synthetic procedures providing a groundwork, investigations into the properties of these materials can begin. Aside from the individually interesting properties these metal germanide nanocrystals may possess, the ability to produce germanium and metal germanide nanocrystals through a similar synthetic protocol should help facilitate future work on surface chemistry modification to aid in the production of heterostructured films for thermoelectric applications, which was a driving force in the development of these methodologies. The production of heterostructured silicon/metal silicide wires, while not our initial intention, is nonetheless an extremely exciting result, and these

products will hopefully produce equally exciting results when their electrical properties are investigated in the future.

3.8 Experimental Procedures

Basic Germanium Synthesis

In a glovebox, 140 mg (0.6 mmol) of germanium dibromide were added to an oven dried three neck round bottom flask, along with 5 ml of degassed oleylamine. A condenser was attached and the apparatus was transferred to a Schlenk line. The reaction was heated to 300 °C at a rate of 10 °C/min and held for one hour. After cooling to room temperature, the solution was transferred to a centrifuge tube with the aid of 10 ml of toluene and precipitated using ethanol. The nanocrystals were purified through repeated solution/precipitation from toluene and ethanol, with approx. 10 drops of oleylamine added to each wash. After the final wash, the particles were resuspended in 5 ml of dry toluene, to which 10 drops of oleylamine were added, and transferred to a scintillation vial, which was stored in a glovebox.

Modification for Nickel Germanide Synthesis

To produce nickel germanide nanocrystals, the apparatus was assembled as per the germanium-only reaction. Separately, 0.165 g (0.6 mmol) of bis(1,5-cyclooctadiene)nickel(0) was dissolved into a minimal amount of toluene (roughly 5 ml). The germanium reaction was heated to 260 °C and held for 5 minutes, during which the toluene solution of Ni(COD)₂ was added dropwise. During addition, a higher positive nitrogen pressure was employed and a vent needle was added to the reaction to allow the toluene vapors to escape without introducing air into the system. After addition, the reaction was heated to 300 °C at 5 °C/min and held for one hour. Purification of the products was performed identically to the germanium only protocol.

Modification for Palladium Germanide Synthesis

To produce palladium germanide nanocrystals, the apparatus was assembled as per the germanium-only reaction, however, 0.070 g (0.3 mmol) of germanium dibromide and 3 ml of oleylamine were used instead. Separately, 0.346 g (0.3 mmol) of tetrakis(triphenylphosphine)palladium(0) was dissolved into a minimal amount of toluene (roughly 5 ml). The germanium reaction was heated to 260 °C and held for 5 minutes, during which the toluene solution of Pd(PPh₃)₄ was added dropwise. During addition, a higher positive nitrogen pressure was employed and a vent needle was added to the reaction to allow the toluene vapors to escape without introducing air into the system. After addition, the reaction was heated to 280 °C at 5 °C/min and held for one hour. Purification of the products was performed identically to the germanium only protocol.

Modification for Iron Germanide Synthesis

To produce iron germanide nanocrystals, the apparatus was assembled as per the germanium-only reaction. Separately, 0.079 ml (0.6 mmol) of iron pentacarbonyl was dissolved into 2 ml of oleylamine and allowed to stir overnight in a glovebox. The germanium reaction was heated to 200 °C and held for 5 minutes, during which the FeCO₅ solution was added. After addition, the reaction was heated to 300 °C at 5 °C/min and held for one hour. Purification of the products was performed identically to the germanium only protocol.

Silicon Nanowire Synthesis

Boron doped p-type (100) silicon wafers were cut into 2 cm² squares and sonicated for 5 minutes each sequentially in acetone, methanol, and Millipore water. The wafers were dried and secured to the bottom of polyethylene beakers using nail polish. Separately, 20 mL of 5M

hydrofluoric acid was diluted into 80 mL of Millipore water containing 0.34 g (0.02 mol) of silver nitrate (AgNO_3). These solutions were added to the sample beakers and left to react for 2 hours. The AgNO_3/HF solution and waste silver byproduct was then decanted and discarded. The wafers were rinsed with Millipore water and isopropanol and dried using compressed air. The wafers were then soaked for 30 minutes in concentrated nitric acid and then rinsed a final time with Millipore water and isopropanol and then dried with compressed air. These nanowire arrays were then stored in a glovebox for future use.

Nickel Deposition and Silicide Formation

In a scintillation vial, 0.025 g (0.09 mmol) of bis(1,5-cyclooctadiene)nickel(0) were dissolved into 10 ml of anhydrous toluene. A silicon nanowire array sample was suspended into the toluene solution, which was heated to 90 °C for 2 hours. After cooling to room temperature, the silicon chip was removed and rinsed with anhydrous toluene, then left to dry in the glovebox.

The samples were placed onto a quartz holder and transferred to a tube furnace. After purging with nitrogen for 10 minutes at room temperature, the furnace was heated to 650 °C at 20 °C/min and annealed for one hour. After cooling to room temperature, excess nickel was removed via a commercial nickel etchant. The samples were placed into the solution, which was heated to 70 °C for 1.5 hours. The cleaned samples were then rinsed with Millipore water and isopropanol, dried using compressed air, and stored in the glovebox.

3.9 References

- (1) van der Meulen, M. I.; Petkov, N.; Morris, M. A.; Kazakova, O.; Han, X.; Wang, K. L.; Jacob, A. P.; Holmes, J. D. *Nano Lett.* **2009**, *9*, 50-56.
- (2) Shepela, A. *Solid State Electron.* **1973**, *16*, 477-481.
- (3) Wittmer, M.; Smith, D. L.; Lew, P. W.; Nicolet, M.-A. *Solid State Electron.* **1978**, *21*, 573-580.
- (4) Chand, S.; Kumar, J. *Solid State Electron.* **1995**, *38*, 1103-1104.
- (5) Wu, Y.; Xiang, J.; Yang, C.; Lu, W.; Lieber, C. M. *Nature* **2004**, *430*, 61-65.
- (6) Chueh, Y. L.; Ko, M.-T.; Chou, L.-J.; Chen, L.-J.; Wu, C.-S.; Chen, C.-D. *Nano Lett.* **2006**, *6*, 1637-1644.
- (7) Kittl, J. A.; Opsomer, K.; Torregiani, C.; Demeurisse, C.; Mertens, S.; Brunco, D. P.; Van Dal, M. J. H.; Lauwers, A. *Mater. Sci. Eng. B* **2008**, *154-155*, 144-154.
- (8) Dellas, N. S.; Minassian, S.; Redwing, J. M.; Mohny, S. E. *Appl. Phys. Lett.* **2010**, *97*, 263116.
- (9) Lin, Y. C.; Chen, Y.; Shailos, A.; Huang, Y. *Nano Lett.* **2010**, *10*, 2281-2287.
- (10) Schmitt, A. L.; Higgins, J. M.; Szczech, J. R.; Jin, S. *J. Mater. Chem.* **2010**, *20*, 223-235.
- (11) Tang, J.; Wang, C.-Y.; Xiu, F.; Zhou, Y.; Chen, L.-J.; Wang, K. L. *Adv. Mater. Sci. Eng.* **2011**, *2011*, 1-16.
- (12) Yan, C.; Higgins, J. M.; Faber, M. S.; Lee, P. S.; Jin, S. *ACS Nano* **2011**, *5*, 5006-5014.
- (13) Dellas, N. S.; Schuh, C. J.; Mohny, S. E. *J. Mater. Sci.* **2012**, *47*, 6189-6205.
- (14) Lin, Y. C.; Chen, Y.; Huang, Y. *Nanoscale* **2012**, *4*, 1412-1421.
- (15) Tsai, C.-Y.; Yu, S.-Y.; Hsin, C.-L.; Huang, C.-W.; Wang, C.-W.; Wu, W.-W. *CrystEngComm* **2012**, *14*, 53-58.

- (16) Yearsley, J. D.; Lin, J. C.; Hwang, E.; Datta, S.; Mohney, S. E. *J. Appl. Phys.* **2012**, *112*, 054510.
- (17) Bower, R. W.; Sigurd, D. *Solid State Electron.* **1973**, *16*, 1461-1471.
- (18) Zhou, A. J.; Zhao, X. B.; Zhu, T. J.; Yang, S. H.; Dasgupta, T.; Stiewe, C.; Hassdorf, R.; Mueller, E. *Mater. Chem. Phys.* **2010**, *124*, 1001-1005.
- (19) Ohishi, Y.; Kurosaki, K.; Suzuki, T.; Muta, H.; Yamanaka, S.; Uchida, N.; Tada, T.; Kanayama, T. *Thin Solid Films* **2013**, *534*, 238-241.
- (20) Fahrnbauer, F.; Souchay, D.; Wagner, G.; Oeckler, O. *J. Am. Chem. Soc.* **2015**, *137*, 12633-12638.
- (21) Fedorov, M. I.; Isachenko, G. N. *Jpn. J. Appl. Phys.* **2015**, *54*, 07JA05.
- (22) Nhi Truong, D. Y.; Berthebaud, D.; Gascoin, F.; Kleinke, H. *J. Electron. Mater.* **2015**, *44*, 3603-3611.
- (23) Tang, J.; Wang, C.-Y.; Hung, M.-H.; Jiang, X.; Chang, L.-T.; He, L.; Liu, P.-H.; Yang, H.-J.; Tuan, H. Y.; Chen, L.-J.; Wang, K. L. *ACS Nano* **2012**, *6*, 5710-5717.
- (24) McEnaney, J. M.; Schaak, R. E. *Inorg. Chem.* **2015**, *54*, 707-709.
- (25) Vijh, A. K.; Belanger, G.; Jacques, R. *Int. J. Hydrogen Energy* **1990**, *15*, 789-794.
- (26) Murarka, S. P. *Intermetallics* **1995**, *3*, 173-186.
- (27) Colgan, E. G.; Gambino, J. P.; Hong, Q. Z. *Mater. Sci. Eng.* **1996**, *R16*, 43-96.
- (28) Sun, H. P.; Chen, Y. B.; Pan, X. Q.; Chi, D. Z.; Nath, R.; Foo, Y. L. *Appl. Phys. Lett.* **2005**, *87*, 211909.
- (29) Agnello, P. D.; Kesan, V. P.; Tejawani, M.; Ott, J. A. *J. Electron. Mater.* **1994**, *23*, 413-421.

- (30) Cho, Y. J.; Kim, C. H.; Im, H. S.; Myung, Y.; Kim, H. S.; Back, S. H.; Lim, Y. R.; Jung, C. S.; Jang, D. M.; Park, J.; Lim, S. H.; Cha, E. H.; Bae, K. Y.; Song, M. S.; Cho, W. I. *Phys. Chem. Chem. Phys.* **2013**, *15*, 11691-11695.
- (31) Leong, D.; Harry, M.; Reeson, K. J.; Homewood, K. P. *Nature* **1997**, *387*, 686-688.
- (32) Yoon, H.-N.; Yoo, Y.-D.; Seo, K.-Y.; In, J.-H.; Kim, B.-S. *B. Kor. Chem. Soc.* **2012**, *33*, 2830-2844.
- (33) Liang, S.; Islam, R.; Smith, D. J.; Bennett, P. A.; O'Brien, J. R.; Taylor, B. *Appl. Phys. Lett.* **2006**, *88*, 113111.
- (34) Ramasamy, K.; Kotula, P. G.; Fidler, A. F.; Brumbach, M. T.; Pietryga, J. M.; Ivanov, S. *A. Chem. Mater.* **2015**, *27*, 4640-4649.
- (35) Khyzhun, O. Y.; Zaulychny, Y. V.; Zhurakovsky, E. A. *J. Alloy. Compd.* **1996**, *244*, 107-112.
- (36) Gaudet, S.; Detavernier, C.; Kellock, A. J.; Desjardins, P.; Lavoie, C. *J. Vac. Sci. Technol. A* **2006**, *24*, 474.
- (37) Chen, L.-J.; Wu, W.-W. *Jpn. J. Appl. Phys.* **2015**, *54*, 07JA04.
- (38) Kang, K.; Kim, S.-K.; Kim, C.-J.; Jo, M.-H. *Nano Lett.* **2008**, *8*, 431-436.
- (39) Zeng, C.; Kent, P. R. C.; Varela, M.; Eisenbach, M.; Stocks, G. M.; Torija, M.; Shen, J.; Weitering, H. H. *Phys. Rev. Lett.* **2006**, *96*.
- (40) Liu, B.; Wang, Y.; Dilts, S.; Mayer, T. S.; Mohny, S. E. *Nano Lett.* **2007**, *7*, 818-824.
- (41) Seo, K.; Varadwaj, K. S. K.; Cha, D.; In, J.; Kim, J.; Park, J.; Kim, B. *J. Phys. Chem. C* **2007**, *111*, 9072-9076.
- (42) Schmitt, A. L.; Bierman, M. J.; Schmeisser, D.; Himpfel, F. J.; Jin, S. *Nano Lett.* **2006**, *6*, 1617-1621.

- (43) Schmitt, A. L.; Zhu, L.; Schmeiber, D.; Himpsel, F. J.; Jin, S. *J. Phys. Chem. B Lett.* **2006**, *110*, 18142-18146.
- (44) Du, J.; Du, P.; Hao, P.; Huang, Y.; Ren, Z.; Han, G.; Weng, W.; Zhao, G. *J. Phys. Chem. C* **2007**, *111*, 10814-10817.
- (45) Yamamoto, K.; Kohno, H.; Takeda, S.; Ichikawa, S. *Appl. Phys. Lett.* **2006**, *89*, 083107.
- (46) Varadwaj, K. S. K.; Seo, K.; In, J.; Mohanty, P.; Park, J.; Kim, B. *J. Am. Chem. Soc.* **2007**, *129*, 8594-8599.
- (47) Schmitt, A. L.; Jin, S. *Chem. Mater.* **2007**, *19*, 126-128.
- (48) In, J.; Varadwaj, K. S. K.; Seo, K.; Lee, S.; Jo, Y.; Jung, M.-H.; Kim, J.; Kim, B. *J. Phys. Chem. C* **2008**, *112*, 4748-4752.
- (49) Seo, K.; Varadwaj, K. S. K.; Mohanty, P.; Lee, S.; Jo, Y.; Jung, M.-H.; Kim, J.; Kim, B. *Nano Lett.* **2007**, *7*, 1240-1245.
- (50) Seo, K.; Lee, S.; Yoon, H.; In, J.; Varadwaj, K. S. K.; Jo, Y.; Jung, M.-H.; Kim, J.; Kim, B. *ACS Nano* **2009**, *3*, 1145-1150.
- (51) Chou, Y.-C.; Wu, W.-W.; Cheng, S.-L.; Yoo, B.-Y.; Myung, N.; Chen, L. J.; Tu, K. N. *Nano Lett.* **2008**, *8*, 2194-2199.
- (52) Lu, K.-C.; Wu, W.-W.; Wu, H.-W.; Tanner, C. M.; Chang, J. P.; Chen, L. J.; Tu, K. N. *Nano Lett.* **2007**, *7*, 2389-2394.
- (53) Song, Y.; Schmitt, A. L.; Jin, S. *Nano Lett.* **2007**, *7*, 965-969.
- (54) Song, Y.; Jin, S. *Appl. Phys. Lett.* **2007**, *90*, 173122.
- (55) Lee, C.-Y.; Lu, M.-P.; Liao, K.-F.; Wu, W.-W.; Chen, L.-J. *Appl. Phys. Lett.* **2008**, *93*, 113109.

- (56) Kim, J.; Shin, D. H.; Lee, E.-S.; Han, C.-S.; Park, Y. C. *Appl. Phys. Lett.* **2007**, *90*, 253103.
- (57) Lee, C.-Y.; Lu, M.-P.; Liao, K.-F.; Lee, W.-F.; Huang, C.-T.; Chen, S.-Y.; Chen, L.-J. *J. Phys. Chem. C* **2009**, *113*, 2286-2289.
- (58) Szczech, J. R.; Schmitt, A. L.; Bierman, M. J.; Jin, S. *Chem. Mater.* **2007**, *19*, 3238-3243.
- (59) Yu, L.; Ma, Y.; Zhu, J.; Feng, H.; Wu, Q.; Lu, Y.; Lin, W.; Sang, H.; Hu, Z. *J. Phys. Chem. C* **2008**, *112*, 5865-5868.
- (60) Geaney, H.; Dickinson, C.; O'Dwyer, C.; Mullane, E.; Singh, A.; Ryan, K. M. *Chem. Mater.* **2012**, *24*, 4319-4325.
- (61) Xiang, B.; Wang, Q. X.; Wang, Z.; Zhang, X. Z.; Liu, L. Q.; Xu, J.; Yu, D. P. *Appl. Phys. Lett.* **2005**, *86*, 243103.
- (62) Chang, C.-M.; Chang, Y.-C.; Chung, Y.-A.; Lee, C.-Y.; Chen, L.-J. *J. Phys. Chem. C* **2009**, *113*, 17720-17723.
- (63) Zhou, S.; Liu, X.; Lin, Y.; Wang, D. *Chem. Mater.* **2009**, *21*, 1023-1027.
- (64) Lin, H.-K.; Tzeng, Y.-F.; Wang, C.-H.; Tai, N.-H.; Lin, I.-N.; Lee, C.-Y.; Chiu, H.-T. *Chem. Mater.* **2008**, *20*, 2429-2431.
- (65) Chang, C.-M.; Chang, Y.-C.; Lee, C.-Y.; Yeh, P.-H.; Lee, W.-F.; Chen, L.-J. *J. Phys. Chem. C* **2009**, *113*, 9153-9156.
- (66) Chueh, Y. L.; Chou, L. J.; Cheng, S. L.; Chen, L. J.; Tsai, C. J.; Hsu, C. M.; Kung, S. C. *Appl. Phys. Lett.* **2005**, *87*, 223113.
- (67) Ham, M.-H.; Lee, J.-W.; Moon, K.-J.; Choi, J.-H.; Myoung, J.-M. *J. Phys. Chem. C* **2009**, *113*, 8143-8146.

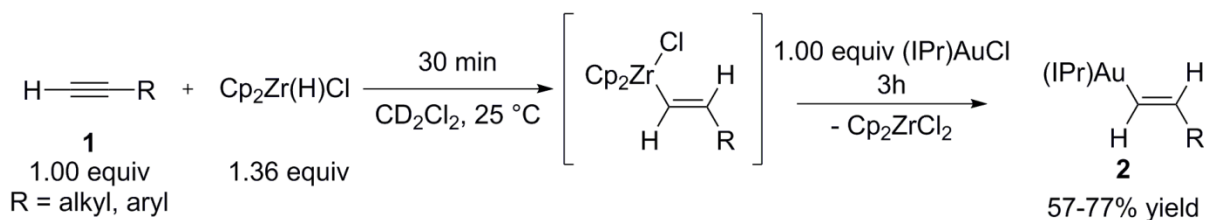
- (68) Higgins, J. M.; Schmitt, A. L.; Guzei, I. A.; Jin, S. *J. Am. Chem. Soc.* **2008**, *130*, 16086-16094.
- (69) Dahal, N.; Chikan, V. *Chem. Mater.* **2010**, *22*, 2892-2897.
- (70) Lu, X.; Korgel, B. A. *Chemistry* **2014**, *20*, 5874-5879.
- (71) Yoon, H.; Lee, A. T.; Choi, E.-A.; Seo, K.; Bagkar, N.; Cho, J.; Jo, Y.; Chang, K. J.; Kim, B. *J. Am. Chem. Soc.* **2010**, *132*, 17447-17451.
- (72) Yoon, H.; Kang, T.; Lee, J. M.; Kim, S.-i.; Seo, K.; Kim, J.; Park, W. I.; Kim, B. *J. Phys. Chem. Lett.* **2011**, *2*, 956-960.
- (73) Tang, J.; Wang, C. Y.; Xiu, F.; Hong, A. J.; Chen, S.; Wang, M.; Zeng, C.; Yang, H. J.; Tuan, H. Y.; Tsai, C. J.; Chen, L. J.; Wang, K. L. *Nanotechnol.* **2010**, *21*, 505704.
- (74) Yoon, H.; Seo, K.; Bagkar, N.; In, J.; Park, J.; Kim, J.; Kim, B. *Adv. Mater.* **2009**, *21*, 4979-4982.
- (75) D. Vaughn Ii, D.; Sun, D.; Moyer, J. A.; Biacchi, A. J.; Misra, R.; Schiffer, P.; Schaak, R. *E. Chem. Mater.* **2013**, *25*, 4396-4401.
- (76) Vaughn, D. D., 2nd; Schaak, R. E. *Chem. Soc. Rev.* **2013**, *42*, 2861-2879.
- (77) Ruddy, D. A.; Erslev, P. T.; Habas, S. E.; Seabold, J. A.; Neale, N. R. *J. Phys. Chem. Lett.* **2013**, *4*, 416-421.
- (78) Xue, D. J.; Wang, J. J.; Wang, Y. Q.; Xin, S.; Guo, Y. G.; Wan, L. J. *Adv. Mater.* **2011**, *23*, 3704-3707.
- (79) Fillman, L. M.; Tang, S. C. *Thermochim. Acta* **1984**, *75*, 71-84.
- (80) Chamberlain, T. W.; Zoberbier, T.; Biskupek, J.; Botos, A.; Kaiser, U.; Khlobystov, A. *N. Chem. Sci.* **2012**, *3*, 1919.

- (81) Peng, K.; Wu, Y.; Fang, H.; Zhong, X.; Xu, Y.; Zhu, J. *Angew. Chem. Int. Ed. Engl.* **2005**, *44*, 2737-2742.
- (82) Peng, K.-Q.; Yan, Y.-J.; Gao, S.-P.; Zhu, J. *Adv. Mater.* **2002**, *14*, 1164-1167.
- (83) Peng, K.; Yan, Y.; Gao, S.; Zhu, J. *Adv. Func. Mater.* **2003**, *13*, 127-132.
- (84) ASM International Alloy Phase Diagram Database. November 2, 2015.
<http://www1.asminternational.org/asmenterprise/apd/>.
- (85) Gösele, U. *J.Appl. Phys.* **1982**, *53*, 3252.
- (86) Nemouchi, F.; Mangelinck, D.; Lábár, J. L.; Putero, M.; Bergman, C.; Gas, P. *Microelectron. Eng.* **2006**, *83*, 2101-2106.
- (87) Johnson, W. C.; Martin, G. *J.Appl. Phys.* **1990**, *68*, 1252.
- (88) Tu, K. N.; Ottaviani, G.; Gösele, U.; Föll, H. *J.Appl. Phys.* **1983**, *54*, 758.
- (89) d'Heurle, F.; Petersson, C. S.; Baglin, J. E. E.; La Placa, S. J.; Wong, C. Y. *J.Appl. Phys.* **1984**, *55*, 4208.
- (90) Comrie, C. M.; Smeets, D.; Pondo, K. J.; der Walt, C. v.; Demeulemeester, J.; Knaepen, W.; Detavernier, C.; Habanyama, A.; Vantomme, A. *Thin Solid Films* **2012**, *526*, 261-268.
- (91) Julies, B. A.; Knoesen, D.; Pretorius, R.; Adams, D. *Thin Solid Films* **1999**, *347*, 201-207.

Chapter 4: The Synthesis of Alkenylgold(I) Complexes via Sequential Hydrozirconation and Zirconium to Gold Transmetalation

4.1 Introduction

The development of homogeneous gold(I) catalysis within the past decade has been largely founded upon the intermediacy of organogold(I) complexes and especially stereodefined alkenylgold(I) complexes.¹⁻¹⁵ Synthetic methods for preparing alkenylgold complexes, in order to probe their reactivity and for mechanistic studies, are generally limited to transmetalation of gold(I) precursors with Grignard reagents,^{16,17} organolithium reagents,^{13,17} or boronic acids.^{9,18-21} A subset of alkenylgold(I) complexes also have been synthesized by gold-mediated cyclizations of substrates containing π systems, a route first demonstrated by Hammond,^{8,9,11-18,22,23} or by palladium-catalyzed carboauration of alkynes.²⁴ Although effective, these methods each have limitations. Grignard and organolithium reagents are incompatible with numerous functional groups, including esters and bromides, and the preparation and trapping of stereochemically pure Grignard reagents is often challenging.²⁵ Boronic acids and esters are more functional group tolerant,^{18,20,21} but their application in synthesizing alkenylgold compounds thus far is limited.¹⁸ Generation by gold-mediated cyclization often involves multistep substrate synthesis. Palladium-catalyzed carboauration is limited to the synthesis of α -aurated vinyl esters.²⁴ Here, we present a new, stereoselective synthesis of (*E*)-alkenylgold compounds through a one-pot hydrozirconation/transmetalation sequence that is tolerant of ester and halide functional groups.



Scheme 4.1: Synthetic scheme for the production of (*E*)-alkenylgold(I) compounds from terminal alkynes through a one-pot sequential hydrozirconation and transmetalation.

Hydrozirconation of alkynes provides a useful starting point for organogold synthesis, due to robust literature precedent, high regio- and stereoselectivity of the Zr–H addition, and a diverse set of commercially available or readily accessible functionalized alkyne starting materials.^{26–30} This work also provides an early example of transmetalation from zirconium to gold.³¹

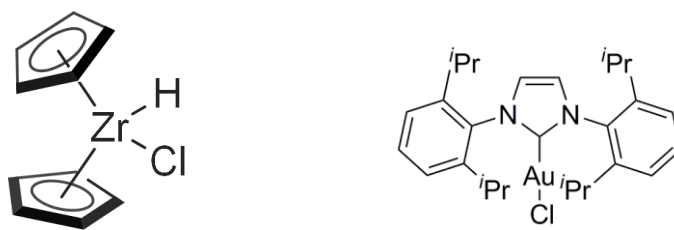


Figure 4.1: Precursor reagents for the synthesis of alkenylgold(I) complexes. Left: Schwartz's reagent. Right: (2,6-diisopropylphenyl)imidazol-2-ylidene)gold(I) chloride.

4.2 Results and Discussion

Terminal alkynes **1a–h** were hydrozirconated with zirconocene hydrochloride, Schwartz's reagent, (Figure 4.1) in deuterated dichloromethane, at 25 °C under an inert

atmosphere (Scheme 4.1). A slight excess of Schwartz's reagent was used to compensate for the presence of Cp_2ZrCl_2 in the purchased reagent and ensure complete conversion to the hydrozirconated intermediates. This complete conversion was observed within 30 min by ^1H NMR spectroscopy. In all cases, addition of the zirconium to the less sterically hindered terminal carbon was observed, consistent with the well-established regioselectivity of Schwartz's reagent.^{26,27,30} After formation of the alkenylzirconium intermediate, addition of 1.00 equiv of $(\text{IPr})\text{AuCl}$ ($\text{IPr} = (2,6\text{-diisopropylphenyl})\text{imidazol-2-ylidene}$) (Figure 4.1) led to transmetalation and formation of the final organogold(I) product. The reaction was monitored for completion via ^1H NMR spectroscopy. Alkynes containing alkyl and aryl groups (**1a,f**), protected alcohols (**1b**), tert-butyl esters (**1c**), ethers (**1h**), and halides (**1d,e,g**) were effective substrates (Table 4.1). ^1H NMR spectroscopy yields were high, consistently reaching >90% conversion.

Initially, isolation of the alkenylgold products in the presence of the Cp_2ZrCl_2 byproduct proved challenging. Isolation was accomplished through extraction of the product using 1:1 hexanes:diethyl ether, followed by filtration through a short basic alumina column. The presence of residual water on the alumina was found to be deleterious, and the use of oven-dried basic alumina was critical in preventing protodeauration side reactions that may have been promoted by the presence of the residual Lewis acidic Cp_2ZrCl_2 ;³² however, the employment of oven-dried alumina fully solved this complication, and all products were isolated with analytical purity (57–77% yield). In all cases except from alkyne **1e**, which will be discussed later, products consisted exclusively of the *E* isomer. This is consistent with the established *syn* addition of Schwartz's reagent across the alkyne, followed by transmetalation from zirconium to gold with retention of stereochemistry.

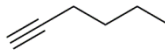
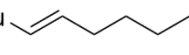
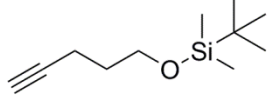
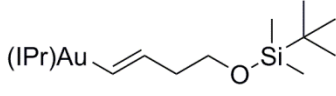
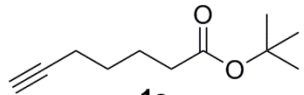
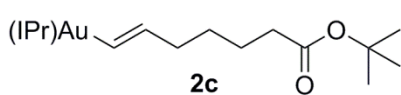
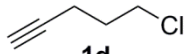
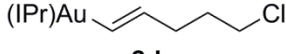
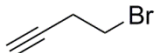
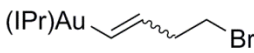
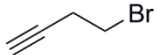
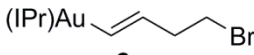
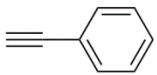
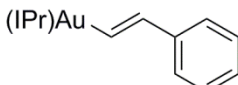
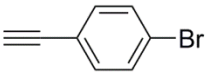
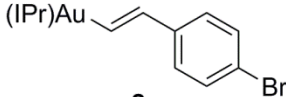
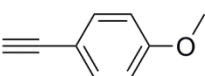
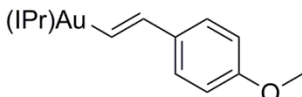
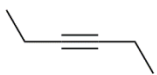
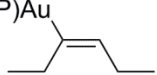
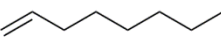
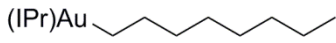
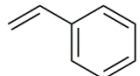
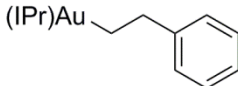
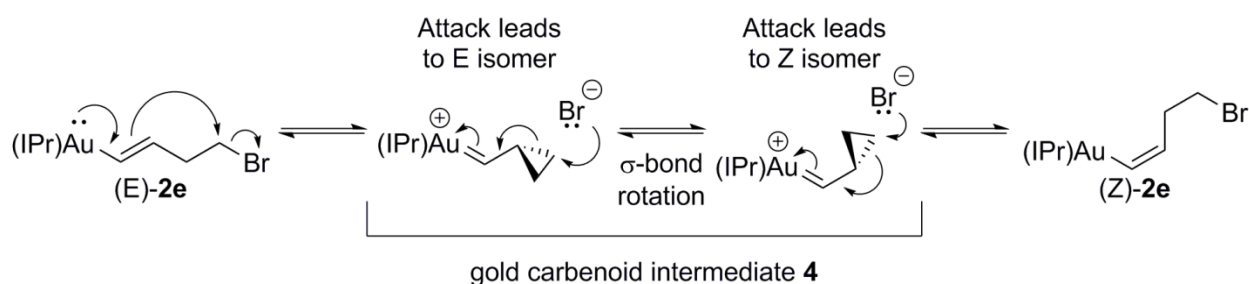
Substrate	Product	Yield (%)
 1a	(IPr)Au  2a	72%
 1b	(IPr)Au  2b	57%
 1c	(IPr)Au  2c	62%
 1d	(IPr)Au  2d	68%
 1e	(IPr)Au  2e	66% (4:1 <i>E:Z</i>)
 1e	(IPr)Au  2e	(100%) ^a (>95% <i>E</i>)
 1f	(IPr)Au  2f	77%
 1g	(IPr)Au  2g	62%
 1h	(IPr)Au  2h	65%
 1i	(Ph ₃ P)Au  2i	0% ^b
 1j	(IPr)Au  2j	(~50%) ^c
 1k	(IPr)Au  2k	trace ^c

Table 4.1: Reaction substrate scope. ^aThe reaction was run in C₆D₆ and the product was not isolated. ^bPPh₃AuCl was used as the gold precursor; the product decomposed during purification. ^cObserved by ¹NMR spectroscopy after 3 days; not isolated.

Subjecting internal alkyne **1i** to hydrozirconation produced the corresponding hydrozirconated intermediate; however, the transmetalation of this internal organozirconium to (IPr)AuCl was unsuccessful, even upon heating at 60 °C. Switching the gold(I) precursor to Ph₃PAuCl led to transmetalation without heating; however, the resulting product was not stable and decomposed during purification. We suspect that these differences in reactivity and stability are due to the steric bulk of the IPr ligand being greater than that of PPh₃.



Scheme 4.2: Proposed isomerization of compound **2e** through a gold carbenoid intermediate. Electron donation from gold induces carbenoid formation. Attack by the released bromide ion reestablishes the alkenylgold species. σ -bond rotation prior to attack determines the resulting isomer.

The stereochemical outcome of the reaction of alkyne **1e**, containing a tethered alkyl bromide, was the only example in the study to yield a mixture of diastereomeric organogold products. The hydrozirconation of alkyne **1e** afforded the organozirconium intermediate as the expected *E* isomer. Yet, transmetalation of the organozirconium intermediate to gold

unexpectedly produced a 4:1 (*E*:*Z*) mixture of diastereomers. The identity of both diastereomers in the final organogold mixture, (*E*)-**2e** and (*Z*)-**2e**, was clearly indicated from their distinctive alkenyl ¹H NMR coupling constants. We next turned our attention to probing the origin of this stereochemical scrambling. We hypothesized that alkenylgold **2e** could form a gold carbenoid intermediate which would be responsible for the *E* to *Z* isomerization (Scheme 4.2). Specifically, electron donation from Au into the alkene promotes a nucleophilic attack of the alkene onto the alkyl bromide, thereby forming the ion-paired gold carbenoid intermediate **4**. Subsequent C–C bond rotation and collapse of the ion pair affords the *Z* isomer. In related work, Fürstner and co-workers reported *Z* to *E* isomerization of an organogold compound through a carbenoid intermediate, although the organogold carbenoid in that case was formed through a different route.^{33,34} To investigate this isomerization process further, the transmetalation reaction to generate **2e** was repeated in the less polar solvent C₆D₆. We hypothesized that C₆D₆, being less polar than CD₂Cl₂, would not be as effective at stabilizing the proposed carbenoid ion pair intermediate **4** (Scheme 4.2) and therefore the isomerization pathway would be kinetically less accessible. Consistent with this hypothesis, the hydrozirconation/transmetalation reaction conducted in C₆D₆ produced only the *E* isomer of **2e**. As additional evidence for the solvent effect, stereochemically pure (*E*)-**2e** was dissolved in CD₂Cl₂, and subsequently isomerized to a 1:1 mixture of *E* and *Z* isomers in 12 h. In contrast, no isomerization of stereochemically pure (*E*)-**2e** occurred after 12 h on dissolution in C₆D₆. From these data, we concluded that the isomerization did not occur as part of the transmetalation step but rather was an independent intramolecular rearrangement reaction of organogold **2e**, consistent with the carbenoid ion pair mechanism shown in Scheme 2. The product isomer is dependent upon the orientation of the cyclopropyl group upon attack by the bromide when the σ- bond loses the ability to freely rotate.

Attempts to trap the potential carbenoid intermediate were investigated. Addition of AgSbF₆ to scavenge the bromide led to a rapid and intractable decomposition, while addition of methanol resulted in protodeauration³² without noticeable replacement of the bromine with a methoxy group. Trapping through cyclopropanation^{35,36} of styrene was also attempted but showed no evidence of the cyclopropanation product, possibly because the carbenoid lacks sufficient lifetime for intermolecular reactivity.

The reversibility of the transmetalation reaction was examined by combining organogold **2a** with zirconocene dichloride in CD₂Cl₂. Monitoring this mixture by ¹H NMR spectroscopy showed no signals corresponding to either the hydrozirconated intermediate or (IPr)AuCl, suggesting either that there is no kinetically accessible equilibrium between the hydrozirconated material and final organogold products or that the equilibrium strongly favors the organogold products thermodynamically. Carbon monoxide was added to this reaction mixture as a kinetic trap for the possible hydrozirconated intermediate; however, no trapping was observed, consistent with an inaccessible equilibrium.

In conclusion, this work presents a new approach to synthesizing stereodefined alkenylgold(I) compounds using a one-pot hydrozirconation/transmetalation method. This approach employs commercially available reagents, is complete in less than 4 h, and allows for inclusion of functional groups that are either unexplored or unavailable through currently established methods. This reaction also represents an early demonstration of a transmetalation from zirconium to gold. Examination of a product isomerization process suggests the possibility of a gold carbenoid species as a viable intermediate. This newly established method provides expanded access to alkenylgold(I) substrates for stoichiometric studies on the electronic and steric effects and the stereochemical behavior of this important class of proposed intermediates

in gold catalysis. In addition, this report of zirconium to gold transmetalation opens the possibility for continued research into the reactivity between zirconium and gold.

4.3 References

- (1) Arcadi, A. *Chem. Rev.* **2008**, *108*, 3266–3325.
- (2) Boorman, T. C.; Larrosa, I. *Chem. Soc. Rev.* **2011**, *40*, 1910–1925.
- (3) Lu, P.; Boorman, T. C.; Slawin, A. M. Z.; Larrosa, I. *J. Am. Chem. Soc.* **2010**, *132*, 5580–5581.
- (4) Hashmi, A. S. K. *Chem. Rev.* **2007**, *107*, 3180–3211.
- (5) Hirner, J. J.; Shi, Y.; Blum, S. A. *Acc. Chem. Res.* **2011**, *44*, 603–613.
- (6) Panda, B.; Sarkar, T. K. *Chem. Commun.* **2010**, *46*, 3131–3133.
- (7) Lauterbach, T.; Livendahl, M.; Rosellón, A.; Espinet, P.; Echavarren, A. M. *Org. Lett.* **2010**, *12*, 3006–3009.
- (8) Shi, Y.; Roth, K. E.; Ramgren, S. D.; Blum, S. A. *J. Am. Chem. Soc.* **2009**, *131*, 18022–18023.
- (9) Hashmi, A. S. K.; Ramamurthi, T. D.; Rominger, F. *Adv. Synth. Catal.* **2010**, *352*, 971–975.
- (10) Döpp, R.; Löthschütz, C.; Wurm, T.; Pernpointner, M.; Keller, S.; Rominger, F.; Hashmi, A. S. K. *Organometallics* **2011**, *30*, 5894–5903.
- (11) Liu, L.-P.; Hammond, G. B. *Chem. Soc. Rev.* **2012**, *41*, 3129–3139.
- (12) Liu, L.-P.; Xu, B.; Mashuta, M. S.; Hammond, G. B. *J. Am. Chem. Soc.* **2008**, *130*, 17642–17643.
- (13) Weber, D.; Tarselli, M. A.; Gagné, M. R. *Angew. Chem., Int. Ed.* **2009**, *48*, 5733–5736.

- (14) Hashmi, A. S. K.; Lothschütz, C.; Döpp, R.; Rudolph, M.; Ramamurthi, T. D.; Rominger, F. *Angew. Chem., Int. Ed.* **2009**, *48*, 8243–8246.
- (15) LaLonde, R. L.; Brenzovich, W. E., Jr.; Benitez, D.; Tkatchouk, E.; Kelley, K.; Goddard, W. A., III.; Toste, F. D. *Chem Sci.* **2010**, *1*, 226–233.
- (16) Parish, R. V. *Gold Bull.* **1997**, *30*, 3–12.
- (17) Komiya, S.; Shibue, A.; Ozaki, S. *J. Organomet. Chem.* **1987**, *319*, C31–34.
- (18) Hashmi, A. S. K.; Schuster, A. M.; Rominger, F. *Angew. Chem., Int. Ed.* **2009**, *48*, 8247–8249.
- (19) Peña-López, M.; Ayán-Varela, M.; Sarandeses, L. A.; Sestelo, J. P. *Chem. Eur. J.* **2010**, *16*, 9905–9909.
- (20) Partyka, D. V.; Zeller, M.; Hunter, A. D.; Gray, T. G. *Angew. Chem.* **2006**, *118*, 8368–8371.
- (21) Gao, L.; Peay, M. A.; Partyka, D. V.; Updegraff, J. B.; Teets, T. S.; Esswein, A. J.; Zeller, M.; Hunter, A. D.; Gray, T. G. *Organometallics* **2009**, 5669–5681.
- (22) Hashmi, A. S. K.; Schuster, A. M.; Gaillard, S.; Cavallo, L.; Poater, A.; Nolan, S. P. *Organometallics* **2011**, *30*, 6328–6337.
- (23) Hashmi, A. S. K.; Braun, I.; Rudolph, M.; Rominger, F. *Organometallics* **2012**, *31*, 644–661.
- (24) Shi, Y.; Ramgren, S. D.; Blum, S. A. *Organometallics* **2009**, *28*, 1275–1277.
- (25) Garst, J. F.; Soriaga, M. P. *Coord. Chem. Rev.* **2004**, *248*, 623–652.
- (26) Wipf, P.; Jahn, H. *Tetrahedron* **1996**, *52*, 12853–12910.
- (27) Wipf, P.; Kendall, C. *Top. Organomet. Chem.* **2005**, *8*, 1–25.
- (28) Endo, J.; Koga, N.; Morokuma, K. *Organometallics* **1993**, *12*, 2777–2787.

- (29) Chino, M.; Matsumoto, T.; Suzuki, K. *Synlett* **1994**, 359–363.
- (30) Wipf, P.; Takahashi, H.; Zhuang, N. *Pure Appl. Chem.* **1998**, *70*, 1077–1082.
- (31) For an example of transmetalation from organogold to zirconium, see: Chuchuryukin, A. V.; Huang, R.; Lutz, M.; Chadwick, J. C.; Spek, A. L.; van Koten, G. *Organometallics* **2011**, *30*, 2819–2830.
- (32) Roth, K. E.; Blum, S. A. *Organometallics* **2010**, *29*, 1712–1716.
- (33) Seidel, G.; Mynott, R.; Fürstner, A. *Angew. Chem., Int. Ed.* **2009**, *48*, 2510–2513.
- (34) Gold carbenoids have been proposed as intermediates in gold catalyzed reactions. For examples, see: (a) Shapiro, N.; Toste, F. *Synlett* **2010**, *5*, 675–691. (b) Nieto-Oberhuber, C.; López, S.; Jiménez-Núñez, E.; Echavarren, E. M. *Chem. Eur. J.* **2006**, *12*, 5916–5923. (c) Hashmi, A. S. K. *Angew. Chem., Int. Ed.* **2008**, *47*, 6754–6756.
- (35) Fedorov, A.; Chen, P. *Organometallics* **2009**, *28*, 1278–1281.
- (36) Fedorov, A.; Batiste, B.; Bach, A.; Birney, D. M.; Chen, P. *J. Am. Chem. Soc.* **2011**, *133*, 12162–12171.

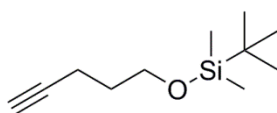
4.4 Experimental Procedures

I. General Methods

All chemicals were used as received from commercial suppliers unless otherwise noted. 1,3-bis(2,6-diisopropylphenyl)imidazol-2-ylidene gold(I) chloride was purchased from Strem Chemical Co. All other purchased reagents (alkynes **1a**, **1d-1k**) were acquired from Sigma-Aldrich. 1-Hexyne (**1a**) and 1-octene (**1i**) were purified via distillation prior to use. Diethyl ether and hexane were purified by passage through an alumina column under argon pressure on a

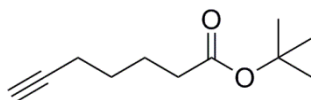
push-still solvent system. Dichloromethane-*d*2 and benzene-*d*6 were dried over CaH₂, degassed using three freeze-pump-thaw cycles, and vacuum transferred prior to use in reactions. All reactions were run in a nitrogen atmosphere glovebox unless otherwise specified. Purification of organogold products was accomplished using oven-dried Acros 50–200 μm basic aluminum oxide (activity I). This oven drying step was found to be critical for successful product isolation. Small volumes of alumina were dried in scintillation vials for a minimum of 12 hours at 140 °C to ensure the entire volume of alumina was completely dried. All proton and carbon NMR spectra were recorded using either a Bruker DRX-500 spectrometer equipped with a cryoprobe, or a Bruker AVANCE600 spectrometer. Chemical shifts are reported in parts per million. NMR spectra are calibrated to residual protiated solvent signals ($\delta = 5.32$ ppm for CD₂Cl₂, $\delta = 7.27$ ppm for CDCl₃, and $\delta = 7.12$ ppm for C₆D₆ for ¹H NMR and $\delta = 54.00$ ppm for CD₂Cl₂ for ¹³C NMR). High resolution mass spectrometry data were obtained at The University of California, Irvine. Elemental Analyses were provided by Elemental Analysis, Inc.

II. Synthetic Procedures



1b

1b. Silyl ether **1b** was prepared according to a literature procedure.¹ The product was obtained as a colorless oil (0.52 g, 23% yield). ¹H NMR (CDCl₃, 500 MHz): δ 0.07 (s, 6H), 0.90 (s, 9H), 1.74 (m, 2H), 1.93 (s, 1H), 2.28 (m, 2H), 3.70 (t, $J = 6.0$ Hz, 2H). This spectrum is in agreement with previously reported spectra.¹



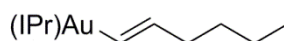
1c

1c. Ester **1c** was prepared according to a literature procedure.² The product was obtained as a colorless oil (10.5 mg, 2% yield). The low yield resulted from hydrolysis of the product on silica gel, which was not reported in the original procedure. Additional purification was required, which consisted of running the product through a basic alumina plug to separate out material that had hydrolyzed on the initial silica gel column. ¹H NMR (CD₂Cl₂, 600 MHz): δ 1.43 (s, 9H), 1.54 (m, J = 7.3, 9.2 Hz, 2H), 1.66 (m, J = 7.7, 6.3 Hz, 2H), 1.98 (t, J = 2.6 Hz, 1H), 2.20 (m, 4H). This spectrum is in agreement with previously reported spectra.²

General Reaction Procedure

In a N₂ filled glovebox, Schwartz's reagent (35.2 mg, 0.136 mmol, 1.36 equiv) was weighed into a dram vial. Alkyne **1** (0.100 mmol, 1.00 equiv) was weighed into another dram vial. To the alkyne was added 0.30 mL of CD₂Cl₂, and the resulting solution was added to the vial containing the Schwartz's reagent. An additional 0.20 mL of CD₂Cl₂ was used to rinse the vial previously containing the alkyne and then added to the reaction vial. Starting materials that were liquids were measured using a gastight syringe and added directly to the vial containing Schwartz's reagent and the final volume of 0.50 mL CD₂Cl₂. An oven-dried stir bar was added to the vial, which was then capped and allowed to stir for 30 min. The resulting solution was transferred to an oven-dried J. Young tube and examined via ¹H NMR spectroscopy for

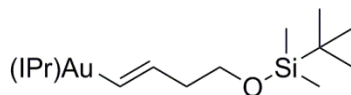
completion. Upon completion, the solution was returned to the glovebox. ((2,6-diisopropylphenyl)imidazole-2-ylidene gold(I) chloride) ((IPr)AuCl) (62.0 mg, 0.100 mmol, 1.00 equiv) was weighed into a dram vial and dissolved in 0.30 mL of CD₂Cl₂. The resulting solution was transferred to the original J. Young tube and the vial was rinsed with another 0.20 mL of CD₂Cl₂, which was also then added to the J. Young tube. The reaction was run for 3 h and monitored further for completion if necessary by ¹H NMR spectroscopy. Upon completion, the reaction was transferred to a 20 mL scintillation vial in the glovebox and concentrated in vacuo. The resulting residue was extracted using 2 mL of dry 1:1 hexanes:diethyl ether. The solution was filtered through a pipette fitted with an oven-dried glass fiber filter to remove solid zirconocene dichloride. The filtered solution was then passed through a pipette containing basic alumina (c.a. 3 cm height) with additional hexanes:diethyl ether solution (c.a. 5 mL) in order to remove any residual impurities. The filtrate was removed from the glovebox and concentrated in vacuo to yield a white solid. This solid was dried under high vacuum (<50 mTorr) overnight to obtain the final vinylgold product.



2a

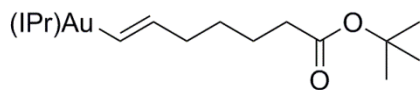
2a. 1-Hexyne (**1a**) (11.4 μ L, 0.100 mmol) was employed for the reaction, following the standard procedure. The product was isolated as a white solid (42.8 mg, 72% yield). ¹H NMR (CD₂Cl₂, 600 MHz): δ 0.79 (t, J = 6.6 Hz, 3H), 1.17 (m, 4H), 1.21 (d, J = 6.6 Hz, 12 H), 1.34 (d, J = 6.6 Hz, 12H), 1.87 (q, J = 6.6, 12.9 Hz, 2H), 2.61 (sept, J = 6.5, 10.3, 12.1 Hz, 4H), 5.21 (dt, J = 6.6, 18.6 Hz, 1H), 6.11 (d, J = 18.6 Hz, 1H), 7.13 (s, 2H), 7.32 (d, J = 7.8 Hz, 4H), 7.55 (t, J = 7.8 Hz, 2H). ¹³C NMR (CD₂Cl₂, 125 MHz): δ 14.4, 23.1, 24.1, 24.7, 29.3, 32.8, 39.0, 123.5, 124.5,

130.6, 135.3, 145.7, 146.4, 153.0, 198.8. HRMS (ESI): $[M + Na]^+$ calcd. for $C_{33}H_{47}N_2AuNa$, 691.3303; found, 691.3287. Anal. Calcd. for $C_{33}H_{47}AuN_2$: C, 59.27; H, 7.08; N, 4.19. Found: C, 58.99; H, 7.13; N, 4.13.



2b

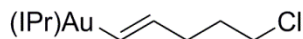
2b. Synthesized compound **1b** (19.8 mg, 0.100 mmol) was employed in this reaction, following the standard procedure. The product was isolated as a white solid (44.5 mg, 57% yield). 1H NMR (CD_2Cl_2 , 500 MHz): δ 0.84 (s, 3H), 1.21 (d, $J = 7.0$ Hz, 12H), 1.34 (d, $J = 7.0$ Hz, 12H), 1.40 (quint, $J = 7.0, 11.0$ Hz, 2H), 1.90 (q, $J = 7.5, 14.2$ Hz, 2H), 2.61 (sept, $J = 7.0, 10.5, 12.3$ Hz, 4H), 3.47 (t, $J = 6.5$ Hz, 2H), 5.20 (dt $J = 10.5, 19.5$ Hz, 1H), 6.12 (d, $J = 18.5$ Hz, 1H), 7.14 (s, 2H), 7.32 (d, $J = 7.5$ Hz, 4H), 7.53 (t, $J = 7.0$ Hz, 2H). ^{13}C NMR (CD_2Cl_2 , 125 MHz): δ 24.1, 24.7, 26.3, 29.3, 33.7, 35.2, 63.7, 123.4, 124.5, 130.6, 135.3, 144.8, 146.4, 154.3, 198.7. HRMS (ESI): $[M + Na]^+$ calcd. for $C_{38}H_{59}OSiN_2AuNa$, 807.3960; found, 807.3976. Anal. Calcd. For $C_{38}H_{59}AuN_2OSi$: C, 58.15; H, 7.58; N, 3.57. Found: C, 58.52; H, 7.87; N, 3.51.



2c

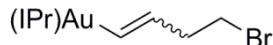
2c. Synthesized compound **1c** (7.8 mg, 0.040 mmol) was added to Schwartz's reagent (15 mg, 0.054 mmol), following the standard procedure. The complex (IPr)AuCl (26.6 mg, 0.0429 mmol) was added to the reaction. The product was isolated as a white solid (20.6 mg, 62% yield). 1H NMR (CD_2Cl_2 , 500 MHz): δ 1.21 (d, $J = 6.9$ Hz, 12H), 1.34 (d, $J = 6.9$ Hz, 12H), 1.38 (s, 9H), 1.43 (m, 2H), 1.87 (q, $J = 7.5, 6.9$ Hz, 2H), 2.08 (t, $J = 7.5$ Hz, 2H), 2.60 (sept, $J = 6.0, 11.0$,

12.0 Hz, 4H), 5.20 (dt, $J = 6.1, 18.6$ Hz, 1H), 6.12 (d, $J = 18.5$ Hz, 1H), 7.14 (s, 2H), 7.32 (d, $J = 7.8$ Hz, 4H), 7.53 (t, $J = 7.8$ Hz, 2H). ^{13}C NMR (CD_2Cl_2 , 125 MHz): δ 24.1, 24.7, 25.6, 28.4, 29.3, 30.0, 36.1, 38.8, 79.9, 123.5, 124.5, 130.6, 135.3, 145.1, 146.5, 154.3, 173.7, 198.7. HRMS (ESI): $[\text{M} + \text{Na}]^+$ calcd. for $\text{C}_{38}\text{H}_{55}\text{AuN}_2\text{O}_2$, 791.3827; found, 791.3824.



2d

2d. Alkyne **1d** (11.1 μL , 0.100 mmol) was employed in the reaction. Standard reaction conditions were followed. Product was isolated as a white solid (46.6 mg, 68% yield). ^1H NMR (CD_2Cl_2 , 500 MHz): δ 1.21 (d, $J = 6.9$ Hz, 12H), 1.34 (d, $J = 6.9$ Hz, 12H), 1.67 (m, 2H), 2.00 (q, $J = 7.2, 13.8$ Hz, 2H), 2.61 (sept, $J = 7.0, 10.0, 12.0$ Hz, 4H), 3.42 (t, $J = 7.0$ Hz, 2H), 5.17 (dt, $J = 6.2, 18.5$ Hz, 1H), 6.17 (d, $J = 18.5$ Hz, 1H), 7.14 (s, 2H), 7.32 (d, $J = 7.8$ Hz, 4H), 7.53 (t, $J = 7.8$ Hz, 2H). ^{13}C NMR (CD_2Cl_2 , 125 MHz): δ 24.1, 24.7, 29.3, 33.5, 36.1, 45.9, 123.5, 124.5, 130.6, 135.3, 143.1, 146.5, 155.7, 198.4. HRMS (ESI): $[\text{M} + \text{Na}]^+$ calcd. For $\text{C}_{32}\text{H}_{44}\text{AuN}_2\text{Cl}$, 711.2756; found, 711.2745. Anal. Calcd. for $\text{C}_{32}\text{H}_{44}\text{AuN}_2\text{Cl}$: C, 55.77; H, 6.44; N, 4.07. Found: C, 55.95; H, 6.35; N, 4.06.



2e

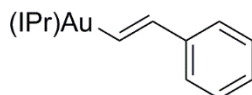
2e. Alkyne **1e** (4.7 μL , 0.050 mmol) was added to Schwartz's reagent (17.6 mg, 0.0683 mmol). Standard reaction procedure was followed. The complex (IPr)AuCl was added to the reaction (30.5 mg, 0.0492 mmol). The product was isolated as a white solid (47.5 mg, 66% yield). ^1H NMR (CD_2Cl_2 , 600 MHz): E isomer: δ 1.22 (m, 12H), 1.34 (m, 12H), 2.15 (q, $J = 7.8, 13.8$ Hz,

2H), 2.42 (q, $J = 7.8, 13.8$ Hz, 2H), 3.23 (t, $J = 7.8$ Hz, 1H), 2.66-2.55 (m, 4H), 5.17 (dt, $J = 6.6, 18.6$ Hz, 1H), 6.29 (d, $J = 18.6$ Hz, 1H), 7.14 (s, 2H), 7.33 (d, $J = 7.8$ Hz, 4H), 7.53 (t, $J = 7.8$ Hz, 2H). Z isomer: δ 1.22 (m, 12H), 1.34 (m, 12H), 2.15 (q, $J = 7.8, 13.8$ Hz, 2H), 2.66-2.55 (m, 4H), 3.00 (t, $J = 7.8$ Hz, 1H), 6.08 (quint, $J = 6.6, 9.3$ Hz, 1H), 6.34 (d, $J = 11.4$ Hz, 1H), 7.17 (s, 2H), 7.33 (d, $J = 7.8$ Hz, 4H), 7.53 (t, $J = 7.8$ Hz, 2H). ^{13}C NMR (CD_2Cl_2 , 125 MHz): δ 24.0, 24.5, 29.1, 34.3, 35.0, 41.8, 42.7, 123.4, 123.6, 124.3, 124.6, 130.5, 130.6, 131.0, 135.0, 139.7, 140.6, 146.1, 146.2, 158.6, 159.0, 197.7, 198.8. HRMS (ESI): $[\text{M} + \text{Na}]^+$ calcd. For $\text{C}_{31}\text{H}_{42}\text{N}_2\text{BrAuNa}$, 741.2095; found, 741.2069. Anal. Calcd. for $\text{C}_{31}\text{H}_{42}\text{AuN}_2\text{Br}$: C, 51.75; H, 5.88; N, 3.89. Found: C, 52.23; H, 6.05; N, 4.06.

Procedure for Examination of the Isomerization of 2e:

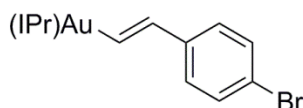
Alkyne **1e** (4.70 μL , 0.0500 mmol) was added to 0.5 mL of C_6D_6 and the resulting solution was added to Schwartz's reagent (17.6 mg, 0.0683 mmol). The reaction mixture was transferred to a J. Young tube. The reaction was monitored for completion by ^1H NMR spectroscopy. Upon completion, a solution of $(\text{IPr})\text{AuCl}$ (30.5 mg, 0.0492 mmol) in 0.5 mL of C_6D_6 was added to the reaction. The reaction was monitored for completion by ^1H NMR spectroscopy. The only product formed was the E isomer. The J Young tube was returned to the glovebox and the solution was separated equally into two scintillation vials. The two vials were concentrated in vacuo in the glovebox. The residue in the first vial was redissolved in C_6D_6 and added to a clean J Young tube. The residue in the second vial was redissolved in CD_2Cl_2 and added to another clean J Young tube. Each solution was monitored by ^1H NMR spectroscopy immediately after being redissolved and again after 12 h. After 12 h, isomerization of the

organogold was evident in the sample in CD₂Cl₂, but no appreciable change was observed for the sample in C₆D₆.



2f

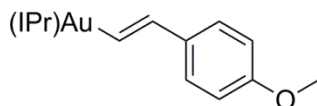
2f. Alkyne **1f** (11.0 μ L, 0.100 mmol) was employed in the reaction. The product was isolated as a white solid (53.3 mg, 77% yield). ¹H NMR (CD₂Cl₂, 600 MHz): δ 1.23 (d, J = 6.6 Hz, 12H), 1.38 (d, J = 7.2 Hz, 12H), 2.65 (sept, J = 6.0, 8.5, 10.3 Hz, 4H), 6.24 (d, J = 19.2 Hz, 1H), 6.96 (m, 1H), 7.12 (m, 4H), 7.17 (s, 2H), 7.29 (d, J = 19.2 Hz, 1H), 7.34 (d, J = 7.8 Hz, 4H), 7.54 (t, J = 7.8 Hz, 2H). ¹³C NMR (CD₂Cl₂, 125 MHz): δ 24.2, 24.7, 29.3, 123.6, 124.5, 125.4, 125.6, 128.5, 130.7, 135.2, 141.8, 143.1, 146.5, 158.9. HRMS (ESI): [M + Na]⁺ calcd. for C₃₅H₄₃AuN₂Na, 711.2990; found, 711.2971. Anal. Calcd. for C₃₅H₄₃AuN₂: C, 61.04; H, 7.08; N, 4.19. Found: C, 58.99; H, 7.13; N, 4.13.



2g

2g. Alkyne **1g** (18.1 mg, 0.100 mmol) was employed in the reaction. The product was isolated as a white solid (47.3 mg, 77% yield). ¹H NMR (CD₂Cl₂, 500 MHz): δ 1.23 (d, J = 7.0 Hz, 12H), 1.37 (d, J = 7.0 Hz, 12H), 2.64 (sept, J = 7.0, 10.5, 12.3 Hz, 4H), 6.19 (d, J = 19.5 Hz, 1H), 7.03 (d, J = 8.5 Hz, 2H), 7.18 (s, 2H), 7.24 (d, J = 8.5 Hz, 2H), 7.31 (d, J = 19.5 Hz, 1H), 7.34 (d, J = 7.5 Hz, 2H), 7.54 (t, J = 8.0 Hz, 2H). ¹³C NMR (CD₂Cl₂, 125 MHz): δ 24.2, 24.8, 29.3, 118.9, 123.6, 124.5, 127.1, 130.8, 131.5, 135.2, 140.8, 141.7, 246.5, 160.6, 197.4. HRMS (ESI): [M +

Na]⁺ calcd. for C₃₅H₄₂N₂BrAuNa, 789.2095; found, 789.2092. Anal. Calcd. for C₃₅H₄₂AuN₂Br: C, 54.77; H, 5.52; N, 3.65. Found: C, 54.83; H, 5.43; N, 3.49.



2h

2h. Alkyne **1h** (13.0 μ L, 0.100 mmol) was employed in the reaction. Product was isolated as a white solid (41.5 mg, 65% yield). ¹H NMR (CD₂Cl₂, 600 MHz): δ 1.23 (d, J = 7.0 Hz, 12H), 1.38 (d, J = 7.0 Hz, 12H), 2.65 (sept, J = 6.5, 10.8, 11.9 Hz, 4H), 3.71 (s, 3H), 6.18 (d, J = 19.2 Hz, 1H), 6.68 (d, J = 8.4 Hz, 2H), 7.06 (d, J = 8.4 Hz, 2H), 7.14 (d, J = 19.0 Hz, 1H), 7.17 (s, 2H), 7.34 (d, J = 7.8 Hz, 4H), 7.54 (t, J = 7.8 Hz, 2H). ¹³C NMR (CD₂Cl₂, 125 MHz): 24.2, 24.8, 29.3, 55.6, 113.9, 123.6, 124.5, 126.4, 130.7, 135.1, 135.2, 142.4, 146.5, 156.1, 158.1, 197.9. HRMS (ESI): [M + Na]⁺ calcd. for C₃₆H₄₅ON₂AuNa, 741.3095; found, 741.3088. Anal. Calcd. for C₃₆H₄₄AuN₂Cl: C, 55.77; H, 6.44; N, 4.07. Found: C, 55.95; H, 6.35; N, 4.06.

Procedure for Transmetalation Reversibility Test:

In the glovebox, **2a** (69.7 mg, 0.104 mmol) was added to a vial with 0.5 mL of CD₂Cl₂. The resulting solution was transferred to a vial containing zirconocene dichloride (39.7 mg, 0.136 mmol). This solution was then transferred to a J. Young tube. The solution was degassed via three freeze-pump-thaw cycles and placed under 1 atm of CO. The presence of CO was intended to trap any of the reverse transmetalated product formed, as earlier experiments had shown that the product of CO insertion into the hydrozirconated starting materials would not transmetalate with (IPr)AuCl. The reaction was monitored by ¹H NMR spectroscopy over 3 d.

After 3 d, only the starting organogold **2a** and its protodeaurated equivalent, 1-hexene, were observed. The lack of any observable signals corresponding to the hydrozirconated material related to **2a** or products of CO insertion suggests there is no significant pathway by which the transmetalation of the hydrozirconated alkynes to the final organogold products is reversible.

Procedure for Attempted AgSbF₄ Carbenoid Trapping Experiment

To a solution of 34.7 mg (0.0480 mmol) of **2e** in 0.5 mL of CD₂Cl₂ was added 16.5 mg (1.00 equiv) of AgSbF₆ in a glovebox. The solution was stirred for 30 min. The solution was then filtered through a pipette fitted with a glass fiber filter to remove any precipitate (anticipated to be AgBr). The filtrate was transferred to an NMR tube. Extensive decomposition was observed with no desired carbenoid product identified.

Procedure for Attempted Methanol Carbenoid Trapping Experiment

To a solution of 5.0 mg (0.0070 mmol) of **2e** in 0.5 mL of CD₂Cl₂ was added 1.7 μ L (0.042 mmol, 6 equiv) of methanol. The solution was transferred to an NMR tube and monitored for signs of reaction at 0.2, 2, 4, 5, and 24 h. Protodeauration to yield the organic bromide was faster than any potential methoxy incorporation, and no methoxy incorporation was identified.

Procedure for Attempted Styrene Carbenoid Trapping Experiment

To 5.0 mg (0.0070 mmol) of **2e** was added a solution of 2.2 mg (0.021 mmol, 3 equiv) of styrene in 0.5 mL of CD₂Cl₂. The solution was transferred to an NMR tube and monitored for signs of reaction at 0.2, 2, 4, 5, and 24 h. No cyclopropanation of styrene was observed.

III. NMR Spectra of all Isolated Compounds

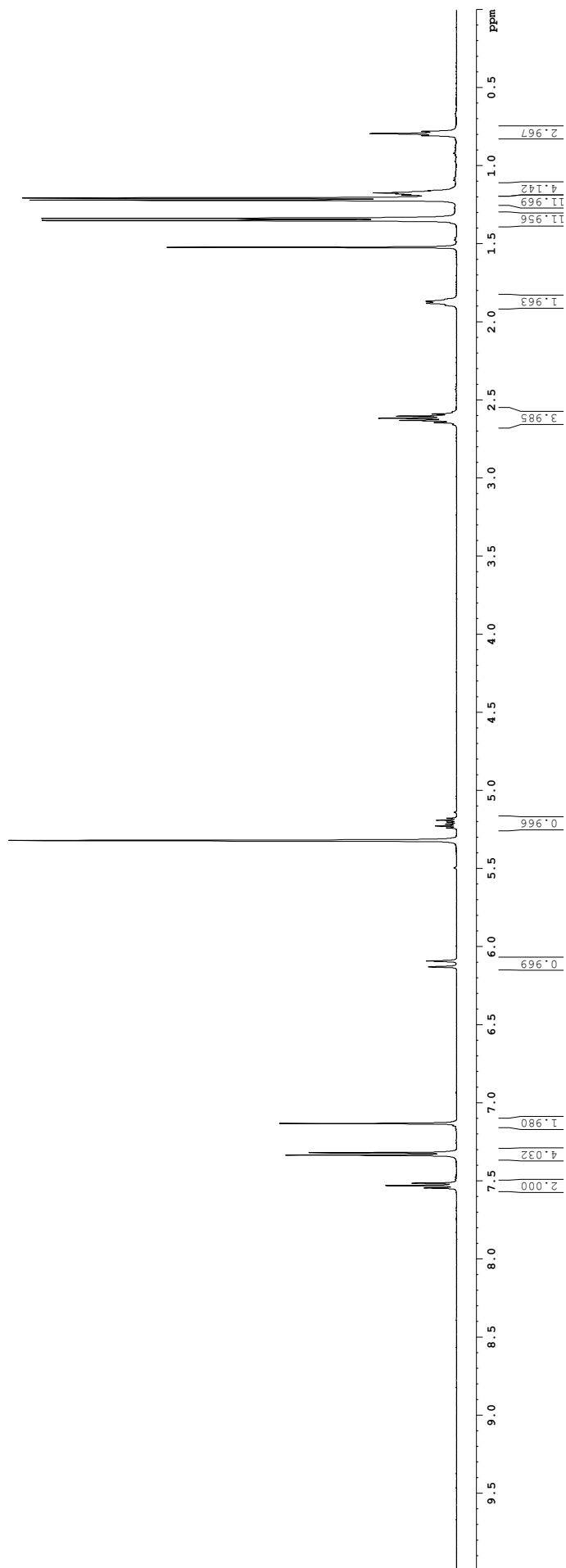
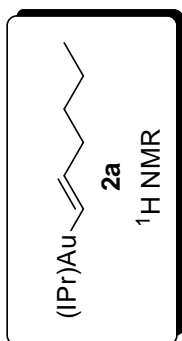
0.779
0.793
0.806
1.158
1.172
1.179
1.187
1.206
1.219
1.336
1.350
1.521
1.866
1.880

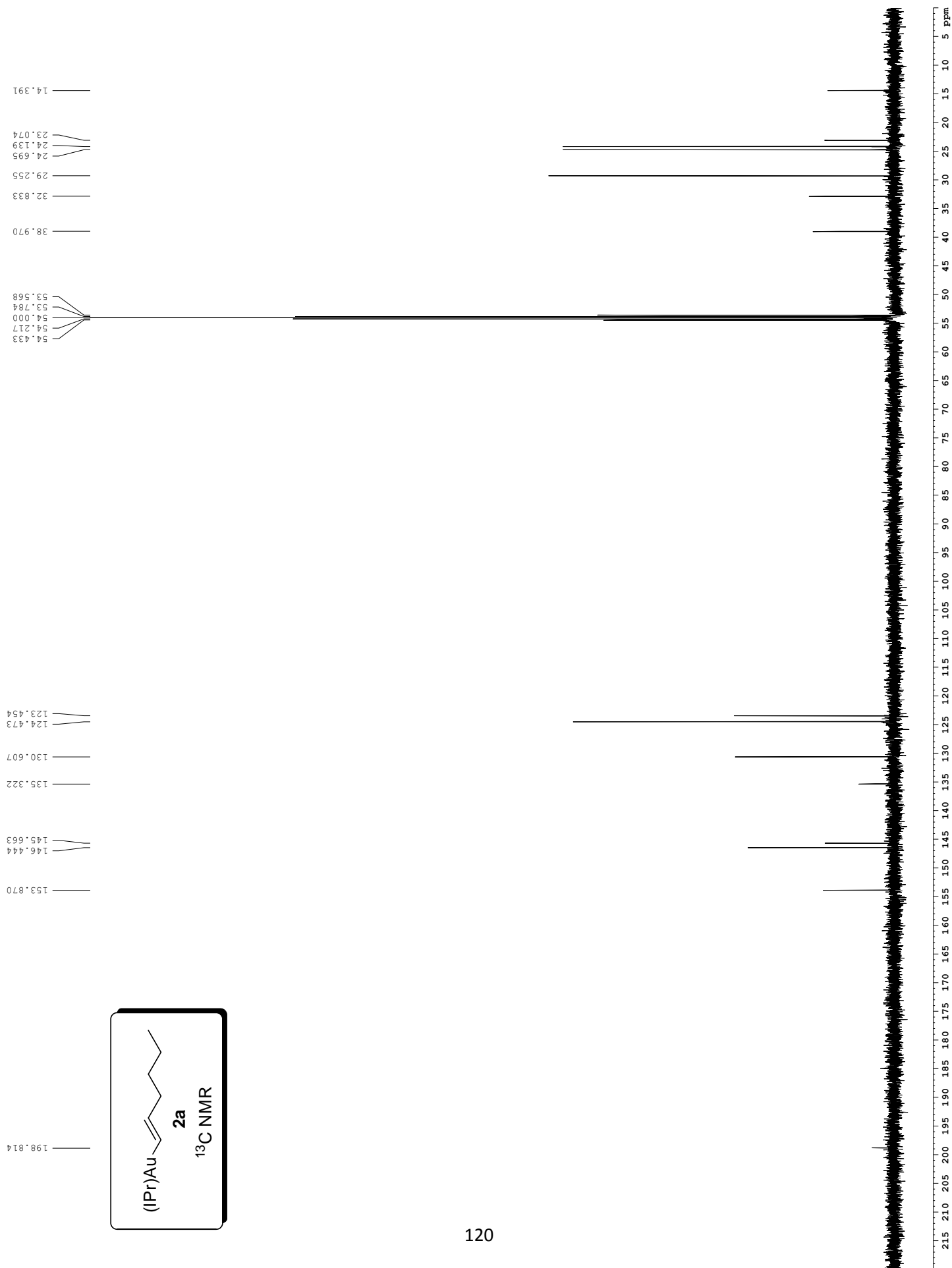
2.644
2.630
2.616
2.602
2.588

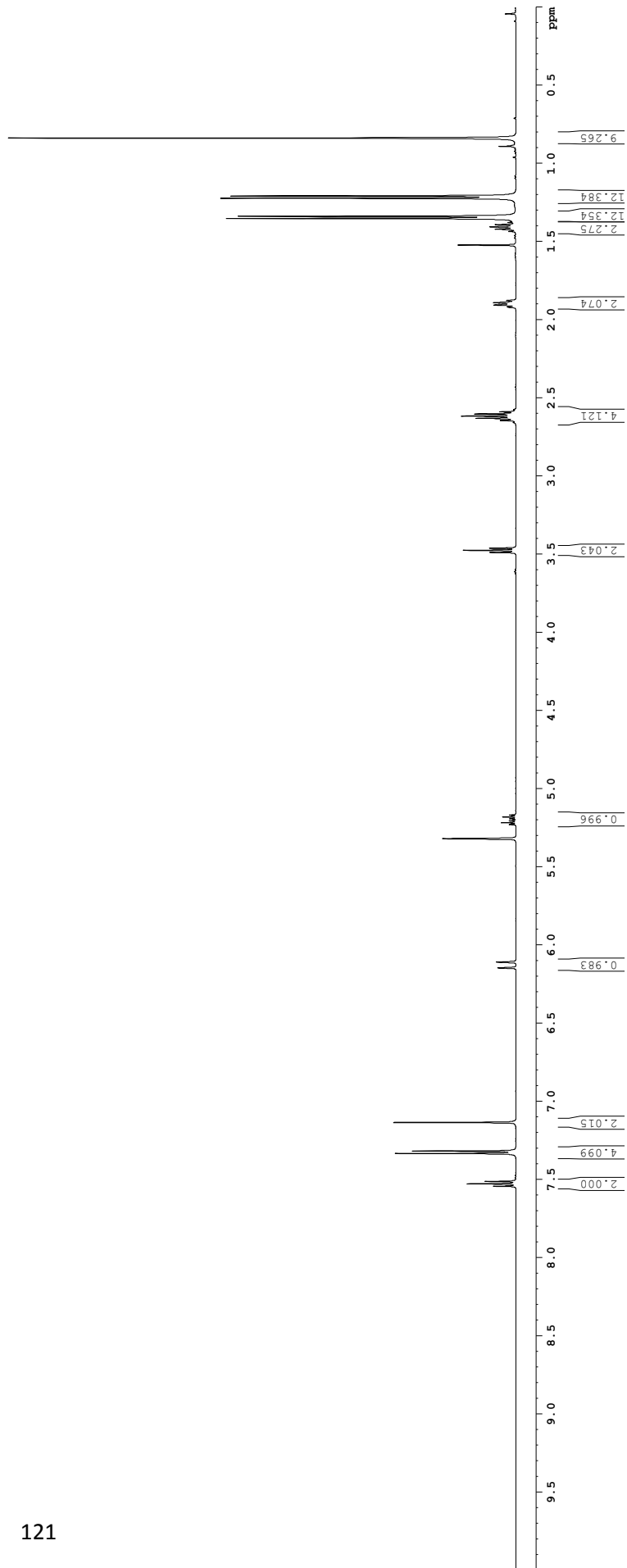
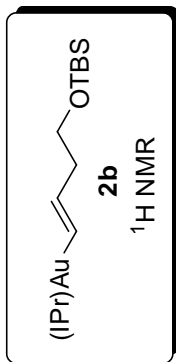
5.190
5.220
5.227

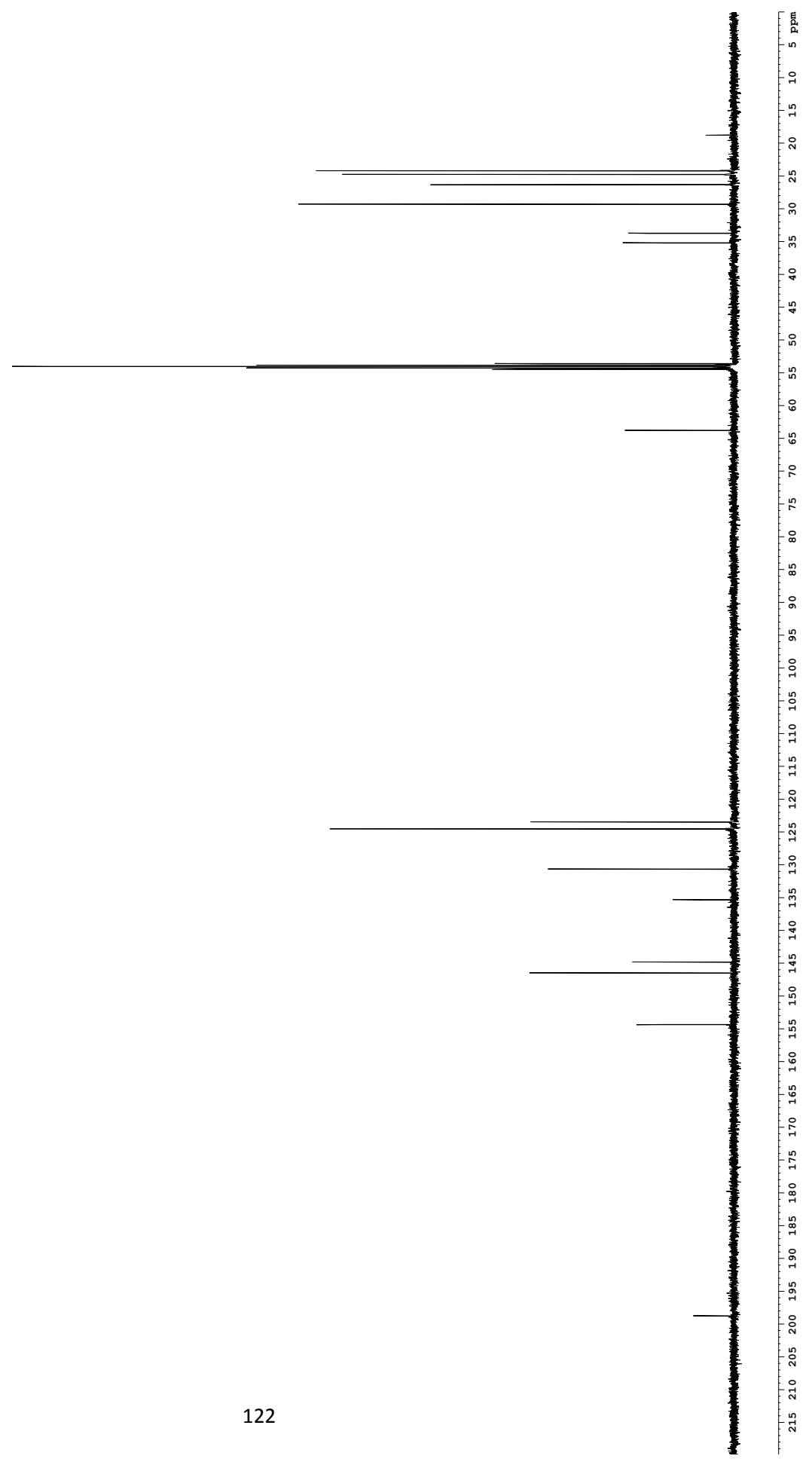
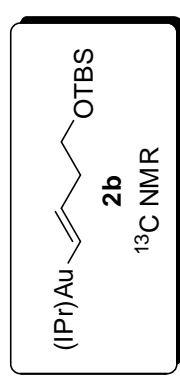
6.092
6.129

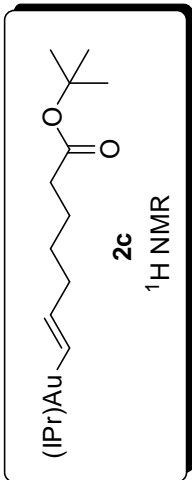
7.132
7.319
7.335
7.515
7.530
7.546











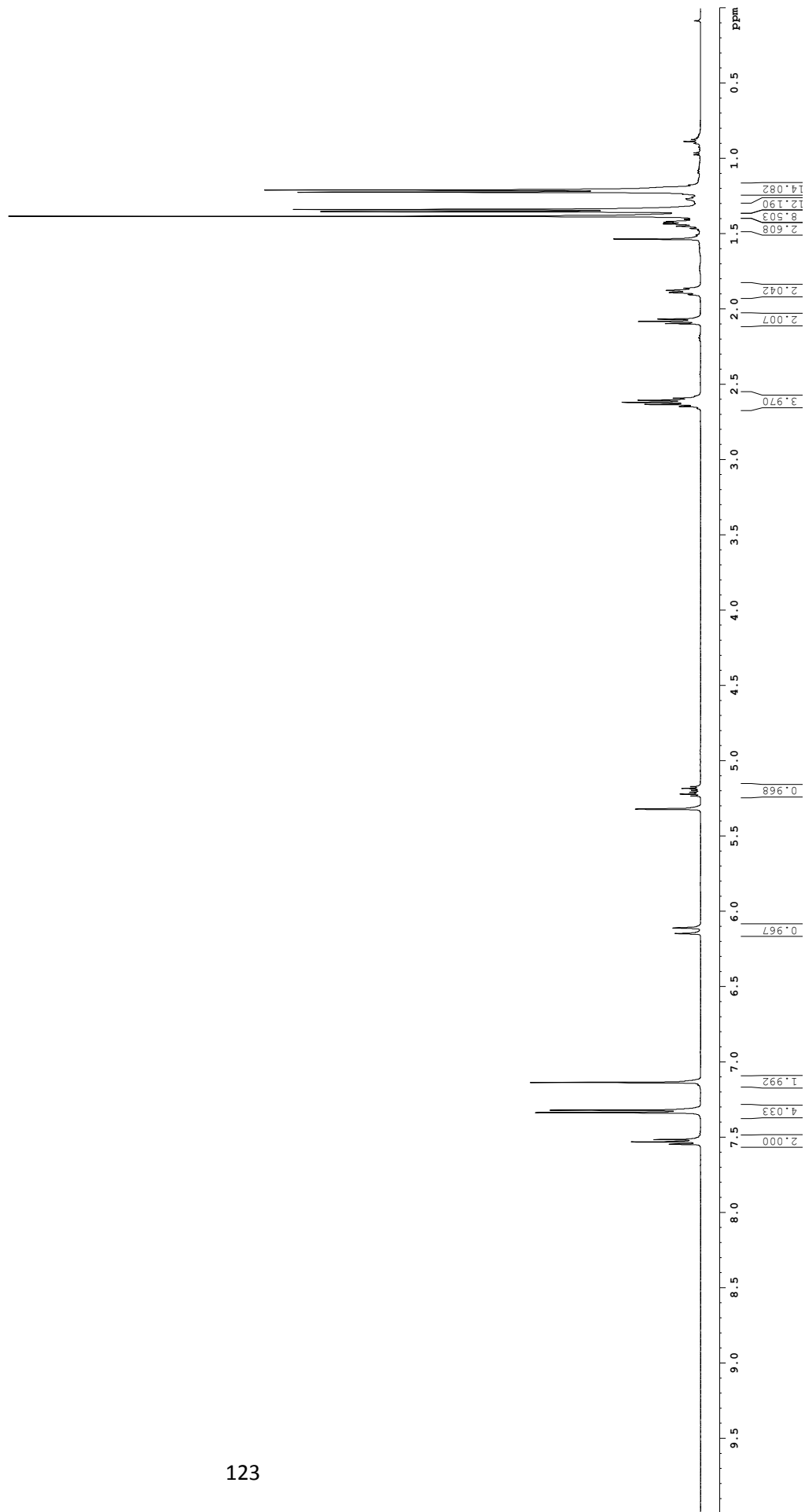
2.096
 2.081
 2.066
 1.890
 1.875
 1.534
 1.449
 1.433
 1.424
 1.418
 1.383
 1.352
 1.338
 1.222
 1.209

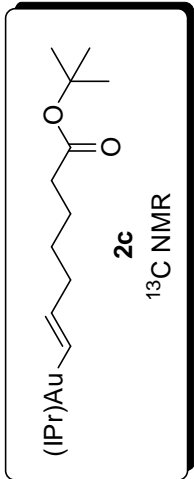
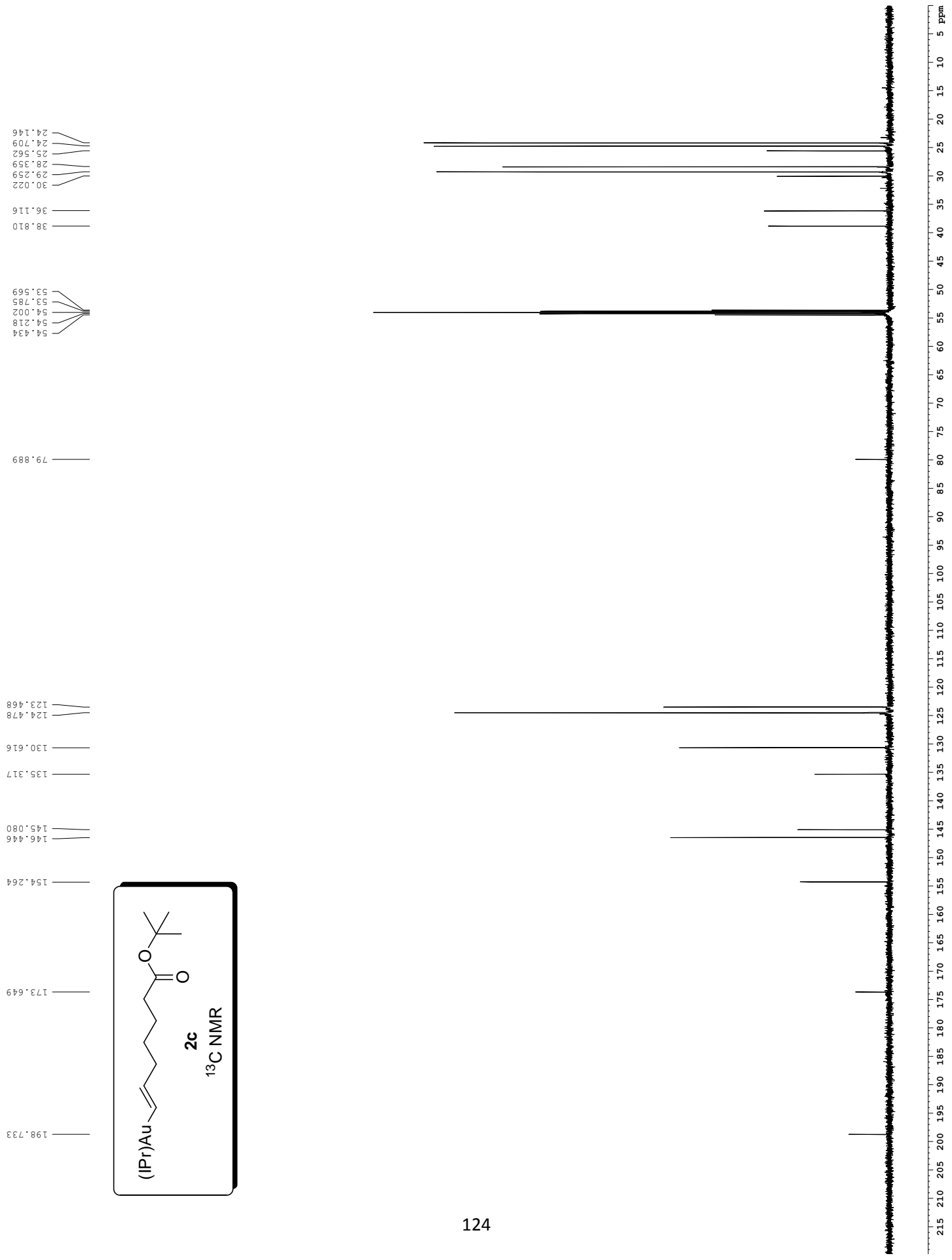
2.632
 2.619
 2.605
 2.591

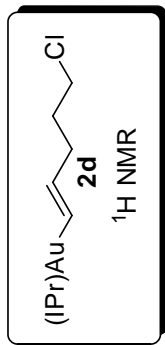
5.222
 5.220
 5.218

6.147
 6.110

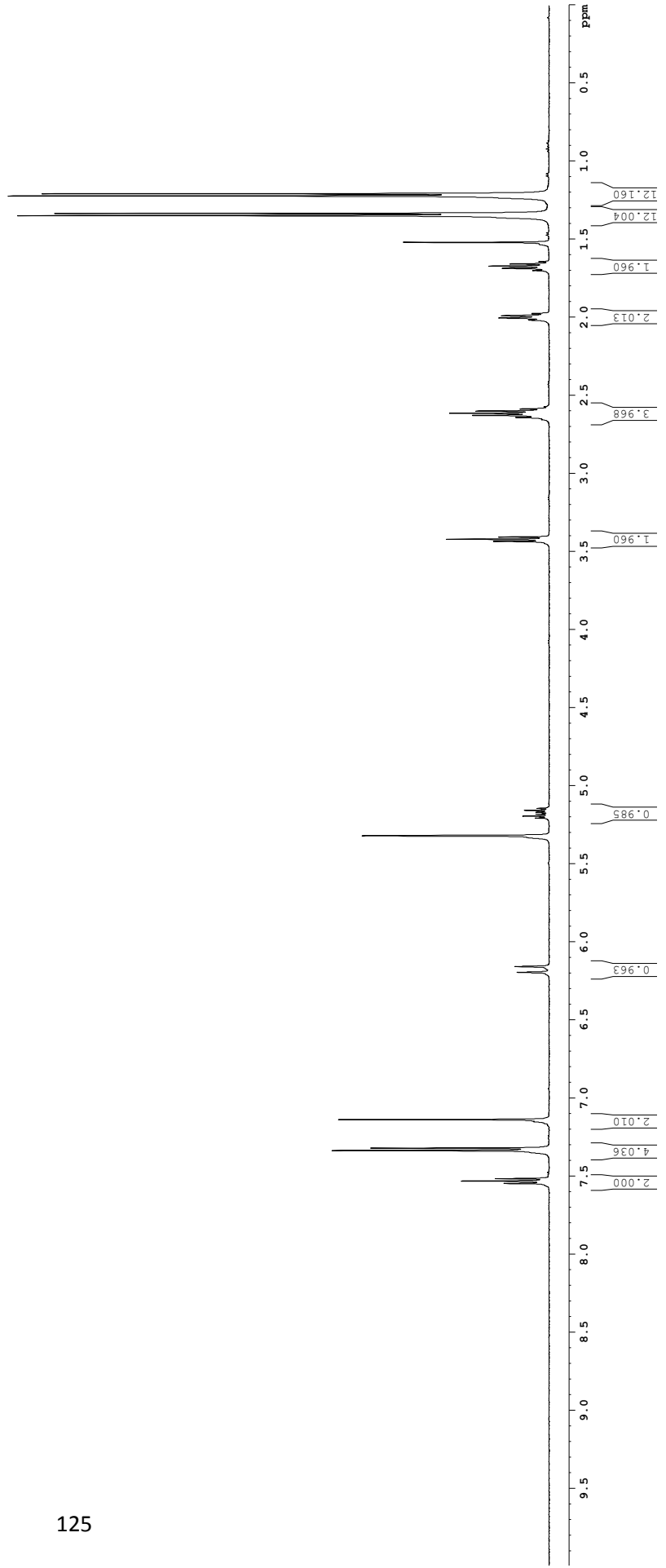
7.547
 7.531
 7.516
 7.337
 7.321
 7.136

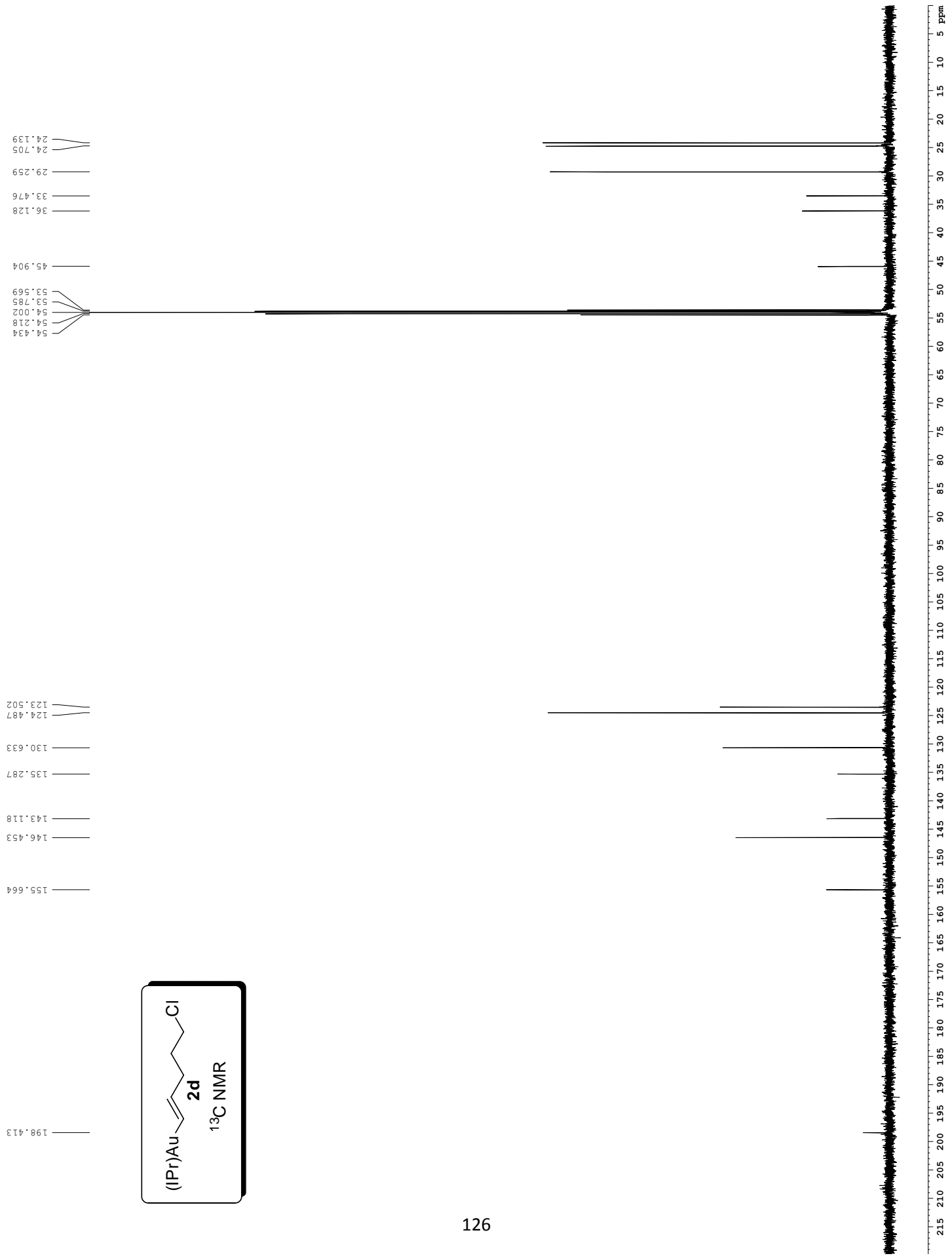


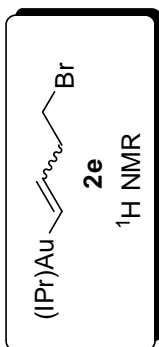




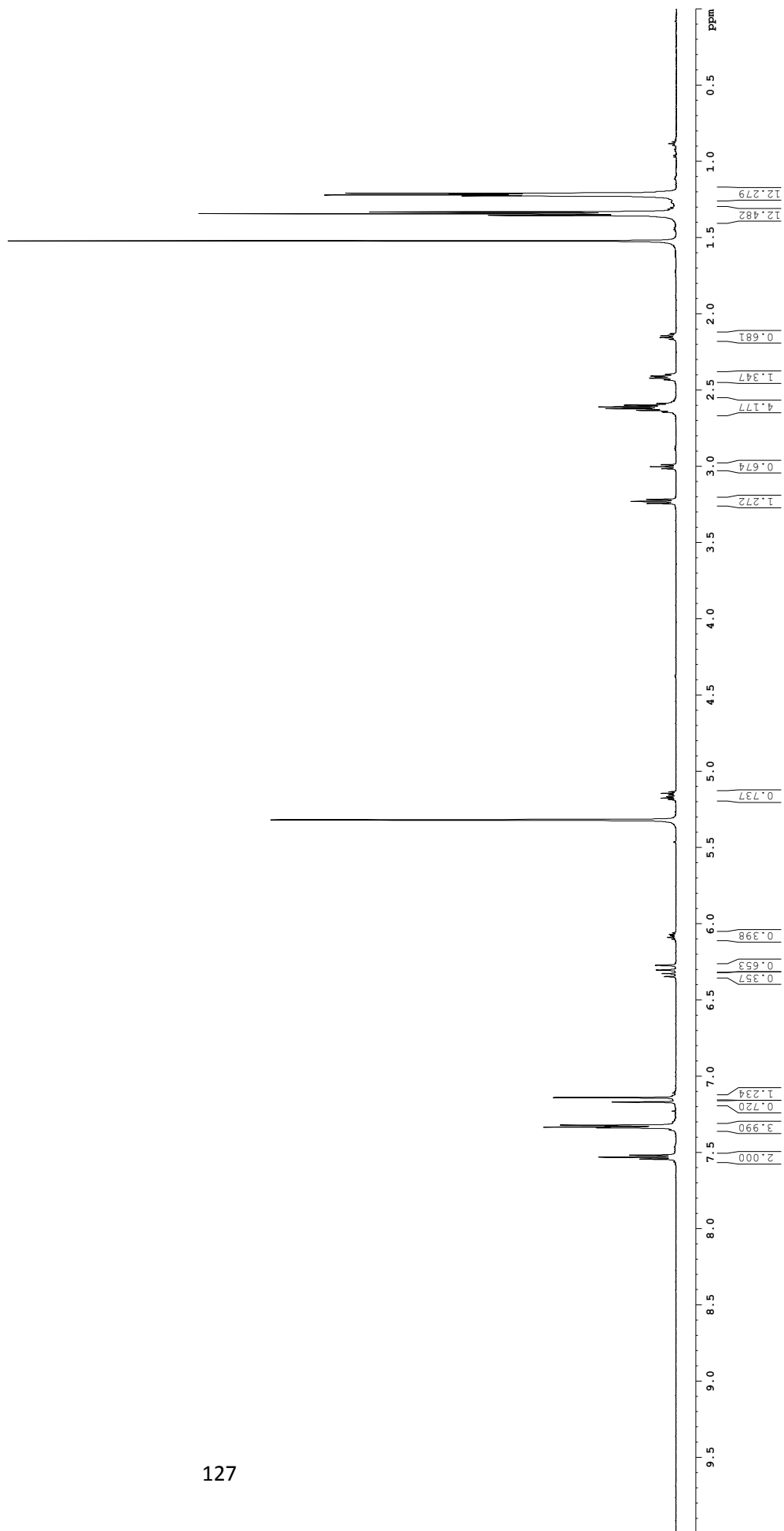
- 7.548
- 7.532
- 7.516
- 7.337
- 7.321
- 7.138
- 6.158
- 5.320
- 5.194
- 5.157
- 3.435
- 3.421
- 3.407
- 2.641
- 2.628
- 2.614
- 2.600
- 2.587
- 2.017
- 2.003
- 1.990
- 1.686
- 1.671
- 1.657
- 1.520
- 1.348
- 1.334
- 1.222
- 1.208







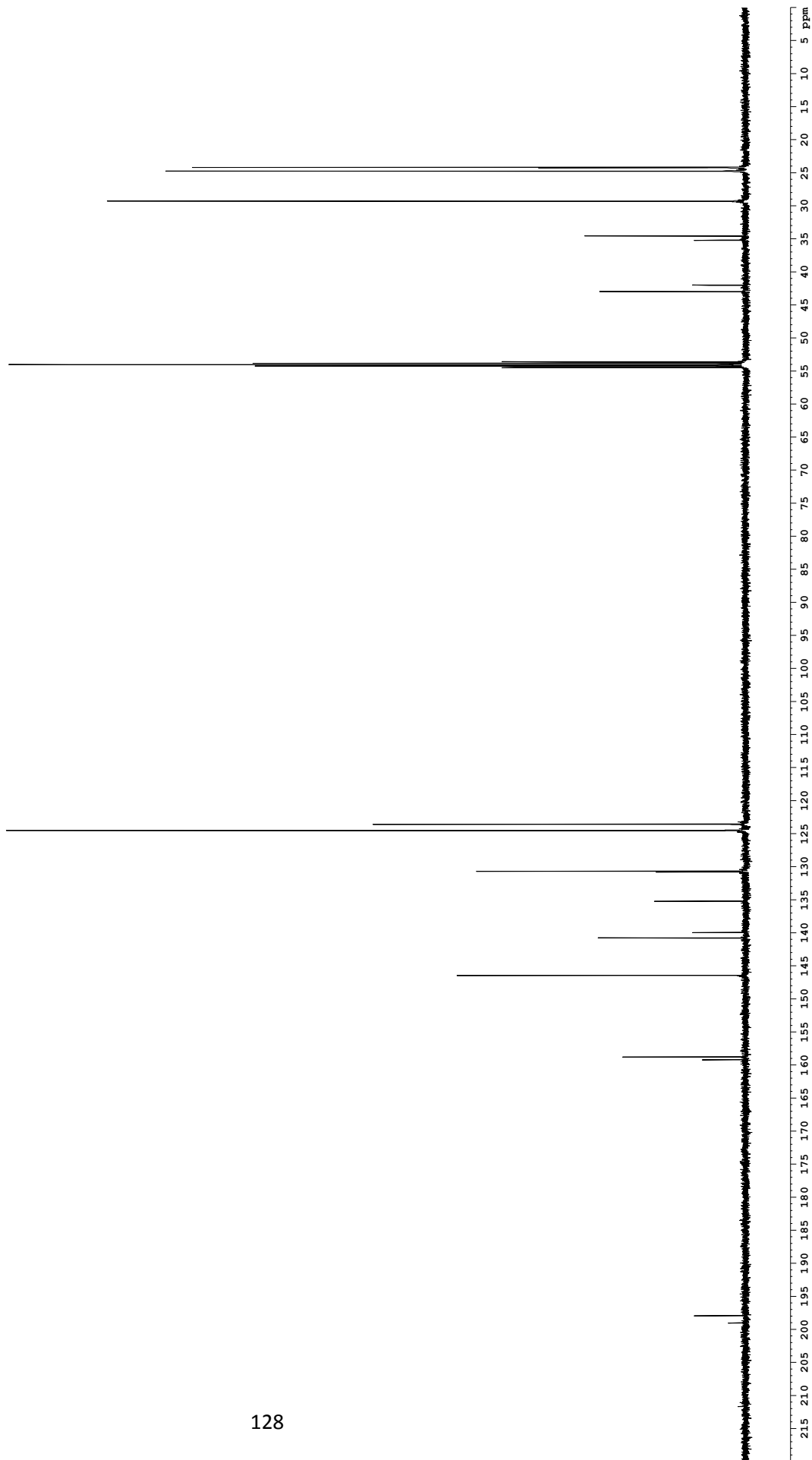
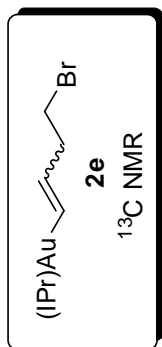
- 7.545
- 7.532
- 7.519
- 7.340
- 7.336
- 7.327
- 7.323
- 7.171
- 7.142
- 6.348
- 6.329
- 6.305
- 6.274
- 6.091
- 5.320
- 5.178
- 5.167
- 5.147
- 3.245
- 3.232
- 3.218
- 3.017
- 3.004
- 2.991
- 2.645
- 2.634
- 2.623
- 2.612
- 2.600
- 2.589
- 2.435
- 2.422
- 2.410
- 2.398
- 2.156
- 2.144
- 1.522
- 1.355
- 1.344
- 1.333
- 1.227
- 1.221
- 1.216
- 1.210

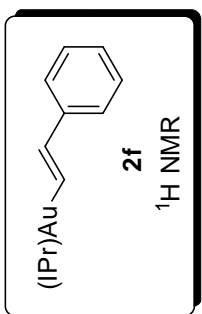


54.433
54.217
54.000
53.784
53.568
42.945
41.971
35.167
34.523
29.288
29.262
24.759
24.716
24.212
24.144

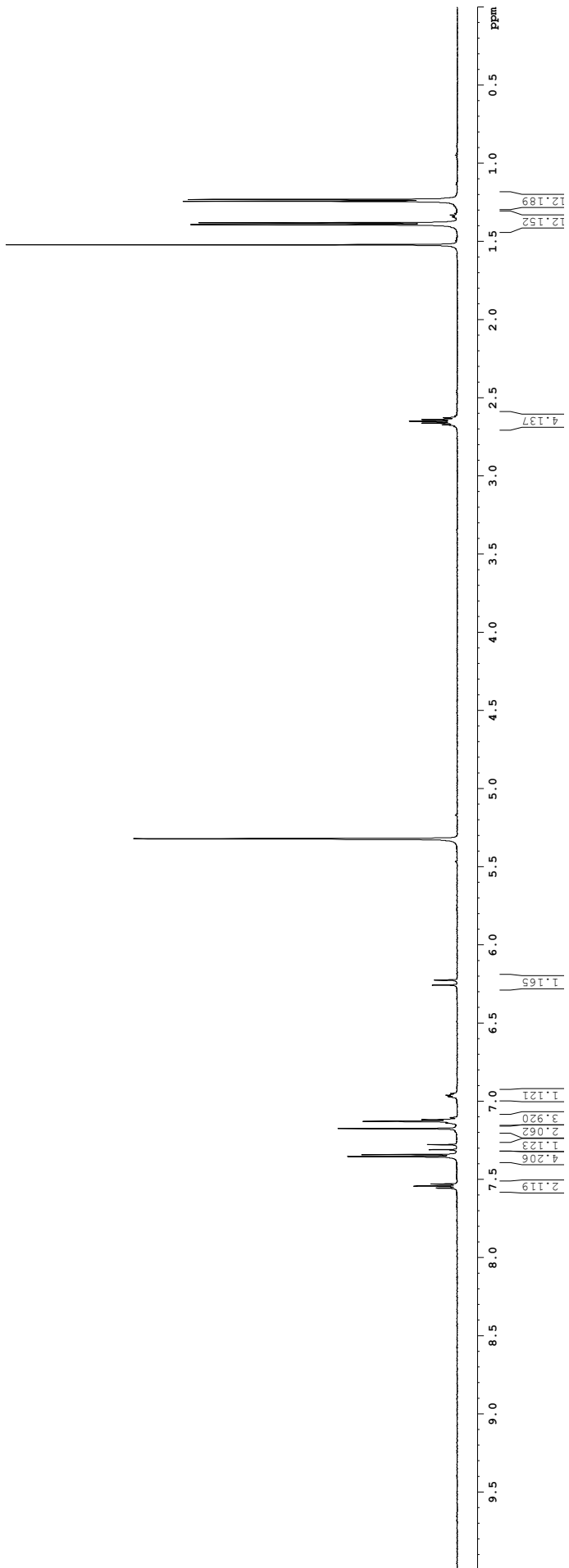
159.204
158.792
146.439
140.772
139.945
135.225
135.188
130.792
130.674
124.505
123.561

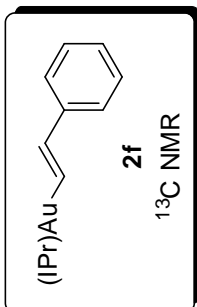
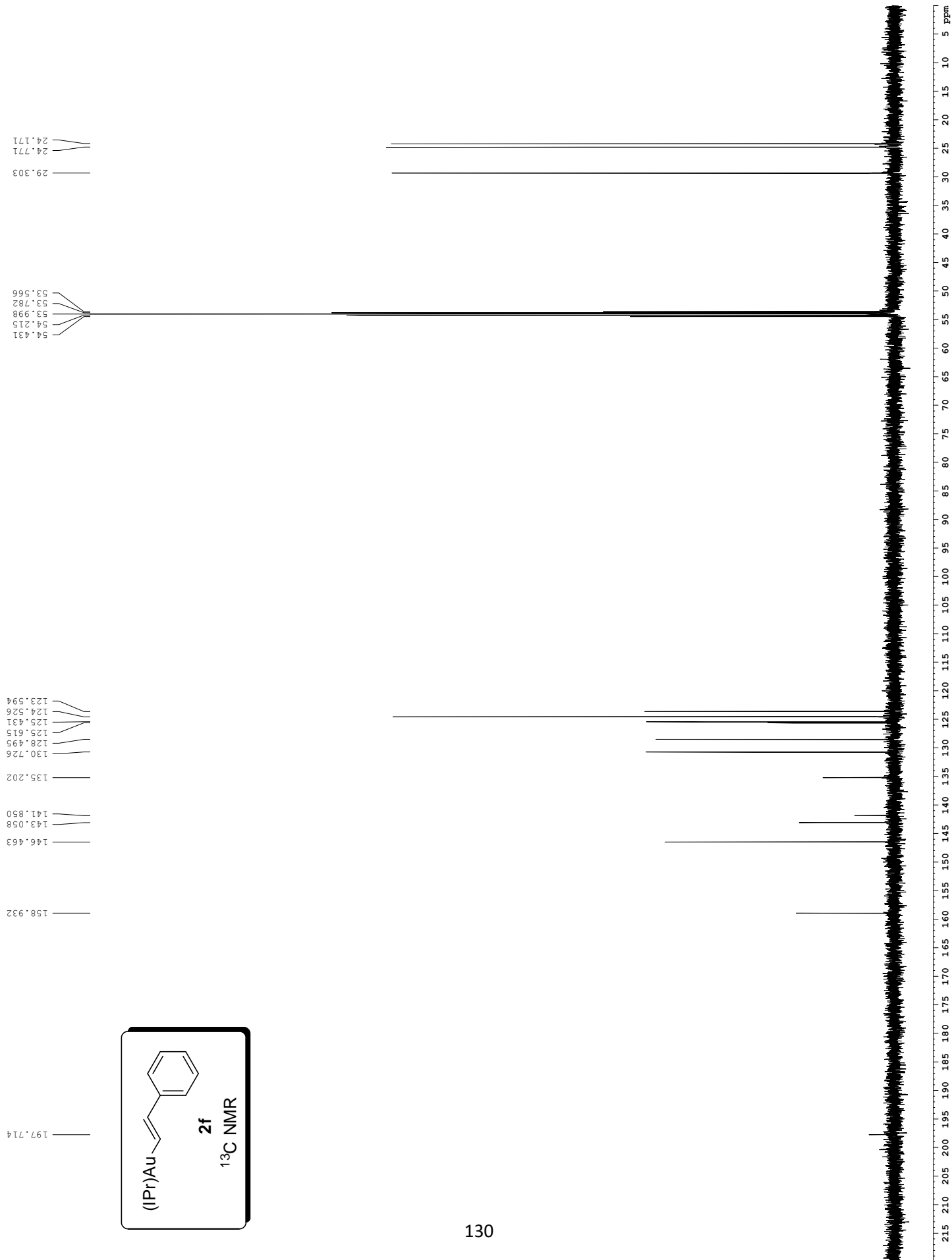
199.023
197.933

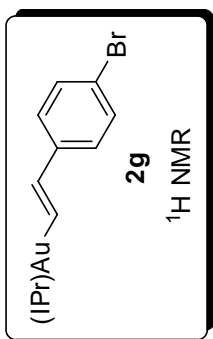




7.555
7.542
7.529
7.354
7.341
7.309
7.277
7.174
7.139
7.128
7.125
7.117
7.103
6.975
6.971
6.965
6.961
6.957
6.950
6.224
5.322
5.320
5.318
2.672
2.661
2.649
2.638
2.626
1.519
1.391
1.379
1.330
1.241
1.230







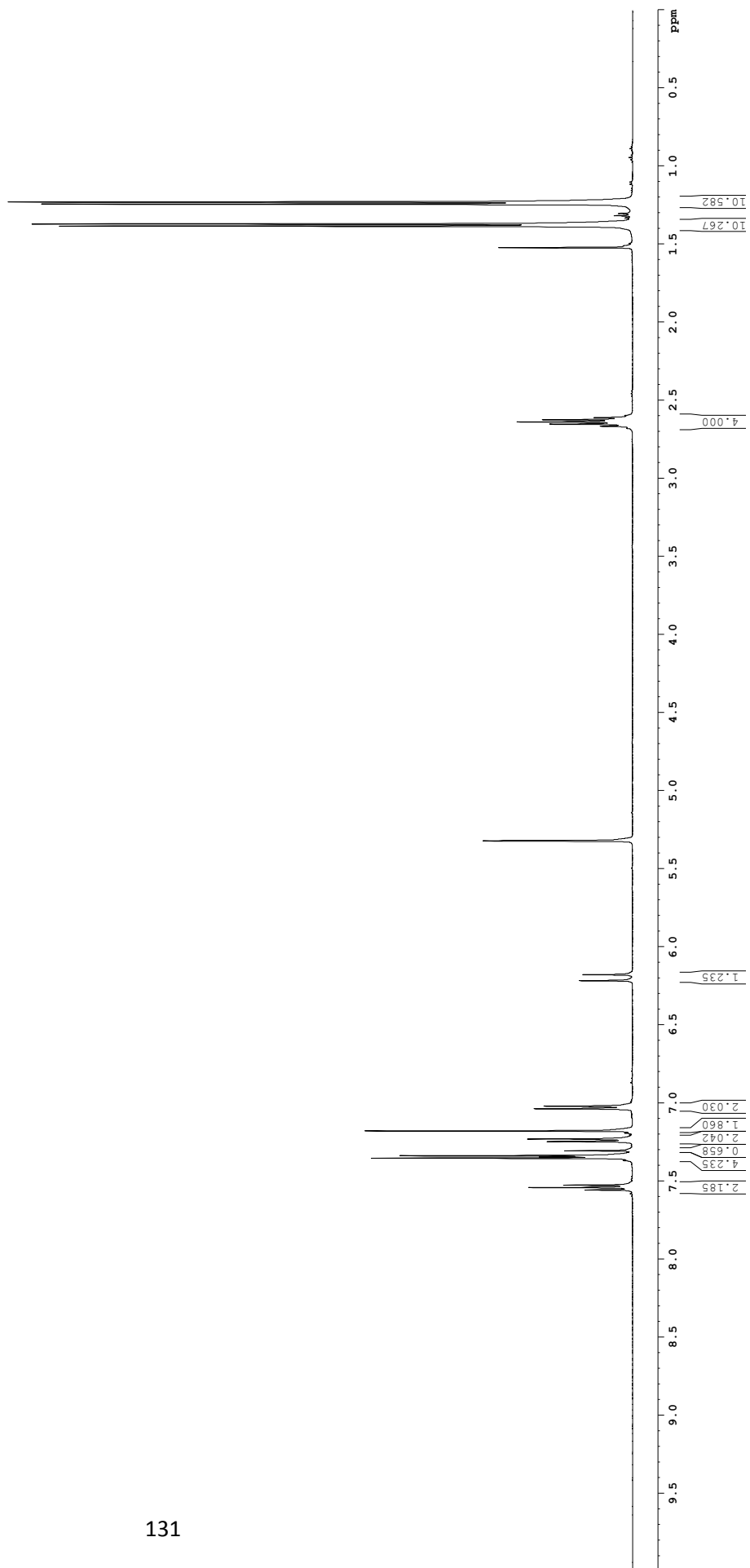
1.522
 1.384
 1.371
 1.317
 1.243
 1.230

2.666
 2.652
 2.638
 2.625
 2.611

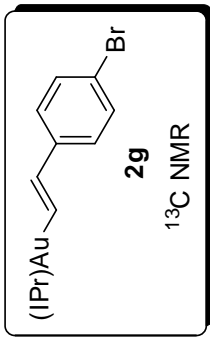
5.322

6.179
6.218

7.558
 7.543
 7.527
 7.354
 7.345
 7.338
 7.307
 7.248
 7.231
 7.180
 7.038
 7.021



197.375



160.529

146.456

141.718

140.821

135.160

131.451

130.747

127.096

124.584

124.531

123.635

118.879

54.432

54.216

53.999

53.783

53.567

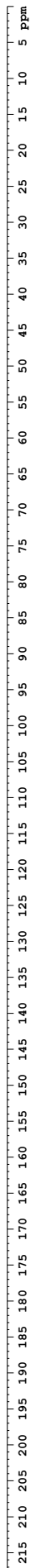
29.302

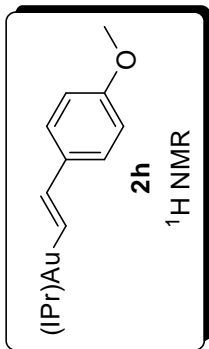
24.792

24.685

24.224

24.175





1.523
 1.386
 1.372
 1.238
 1.224

2.628
 2.642
 2.655

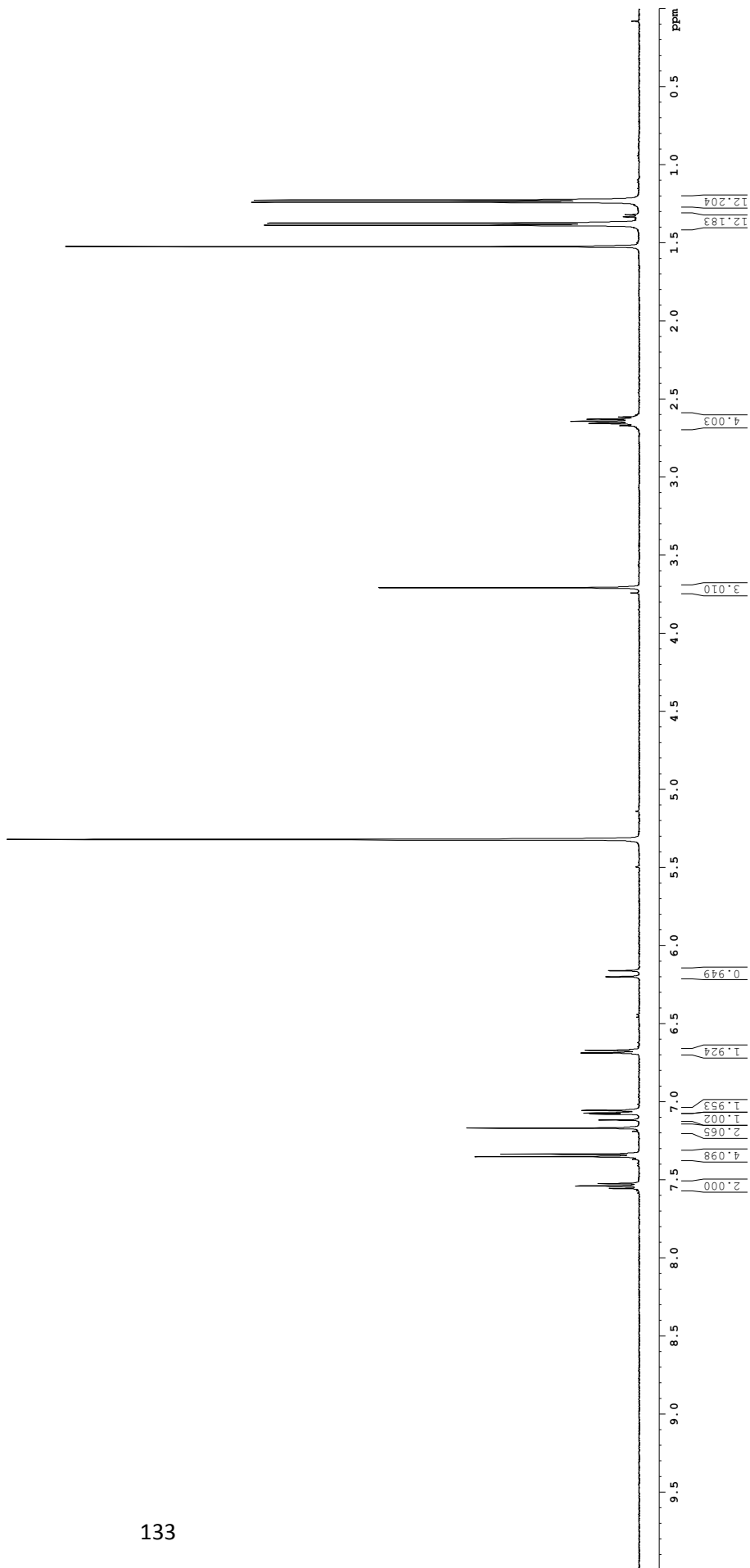
3.708

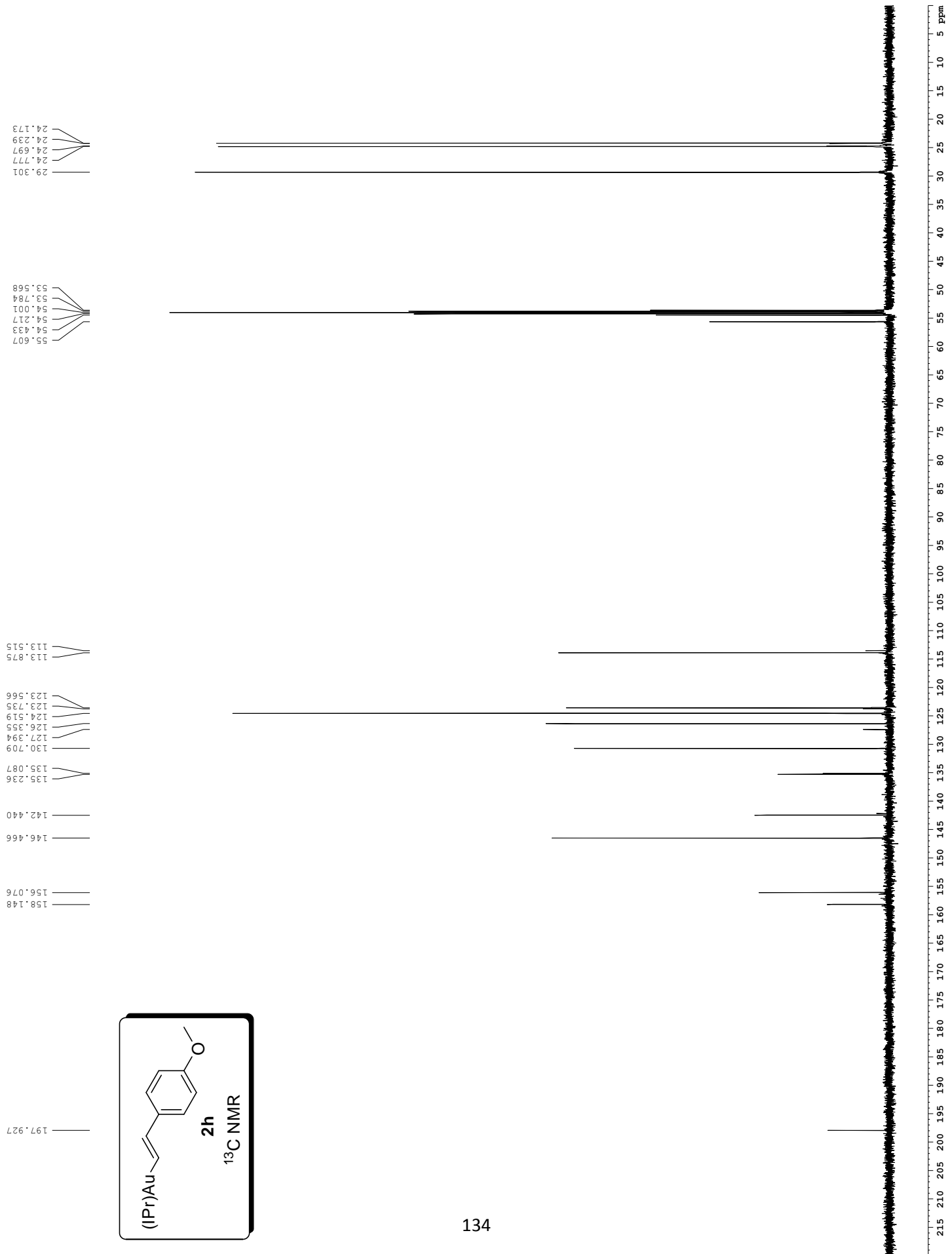
5.322
 5.320
 5.318

6.199
 6.161

6.670
 6.688

7.055
 7.072
 7.079
 7.117
 7.169
 7.336
 7.351
 7.524
 7.539
 7.555





IV. NMR Spectra for Isomerization Experiment of 2e in C₆D₆ and CD₂Cl₂

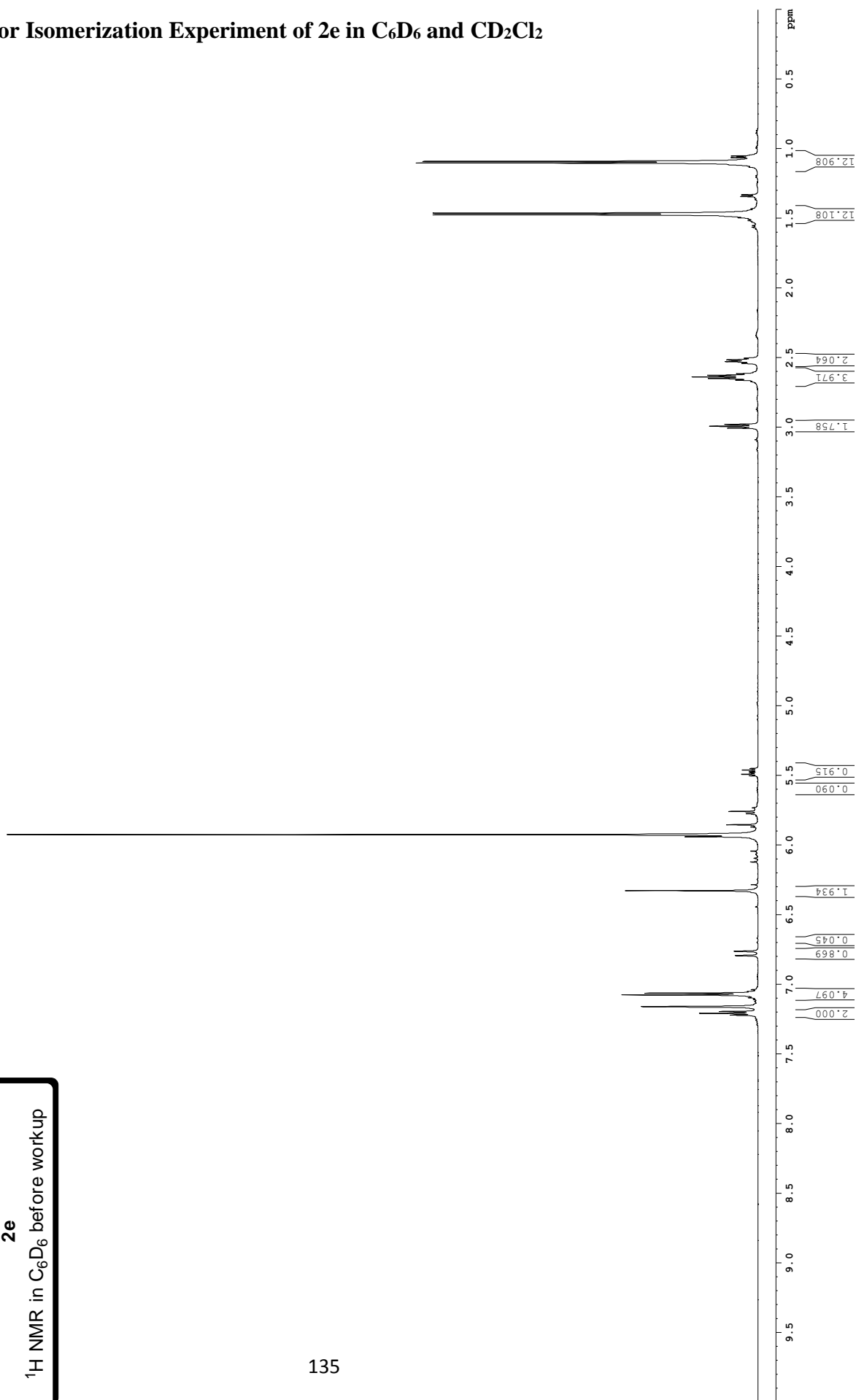
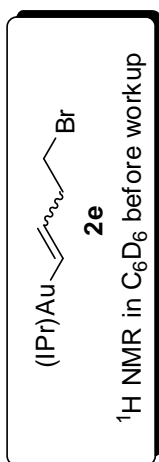
1.515
1.504
1.495
1.473
1.462
1.442
1.342
1.331
1.114
1.101
1.089
1.063
1.051

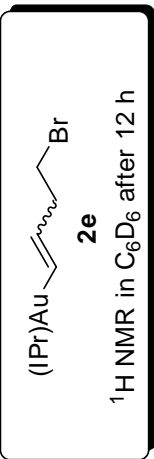
3.005
2.995
2.979
2.661
2.649
2.638
2.626
2.615
2.540
2.528
2.516
2.504

5.940
5.924
5.854
5.775
5.758
5.491
5.461

6.327

7.221
7.208
7.195
7.160
7.076
7.063
7.051
6.793
6.763



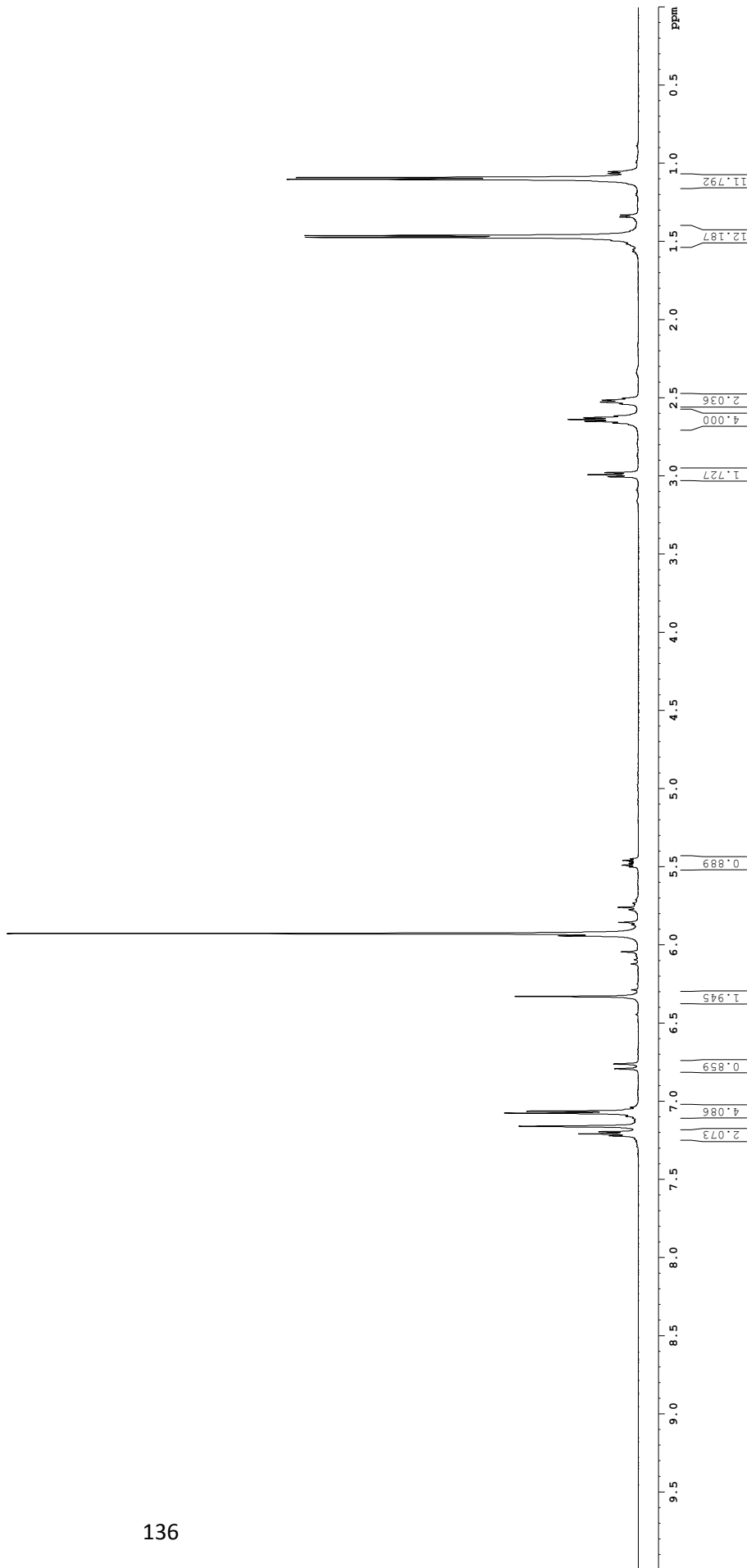


1.524
 1.514
 1.494
 1.472
 1.461
 1.430
 1.342
 1.330
 1.101
 1.089
 1.063
 1.052

3.004
 2.991
 2.978
 2.671
 2.660
 2.649
 2.637
 2.626
 2.615
 2.538
 2.526
 2.514
 2.502

6.044
 5.926
 5.855
 5.775
 5.759
 5.500
 5.490
 5.479
 5.469
 5.459

7.221
 7.208
 7.195
 7.160
 7.095
 7.076
 7.063
 6.792
 6.761

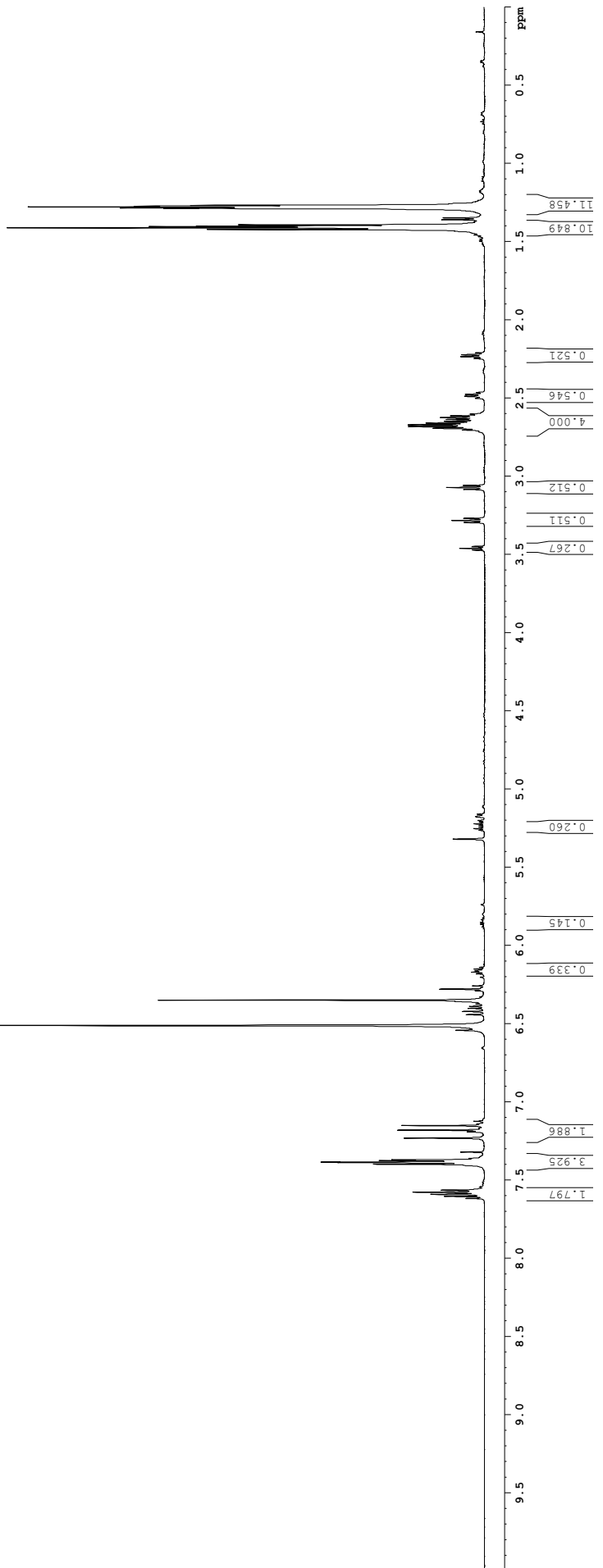




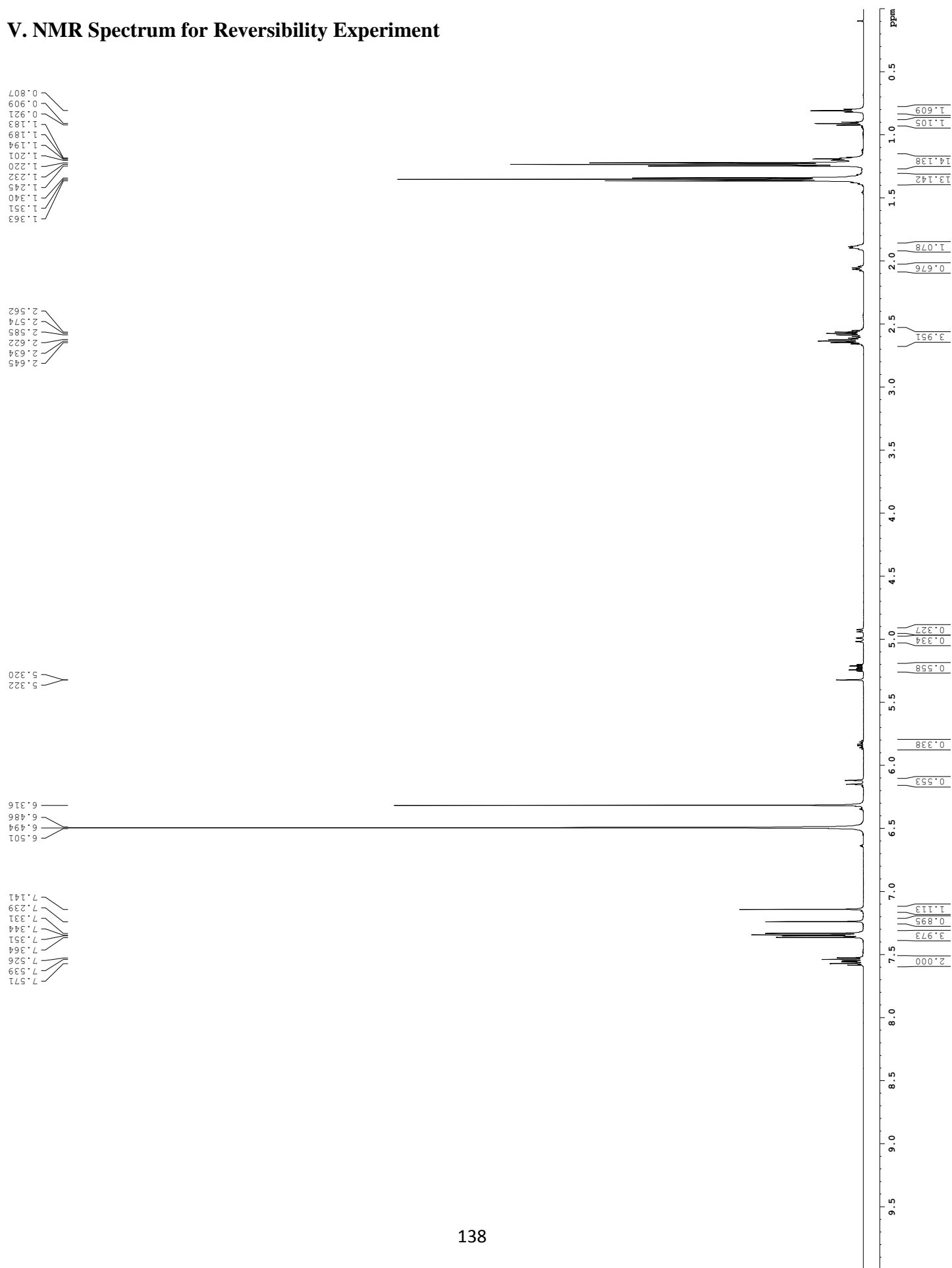
3.460
 3.295
 3.282
 3.268
 3.083
 3.071
 3.058
 2.704
 2.692
 2.681
 2.670
 2.659
 2.648
 2.636
 2.624
 2.613
 2.488
 2.476
 2.235
 2.222
 1.432
 1.421
 1.410
 1.402
 1.399
 1.391
 1.358
 1.347
 1.293
 1.287
 1.283
 1.277
 1.272
 1.266

5.320
 5.319

7.617
 7.604
 7.591
 7.577
 7.564
 7.398
 7.388
 7.385
 7.375
 7.370
 7.321
 7.232
 7.191
 7.180
 7.151
 6.542
 6.511
 6.442
 6.422
 6.402
 6.357
 6.349
 6.279



V. NMR Spectrum for Reversibility Experiment



References for Experimental Section

(1) Guo, H.; O'Doherty, G. A. *Org. Lett.* **2005**, 7, 3921–3924.

(2) Poupot, Mary et al. Phosphorylated Dendrimers as Antiinflammatory Drugs. U.S.

Patent 20,100,173,871, 8 Jul, 2010.

Chapter 5: Development of a New Experimental Method for Real-Time Imaging of Platinum–Sulfur Bond Formation

5.1 Introduction

The use of metal catalysts in modern chemistry is inextricably linked with the success of countless fields in research and industry.¹⁻⁵ To that end, the pursuit of knowledge in how to better understand and develop new catalysts is a never-ending search. The use of supporting surfaces for catalysts have been extremely beneficial for industrial processes, as it facilitates continuous operation, decreases waste, and circumvents the need for catalyst recovery/purification.^{6,7} However, when considering supported catalysts, there is often a distribution of reactivity among the various catalytic sites that is obscured through traditional analytical techniques, which generally rely on the aggregate behavior of a large ensemble of active sites.^{1,8,9} To understand how the behavior of subsets of catalysts on these supports, it is necessary to be able to spatially and temporally resolve and observe individual reaction sites.

To accomplish a task as demanding as this, single molecule microscopy can be utilized to observe and record individual chemical events, providing insight into the true nature of reactivity for various supported catalyst systems. Single molecule microscopy has been used extensively in biophysical systems as a way to monitor reaction distributions for over a decade, but has only recently begun to see adoption to chemical systems as well.¹⁰⁻²⁸

In order to visualize individual events, fluorescently tagged compounds can be used in combination with an imaging technique known as total internal reflectance fluorescence (TIRF)

(Figure 5.1).^{29,30} In this technique, an incident laser beam is aimed at a substrate at an angle such that when it reaches the interface between two surfaces, the beam is completely reflected back into the first material. Mathematically, this angle is determined through Snell's Law;

$$n_1 \sin \theta_i = n_2 \sin \theta_t$$

where n_1 and n_2 are the refractive indices of the two materials and θ_i and θ_t are the angles of the incident and transmitted light, respectively. Setting θ_t equal to 90° and solving for θ_i provides the critical angle, θ_c , at which total internal reflection will occur. When the incident beam is precisely aligned to the critical angle, the reflected light travels parallel to the interface of the two materials. At angles greater than this, it reflects back through the first material.

The key phenomenon of this technique is the appearance of an evanescent wave that extends into the second medium, even though no transmission of the actual beam occurs. This wave decays rapidly as it extends from the interface, resulting in a narrow volume in which excitation of a chemical species, such as a fluorophore, is possible.

5.2 Experimental Design

To examine the validity of applying this method to image chemical reactions at a surface, we set out to demonstrate imaging of a model system utilizing a platinum–sulfur covalent bond formation event as an indicator of a successful “reaction”, mimicking established ligand exchange chemistry of solution platinum complexes. By selectively patterning a glass coverslip with a thiourea-containing triethoxysilane reagent, we aimed to create “sticky” areas for a fluorophore tagged (dien)platinum complex to form a platinum–sulfur covalent bond to, effectively immobilizing the fluorophore tag and resulting in a definitive “on” event that could be observed (Figure 5.2).³¹⁻³³ Unbound fluorophores remain freely diffusing in solution, and are not localized long enough to produce a measurable signal.³⁰

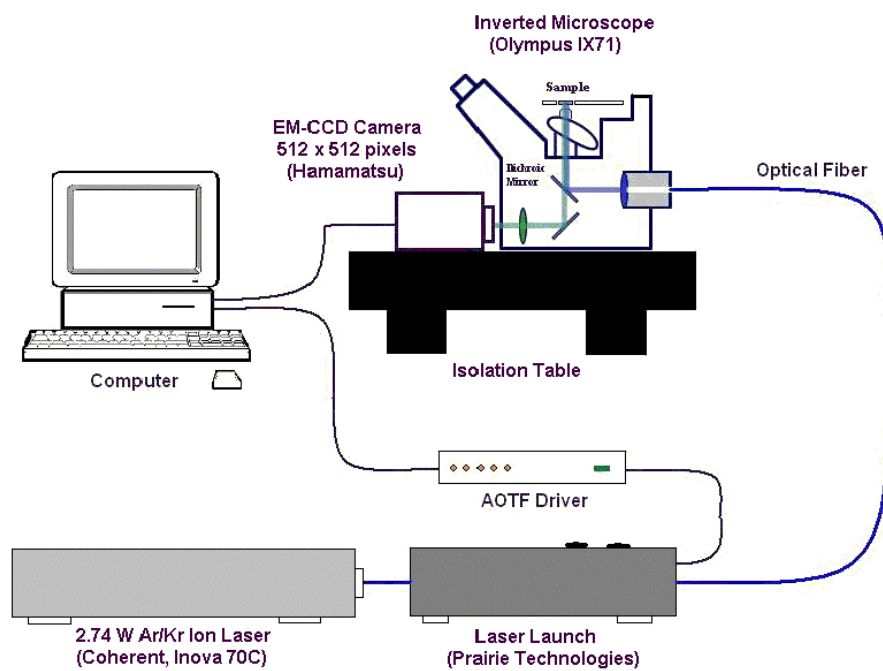
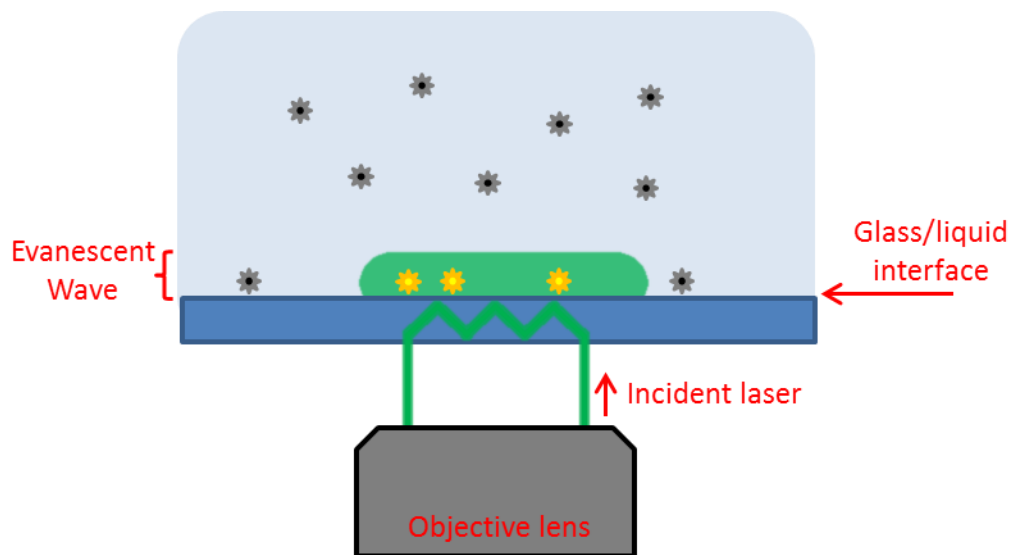


Figure 5.1: Graphic representation of TIRF microscopy with schematic of microscope apparatus used to image Pt-S bond formation.

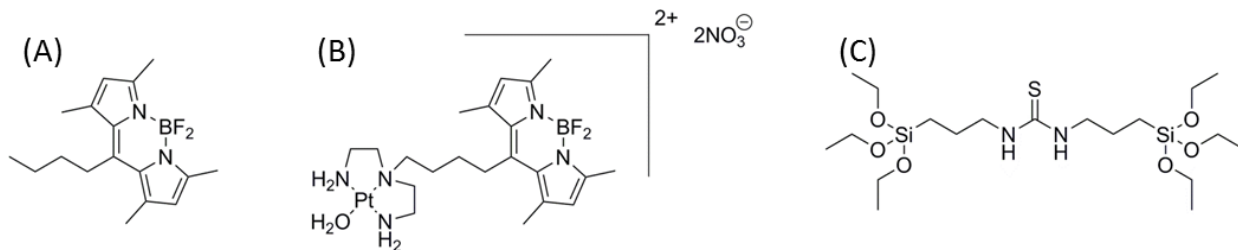


Figure 5.2: (A) BODIPY fluorophore, (B) (dien)Platinum complex, and (C) thiourea-functionalized silane used in this study.

Initial experiments involved addition of the platinum complex directly onto the surface of the coverslip. However, the sensitive nature of the auto-focus system associated with the microscope setup resulted in extremely high experiment failure rates due to loss of focus on the sample surface after addition.

To circumvent this issue, a new experimental apparatus (Figure 5.3) was designed, with the aim of not only avoiding defocusing issues, but also to more closely emulate the behavior of a real reaction environment containing a surface functionalized with a reactive species (such as a surface-supported catalyst) and reactant solution. In this system, a solution reservoir was created above the functionalized coverslip surface through the attachment of a glass wall, conveniently provided by cut glass test tubes cemented into place using an epoxy adhesive. The addition of solvent above the coverslip surface serves as a buffer to disperse the shock of reagent addition, preventing the microscope from losing focus. Furthermore, the reservoir allows for the free diffusion of reagents to and from the surface of the coverslip, allowing for more realistic reaction conditions as well as greater scope for modifying the parameters of the reaction, such as concentration, temperature, and solvent effects; all of which could potentially impact a real catalytic system.

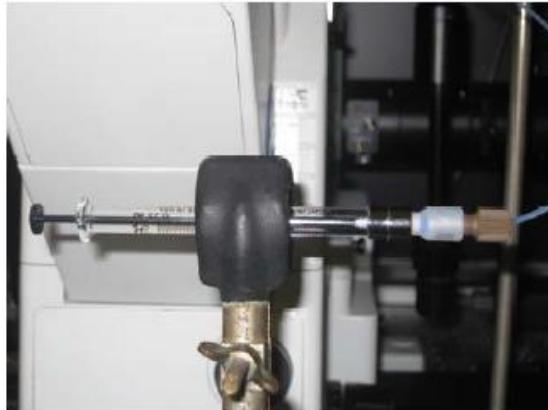
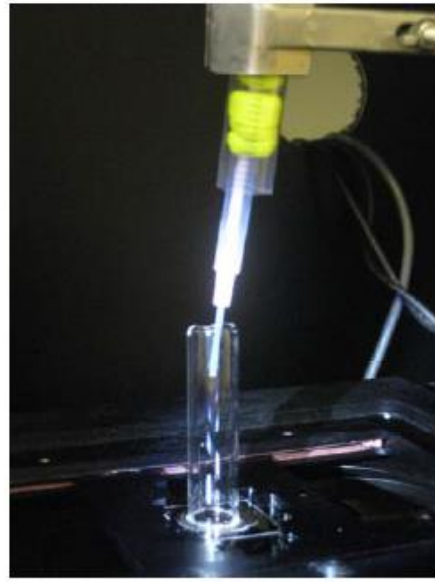
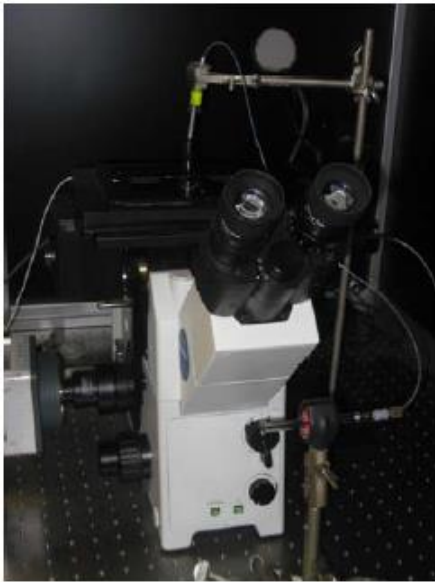


Figure 5.3: Revised injection setup consisting of reaction cell with attached gastight syringe.

5.3 Results and Discussion

Platinum's use as a catalyst is extremely well known, making it a prime candidate as a starting point for probing catalytic behavior at the single molecule level. Equally important to the success of this project is the use of the efficient BODIPY (dipyrromethene boron difluoride) fluorophore. BODIPY's high quantum yield coupled with its lack of reactive functional groups makes it an excellent choice to act as nothing more than a spectator for reporting the location of our compounds of interest, making it a useful, generalizable tool. By leveraging platinum's strong affinity for sulfur, these components provide all the tools necessary for real-time imaging of a chemical bond formation event at the single molecule level.

Functionalization of glass surfaces through silane coupling chemistry has a very rich history, and can be tailored to provide essentially any desired surface functionality. For these reactions, the bis(triethoxysilyl)thiourea complex was used in combination with traditional photopatterning techniques to selectively functionalize glass coverslips. Figure 5.4 outlines the process and shows a representative AFM image demonstrating the creation of chemically distinct sample surfaces, consisting of stripes of unfunctionalized glass and thiourea-functionalized glass.

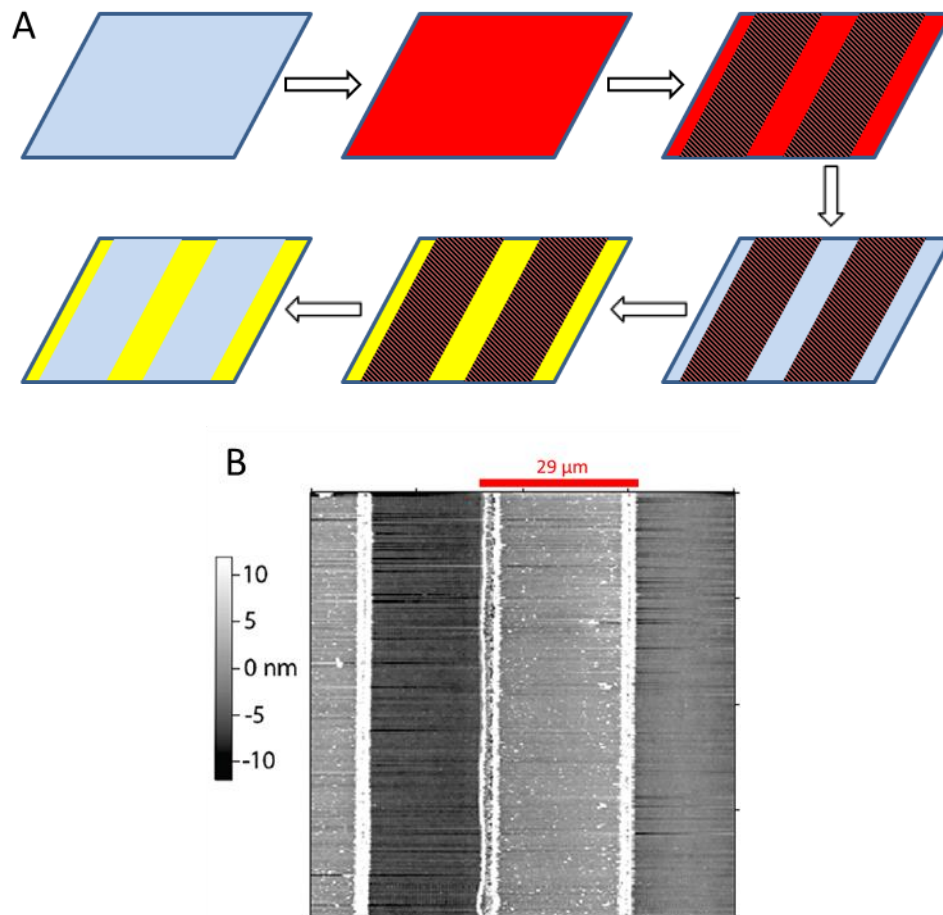


Figure 5.4: (A) Photopatterning of glass coverslips. Clockwise from top left: 1) SU-8 photoresist is spun onto cleaned coverslips. 2) Selective exposure to UV-light followed by heating crosslinks SU-8. 3) Unexposed SU-8 is removed. 4) Exposed areas are functionalized with thiourea. 5) Removal of crosslinked SU-8 restores blank glass surface. (B) AFM image of coverslip surface after patterning and functionalization.

Imaging of samples was conducted continuously, with each frame comprising data collected over 300 ms, with injection of the (dien)platinum complex defined as $t = 0$ ms. The final concentration of the platinum complex in solution after injection was calculated to be 5×10^{-10} M. The sample background was measured by beginning image acquisition for a set period of time prior to addition of the platinum complex. Figure 5.5 shows a typical set of images from a sample. Prior to injection (a), the sample surface only displays trace signals attributable to fluorescent impurities in the solvent. Upon injection (b), a number of fluorescent signals appear in select areas on the surface and are detected by the camera, prior to photobleaching, which results in quenching of their luminescence. Creation of a composite image (c) by collapsing the frames of data collected over several seconds further reveals localization of the fluorescent signals to areas patterned with the thiourea reagent.

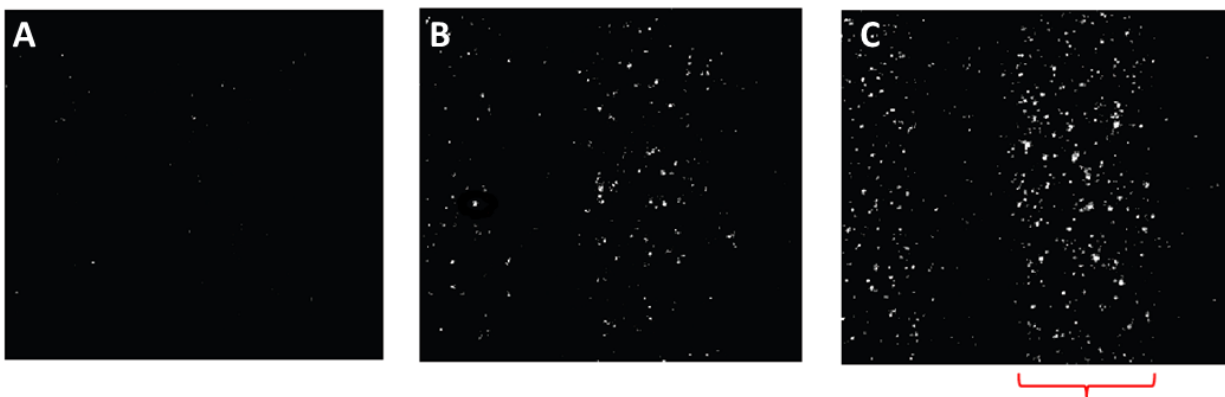


Figure 5.5: Representative data collected from addition of the (dien)platinum complex to a thiourea functionalized coverslip. (A) Sample surface prior to injection. (B) Single frame collected at 1.2 sec after injection. (C) Composite image of all data collected from 0.0–7.2 seconds. The red indicator highlights the section of the sample containing the thiourea functionalized silane.

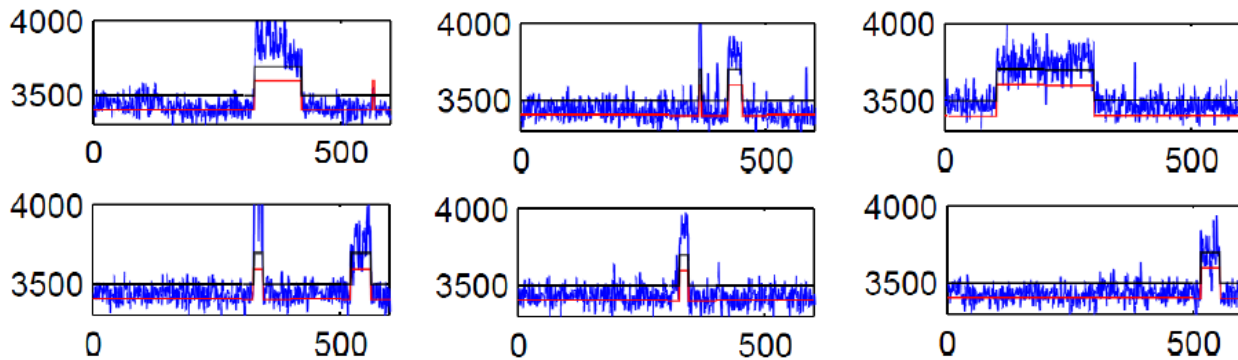


Figure 5.6: Representative Matlab time traces of the BODIPY-tagged (dien)platinum complex demonstrating quantized single molecule fluorophore behavior. The X-axis is frame number and the Y-axis is signal intensity.

Matlab analysis of the data collected from imaging experiments was used to illustrate the single molecule nature of the binding events. The appearance of fluorescent signals from individual fluorophores can be identified through quantized “on-off” events, marked by discrete changes in signal intensity, such as those observed in the time traces shown in Figure 5.6.³⁴ To avoid contributions from fluorescent impurities, only signals present (i.e. immobile) for three or more consecutive frames were quantified. Each trace corresponds to one separate bright spot imaged during the run.

The detection of fluorescent signals outside of the functionalize areas can be attributed to physisorption of the fluorophore-tagged complex to the glass surface.³⁵ This was confirmed through control experiments using the BODIPY analogue shown in Figure 5.2A, which lacked the ability to form any covalent bonds, and through measurements conducted with the BODIPY-tagged platinum complex using unfunctionalized glass coverslips. Through comparison of signal detection rates, it was estimated that non-specific binding through physisorption accounted for less than 2% of all observed binding events. The formation of covalent Pt–S bonds was further

confirmed by other lab members through the use of XPS to compare single molecule experimental samples with an authentic platinum–thiourea complex.

In conclusion, the creation of a new experimental approach facilitated the first demonstration of a spectator fluorophore being used to image a chemical reaction at the single molecule level outside of a biochemical environment, thereby illustrating the potential of single molecule spectroscopy to provide insight into organometallic reaction systems.

5.4 References

- (1) Weckhuysen, B. M. *Angew. Chem. Int. Ed. Engl.* **2009**, *48*, 4910-4943.
- (2) Yin, Y.; Liebscher, J. *Chem. Rev.* **2007**, *107*, 133-173.
- (3) Heitbaum, M.; Glorius, F.; Escher, I. *Angew. Chem. Int. Ed. Engl.* **2006**, *45*, 4732-4762.
- (4) Fink, G.; Steinmetz, B.; Zechlin, J.; Przybyla, C.; Tesche, B. *Chem. Rev.* **2000**, *100*, 1377-1390.
- (5) Heveling, J. J. *Chem. Educ.* **2012**, *89*, 1530-1536.
- (6) Ali, M. E.; Rahman, M. M.; Sarkar, S. M.; Hamid, S. B. A. *J. Nanomater.* **2014**, *2014*, 1-23.
- (7) Ma, Z.; Zaera, F.: Heterogeneous Catalysis by Metals. In *Encyclopedia of Inorganic Chemistry*; John Wiley and Sons, Ltd., 2006; pp 1-15.
- (8) Bouchard, L. S.; Kovtunov, K. V.; Burt, S. R.; Anwar, M. S.; Koptug, I. V.; Sagdeev, R. Z.; Pines, A. *Angew. Chem. Int. Ed. Engl.* **2007**, *46*, 4064-4068.
- (9) Bouchard, L. S.; Burt, S. R.; Anwar, M. S.; Kovtunov, K. V.; Koptug, I. V.; Pines, A. *Science* **2008**, *319*, 442-445.
- (10) Yildiz, A.; Tomishige, M.; Vale, R. D.; Selvin, P. R. *Science*, *303*, 676-678.
- (11) Van Oijen, A. M.; Blainey, P. C.; Crampton, D. J.; Richardson, C. C.; Ellenberger, T.; Xie, X. S. *Science* **2003**, *301*, 1235-1238.
- (12) Lee, J. B.; Hite, R. K.; Hamdan, S. M.; Xie, X. S.; Richardson, C. C.; van Oijen, A. M. *Nature* **2006**, *439*, 621-624.

- (13) Ditzler, M. A.; Aleman, E. A.; Rueda, D.; Walter, N. G. *Biopolymers* **2007**, *87*, 302-316.
- (14) Ha, T.; Ting, A. Y.; Liang, J.; Caldwell, W. B.; Deniz, A. A.; Chemla, D. S.; Schultz, P. G.; Weiss, S. *Proc. Natl. Acad. Sci. U.S.A.* **1999**, *96*, 893-898.
- (15) Sako, Y.; Minoguchi, S.; Yanagida, T. *Nat. Cell. Biol.* **2000**, *2*, 168-172.
- (16) Kiel, A.; Kovacs, J.; Mokhir, A.; Kramer, R.; Hertel, D. P. *Angew. Chem. Int. Ed. Engl.* **2007**, *46*, 3363-3366.
- (17) Bates, M.; Huang, B.; Dempsey, G. T.; Zhuang, X. *Science* **2007**, *317*, 1749-1753.
- (18) Ritchie, K.; Iino, R.; Fujiwara, T.; Murase, K.; Kusumi, A. *Mol. Membr. Biol.* **2003**, *20*, 13-18.
- (19) Greenleaf, W. J.; Woodside, M. T.; Block, S. M. *Annu. Rev. Biophys. Biomol. Struct.* **2007**, *36*, 171-190.
- (20) Roeffaers, M. B.; De Cremer, G.; Uji-i, H.; Muls, B.; Sels, B. F.; Jacobs, P. A.; De Schryver, F. C.; De Vos, D. E.; Hofkens, J. *Proc. Natl. Acad. Sci. U.S.A.* **2007**, *104*, 12603-12609.
- (21) Martinez Martinez, V.; De Cremer, G.; Roeffaers, M. B. J.; Sliwa, M.; Baruah, M.; De Vos, D. E.; Hofkens, J.; Sels, B. F. *J. Am. Chem. Soc.* **2008**, *130*, 13192-13193.
- (22) Roeffaers, M. B.; Sels, B. F.; Uji, I. H.; De Schryver, F. C.; Jacobs, P. A.; De Vos, D. E.; Hofkens, J. *Nature* **2006**, *439*, 572-575.
- (23) Xu, W.; Kong, J. S.; Chen, P. *Phys. Chem. Chem. Phys.* **2009**, *11*, 2767-2778.
- (24) Ameloot, R.; Roeffaers, M. B.; Baruah, M.; De Cremer, G.; Sels, B. F.; De Vos, D. E.; Hofkens, J. *Photochem. Photobiol. Sci.* **2009**, *8*, 453-456.
- (25) Shen, H.; Xu, W.; Chen, P. *Phys. Chem. Chem. Phys.* **2010**, *12*, 6555-6563.
- (26) Roeffaers, M. B.; De Cremer, G.; Libeert, J.; Ameloot, R.; Dedecker, P.; Bons, A. J.; Buckins, M.; Martens, J. A.; Sels, B. F.; De Vos, D. E.; Hofkens, J. *Angew. Chem. Int. Ed. Engl.* **2009**, *48*, 9285-9289.
- (27) De Cremer, G.; Roeffaers, M. B.; Bartholomeeusen, E.; Lin, K.; Dedecker, P.; Pescarmona, P. P.; Jacobs, P. A.; De Vos, D. E.; Hofkens, J.; Sels, B. F. *Angew. Chem. Int. Ed. Engl.* **2010**, *49*, 908-911.
- (28) Naito, K.; Tachikawa, T.; Fujitsuka, M.; Majima, T. *J. Phys. Chem. C* **2008**, *112*, 1048-1059.

- (29) Sako, Y.; Uyemura, T. *Cell. Struct. Funct.* **2002**, *27*, 357-365.
- (30) Axelrod, D. *Methods Enzymol.* **2003**, *361*, 1-33.
- (31) Howarter, J. A.; Youngblood, J. P. *Langmuir* **2006**, *22*, 11142-11147.
- (32) Wang, W.; Vaughn, M. W. *Scanning* **2008**, *30*, 65-77.
- (33) Gray, H. B. *J. Am. Chem. Soc.* **1962**, *283*, 1548-1552.
- (34) Weiss, S. *Science* **1999**, *283*, 1676-1683.
- (35) Wirth, M. J.; Legg, M. A. *Annu. Rev. Phys. Chem.* **2007**, *58*, 489-510.

5.5 Experimental Procedures

I. Coverslip Preparation

Glass coverslips (25 x 25 mm, 0.17 mm thickness) were cleaned through sonication in 20 mL of a 0.6% solution of Hellmanex detergent in Millipore water for 60 minutes and then rinsed sequentially with Millipore water and spectrophotometric grade ethanol. Residual solvent was removed with a compressed air stream and the coverslips were dried in a 115 °C oven.

Functionalization of the surfaces was accomplished by soaking the cleaned coverslips in Coplin staining jars containing 0.5 g of *N,N'*-Bis[(3-triethoxysilyl)propyl]thiourea in 20 mL of spectrophotometric grade chloroform for one hour. The functionalized coverslips were rinsed sequentially with Millipore water and spectrophotometric grade ethanol. Residual solvent was removed with a compressed air stream and the coverslips were dried in a 115 °C oven for 30 minutes. Control samples were prepared by soaking unfunctionalized coverslips in spectrophotometric grade chloroform and following an identical rinsing protocol.

II. Reaction Cell Construction

Hollow glass cylinders approximately 50 mm in length were prepared from commercial glass test tubes (13 x 100 mm) by scoring with a file. The cylinders were rinsed sequentially with Millipore water and spectrophotometric grade ethanol. Residual solvent was removed with a compressed air stream and the coverslips were dried in a 115 °C oven.

A commercial epoxy resin was used along the outer wall of the cylinders to attach the cylinders to the coverslips. The assembled reaction cells were covered and stored overnight to allow for full curing of the resin prior to use in experiments.

III. Data Acquisition

Imaging was performed using an Olympus IX71/IX51 inverted microscope. A 488 nm laser line was generated from an Innova 70C Kr/Ar laser running at 23 A (1.01–1.10 W). To maintain sample focus, a separate 780 nm laser continuous reflective-interface feedback focus (CRIFF) system coupled with a z-axis controller and nanopositioner was employed. A bandpass filter allowing 510–540 nm light was used to selectively isolate BODIPY emission signals from the excitation and CRIFF lasers. Images were acquired on a Hamatsu Photonics C9100-13 CCD camera, with each pixel imaged representing an area of 267 nm². All microscope hardware was controlled using Slidebook software. Images were collected continuously, for 300 ms intervals.

IV. Fluorophore Solution Preparation

Aqueous (10^{-3} to 10^{-4} M) stock solutions of the untethered BODIPY and the BODIPY-tagged (dien)platinum complex (Figure 5-2 A and B, respectively) were prepared fresh prior to

use. A small amount of spectrophotometric acetone was used in preparation of these solutions to aid in solvation of the initial solids. Subsequent dilutions were performed using Millipore water such that the final ratio of acetone to water was 1:2000.

V. Acquisition of Images

A reaction cell was filled with 2.0 mL of water and loaded onto the microscope. The sample was illuminated with the 488 nm laser to achieve successful focus on the surface of the sample. At this point, the CRIFF was locked and 90 s of the blank solvent background was imaged to provide a reference. While continuing acquisition, a 200 μL aliquot of either the untethered BODIPY, (dien)platinum BODIPY complex, or blank solvent was then injected to the reaction cell via a gastight syringe/PTFE tubing apparatus shown in Figure 5-3, to afford a final in-cell concentration of 5×10^{-10} M. Image acquisition was continued for another 90 s.